Predictive Finite Rate Model for Oxygen-Carbon Interactions at High Temperature

A THESIS
SUBMITTED TO THE FACULTY OF THE GRADUATE SCHOOL
OF THE UNIVERSITY OF MINNESOTA
BY

Savio Poovathingal

IN PARTIAL FULFILLMENT OF THE REQUIREMENTS
FOR THE DEGREE OF
DOCTOR OF PHILOSOPHY

Thomas E. Schwartzentruber, Adviser

July, 2016

Acknowledgements

"It takes a village." – old African proverb

There are many to whom I am grateful, for being part of my journey during my graduate study and even before.

I want to start by thanking my advisor Tom (Prof. Thomas E. Schwartzentruber) for being a great mentor and advisor. He gave me the freedom and space to explore my ideas, my thoughts and never discouraged me from doing what I wanted. I started as a naive undergraduate student six years ago, and after his guidance, I feel positive that I can pursue a career in research with confidence. His working style, scientific rigor but most importantly, respect for students is something I wish to carry forward into my career.

I want to thank my committee members, Prof. Graham V. Candler, Prof. Ilja Seipmann and Prof. Ellad Tadmor for providing valuable inputs that has helped me to stay on course during my graduate research. I have been lucky to collaborate with several researchers during my study. I would like to thank all my collaborators, both peers and faculty, Prof. Graham V. Candler, Prof. Timothy K Minton, Prof. Adri vanDuin, Sriram, Vanessa and Eric Stern. Working on some unique research work and writing manuscripts with a diverse academic audience has been a great learning experience for me, both in terms of technical know-how and soft skills of working in a team. I want to especially thank Prof. Timothy K Minton and Vanessa J. Murray for sharing their experimental data with me and also their openness and willingness to collaborate closely with me. It has been a great experience working with them.

A special thanks to my former lab members, Paolo, Paul, Chonglin and Ioannis for all their help. Without their guidance, my PhD would have easily taken another two years. I want to thank Julie Koch, former graduate coordinator in the aerospace

department for making all the bureaucratic work much less painful. I would also like to thank the Air Force Office of Scientific Research (AFOSR) and Doctoral Dissertation Fellowship (DDF) grant for funding my research.

I have been fortunate to have a great circle of friends, who have always helped me understand that I am not alone in my struggles. I want to thank Aswin, Praggy, Juan, Carola, Claudia, Raja, Ranga, Thavil and Rohini. A long day at the lab has always been easier when we head out for a coffee at Starbucks or happy hour in Dinkytown. I want to take this opportunity to acknowledge my friends Prasanth, Liju, Pillai and Devdas for their love and support. You have all been there for me whenever I have needed you and thanks a ton for that.

I want to thank my grandparents, Sebastian appapan, Jose appapan, Thara ammamma and Thabitha ammamma for doting on me when I was a little kid and building beautiful memories with me.

I want to thank my parents, without whom none of this would have ever been possible. I can say without any hesitation that whatever little I have achieved, I owe to them. I could not have done anything, if not for their sacrifices and there is no way I can ever return the love, support and care they have given me. Thanks to my younger sister Stella, for showing me everytime that courage and honesty are virtues worth upholding, and inspiring me everyday. You have always had my back and believed in me even when I have doubted myself. Finally, thanks to Harshada, for bringing sanity into my life.

To Thara Ammamma,
forever will you be loved,
forever will you be remembered.

Abstract

An oxidation model for carbon surfaces is developed to predict ablation rates for carbon heat shields used in hypersonic vehicles. Unlike existing empirical models, the approach used here was to probe gas-surface interactions individually and then based on an understanding of the relevant fundamental processes, build a predictive model that would be accurate over a wide range of pressures and temperatures, and even microstructures.

Initially, molecular dynamics was used to understand the oxidation processes on the surface. The molecular dynamics simulations were compared to molecular beam experiments and good qualitative agreement was observed. The simulations reproduced cylindrical pitting observed in the experiments where oxidation was rapid and primarily occurred around a defect. However, the studies were limited to small systems at low temperatures and could simulate time scales only of the order of nanoseconds. Molecular beam experiments at high surface temperature indicated that a majority of surface reaction products were produced through thermal mechanisms. Since the reactions were thermal, they occurred over long time scales which were computationally prohibitive for molecular dynamics to simulate.

The experiments provided detailed dynamical data on the scattering of O, O_2, CO, and CO_2 and it was found that the data from molecular beam experiments could be used directly to build a model. The data was initially used to deduce surface reaction probabilities at 800 K. The reaction probabilities were then incorporated into the direct simulation Monte Carlo (DSMC) method. Simulations were performed where the microstructure was resolved and dissociated oxygen convected and diffused towards it. For a gas-surface temperature of 800 K, it was found that despite CO being the dominant surface reaction product, a gas-phase reaction forms significant CO_2 within the microstructure region. It was also found that surface area did not play any role in concentration of reaction products because the reaction probabilities were in the diffusion dominant regime.

The molecular beam data at different surface temperatures was then used to build a finite rate model. Each reaction mechanism and all rate parameters of the new model

were determined individually based on the molecular beam data. Despite the experiments being performed at near vacuum conditions, the finite rate model developed using the data could be used at pressures and temperatures relevant to hypersonic conditions. The new model was implemented in a computational fluid dynamics (CFD) solver and flow over a hypersonic vehicle was simulated. The new model predicted similar overall mass loss rates compared to existing models, however, the individual species production rates were completely different. The most notable difference was that the new model (based on molecular beam data) predicts CO as the oxidation reaction product with virtually no CO_2 production, whereas existing models predict the exact opposite trend. CO being the dominant oxidation product is consistent with recent high enthalpy wind tunnel experiments. The discovery that measurements taken in molecular beam facilities are able to determine individual reaction mechanisms, including dependence on surface coverage, opens up an entirely new way of constructing ablation models.

Contents

List of Tables

List of Figures

Chapter 1

Introduction

Aircraft's flying at hypersonic speeds or space capsules that enter a planetary body with an atmosphere have to grapple with the problem of a strong shock on the front side of the vehicle. The shock leads to a rise in temperature of the air around it which heats the vehicle and thermal protection systems (heat shields) that are used to protect the vehicle. Typically, heat shields made of light weight carbon composites are used for their thermal and structural performance. The rise in temperature across the shock also dissociates nitrogen (N_2) and oxygen (O_2) molecules into atoms. The dissociated atoms (especially oxygen atoms) are reactive with carbon surfaces and when the atoms collide with the vehicle, they oxidize the surface. At very high surface temperatures, carbon material also sublimates. These processes where the heat shield is being burnt off is called **ablation** and heat shields used for these applications are called ablative heat shields or ablators.

Ablative heat shields can be classified into porous and non-porous ablators. Porous ablators typically consists of carbon fibers impregnated by a polymer/phenolic matrix and in non-porous ablators, the matrix is also carbon based. Non-porous ablators may also include polycrystalline graphite, pyrolytic graphite, 3D Carbon-Carbon (C-C), and 2D C-C materials. Porous ablators are used for applications with lower heat flux (100 W/cm^2) and non-porous ablators are typically used in hypersonic flights where the heat flux is much higher (5000 W/cm^2). Although the details of the ablation process differ in porous and non-porous ablators, oxidation of carbon fibers/composites is central to the ablation of any carbon-based ablator.

Modeling the oxidation process in continuum solvers like computational fluid dynamics (CFD) involves prescribing a set of gas-surface reaction rates. It is difficult to obtain true gas-surface rates for these conditions because gas phase and gas-surface processes are strongly coupled. The complexities of hypersonic vehicle interacting with the air around it is illustrated in Fig. 1.1. Building a predictive oxidation rate model for ablation is the focus of this work.

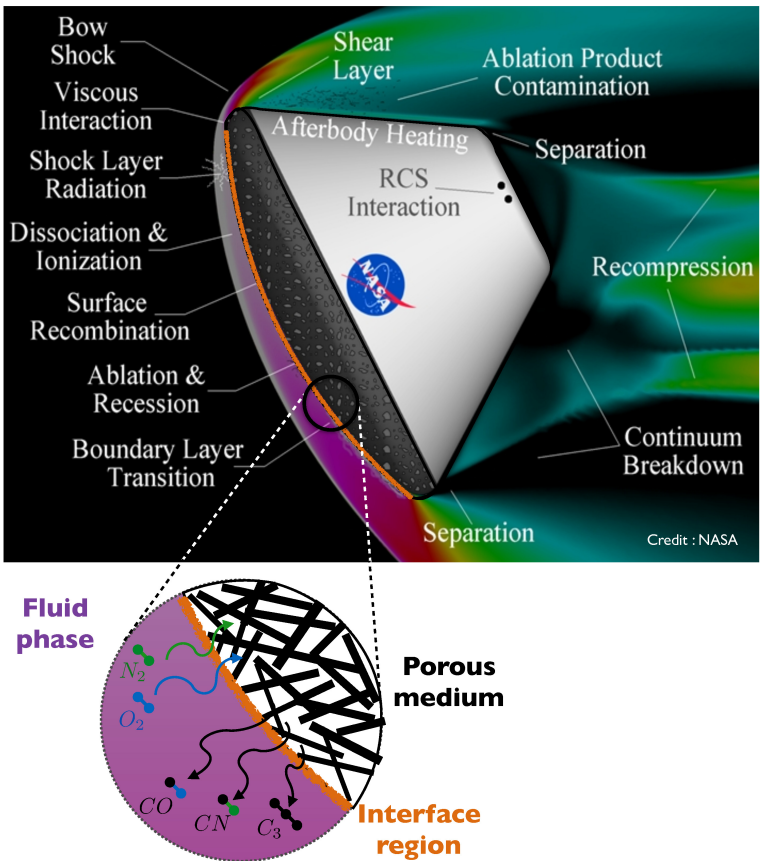

Figure 1.1: Processes when a hypersonic vehicle interacts with an atmosphere. Image taken from Ref. [5].

1.1 Previous Work

The two prominent rate models used in ablation modeling are from the work of Park (referred to as the Park model) [6] and the Zhluktov and Abe model (referred to as the

ZA model) [4]. These two models are described briefly here.

The Park model uses reactions shown in Table 1.1. The rate of all reactions in this model are expressed as kinetic flux of oxygen atoms to the surface ($\frac{P}{\sqrt{2\pi mkT}}$) times the reaction probability γ. The reaction probabilities are obtained from curve fit over several experiments. Figure 1.2 is reproduced here from Park's original paper [6] for the reaction (C(s)+O $\rightarrow$ CO), where all available experimental data at that time was collected and γ was obtained through curve fit over all available data.

Table 1.1: Park model.

Reaction	Rates	Reaction probability (γ)
C(s) + O + O $\rightarrow$ C(s) + O_2	$\gamma \frac{P}{\sqrt{2\pi mkT}}$	0.63exp(-1160/T)
C(s) + O_2 $\rightarrow$ CO + O	$\gamma \frac{P}{\sqrt{2\pi mkT}}$	$\frac{1.43\times10^{-3}+0.01exp(-1450/T)}{1+2\times10^{-4}exp(13000/T)}$
C(s) + O $\rightarrow$ CO	$\gamma \frac{P}{\sqrt{2\pi mkT}}$	0.63exp(-1160/T)

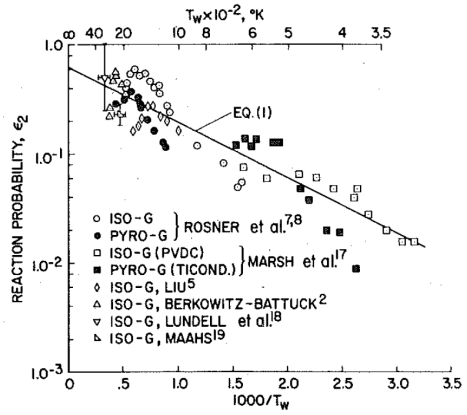

Figure 1.2: Curve fit performed by Park [6].

The ZA model is more complex and solves for surface coverage of adsorbed gas species on the surface. The rates are prescribed as a function of gas phase and adsorbed species concentrations. In the ZA model, the net oxidation is a manifestation of competing kinetic processes on the surface. The ZA reactions and rates [4] are shown in Fig 1.3. There are many parameters in the ZA model like ϵ_i, T_{a2}, T_{a3} etc. that are obtained empirically and since there is a huge spread in the experimental data, Zhluktov and Abe [4] proposed multiple values for some parameters. The ZA model is discussed

further in Chapter 5.

1.	$O + (C) \Leftrightarrow (C - O)$	$k_{f1} = \varepsilon_1 f_O$
2.	$O_2 + 2(C) \Leftrightarrow 2(C - O)$	$k_{r2} = \varepsilon_2 B(kT/h)e^{-T_{a2}/T}$
3.	$O_2 + (C) \Leftrightarrow (C - O) + O$	$k_{f3} = \varepsilon_3 f_{O_2} e^{-T_{a3}/T}$
4.	$O_2 + (C) \Leftrightarrow (C - O) + CO$	$k_{f4} = \varepsilon_4 f_{CO_2}$
5.	$(C - O) \Leftrightarrow CO + (C)$	$k_{f5} = \varepsilon_5 B(kT/h)e^{-T_{a5}/T}$
6.	$O + (C - O) \Leftrightarrow CO_2 + (C)$	$k_{f6} = \varepsilon_6 f_O e^{-T_{a6}/T}$
7.	$2(C - O) \Leftrightarrow CO_2 + 2(C)$	$k_{f7} = \varepsilon_7 B(kT/h)e^{-T_{a7}/T}$
8.	$(C) \Leftrightarrow C + (C)$	$k_{r8} = \varepsilon_8 f_C$
9.	$2(C) \Leftrightarrow C_2 + 2(C)$	$k_{r9} = \varepsilon_9 f_{C_2}$
10.	$3(C) \Leftrightarrow C_3 + 3(C)$	$k_{r10} = \varepsilon_{10} f_{C_3}$
11.	$N + (C) \Leftrightarrow (C - N)$	$k_{f11} = \varepsilon_{11} f_N$
12.	$(C - N) + N \Leftrightarrow N_2 + (C)$	$k_{r12} = \varepsilon_{12} f_{N_2} e^{-T_{a12}/T}$

Figure 1.3: Reactions and rates of ZA model [4].

These two models have been widely compared in existing literature. Here, findings from a few articles are discussed. Havstad and Ferencz [12] used the models to compare simulations with the Passive Ablation Nosetip Technology (PANT) [13] experimental data and found that both ZA and Park model [14] predicted lower ablative mass flux at the stagnation point for high stagnation pressure conditions. Gosse and Candler [10] compared the Park model adding new sublimation species but the stagnation temperature and recession rates were still under predicted when compared to the PANT data. Another model, more commonly used in material response codes is the equilibrium B' model. Beerman *et al.* [15] compared the B' and the Park model at various points on the Stardust trajectory and found that the two models gave different predictions with the most affected parameters being the convective heat load, the total heat load, the ablative and pyrolysis gas mass flux rates, and the recession results. MacLean *et al.* [3] compared four different models; two models based on the work of Park, the ZA model and a constant oxidation probability model. The models were compared using the CFD code, Data Parallel Line Relaxation (DPLR) and they found that all four models predicted different recession rates. Candler [16] performed a numerical analysis of the ZA, the Park and the B' model, for hypersonic conditions over altitudes ranging from 20-40 km, and found significant discrepancies between the models. At strong sublimation conditions (20 km), the B' approach predicted about 30% less mass loss rate at the

stagnation point. But when oxidation dominated (40 km), it predicted about 50% more mass flux than the finite-rate models, even in the stagnation region where the surface temperature was quite high (about 2500 K). A series of high speed flow experiments were conducted in the X-2 facility at the University of Queensland, Australia by Lewis and co-workers [17, 18] in order to evaluate the ablation models. An exhaustive comparison of the Park and ZA model with these experiments was performed by Alba *et al.* in the experimental range of 1770-2410 K can be found in Refs. [7, 19] and [20]. The predicted ablation products were quite different between the Park and the ZA model and neither of the models were able to predict the observed experimental products even in this relatively narrow range of temperature. At 1770 K, the ZA model agreed with the experiments, and at 2410 K, the Park model matched with the experimental data better. Not only did the models not agree with experiments, it was also not possible to predict the behavior of the models under different pressure and temperature conditions.

The Park and ZA models require a number of input parameters, empirically obtained through curve fits from various experiments [4, 6]. Experiments only quantify macroscopic observations such as mass loss or recession rate, which vary among different materials. For instance, different graphitic materials (pyrolytic graphite, polycrystalline graphite), and carbon composites (3D C-C, 2D C-C) exhibit different recession rates and mass losses in diffusion experiments [21].

The selection of tunable parameters has been further complicated by the recent study of Alba and co-workers which has indicated that gas phase reactions near the surface immediately convert the dominant oxidation product into a different species. Figure 1.4 from the work of Alba *et al.* [7] is reproduced here to demonstrate the coupling of gas phase and gas-surface reactions near the surface. In the X-2 facility at University of Queensland, graphite samples were tested and CN radiance profiles were measured along the boundary layer. The CN radiance profiles from the experiments are the lines marked as *X2*. Now, consider the results from the ZA model in Fig. 1.4. The basic ZA model as proposed [4] produced CN profiles indicated in the figure as *ZA(Johnston et. al)*. It can be seen that CN radiance profile is under predicted by the ZA model in this case. This prompted Alba *et al.* [7] to develop nitridation reactions for the ZA model. This is indicated in the figure as *ZA(ER Nitridation)* and it is seen that there is minimal change in the radiance profile. It was then found that the CN observed in

the boundary layer is due to the three gas phase reactions,

$$CO + M \longleftrightarrow C + O + M$$
$$N_2 + C \longleftrightarrow CN + N$$
$$CO + N \longleftrightarrow CN + O$$

After this observation, the ZA model was modified by Alba *et al.* [7] to produce CO at the surface as opposed to CO_2. The CN profiles for this case are plotted as *ZA Modifications* and significant improvement in the prediction can be observed.

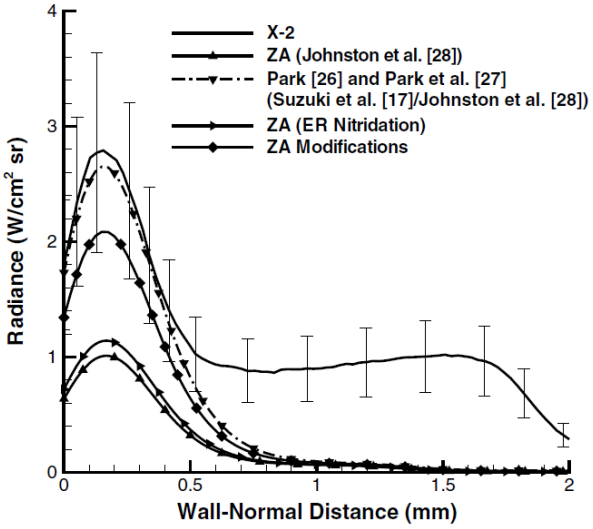

Figure 1.4: Figure from Ref. [7] comparing CN radiance profiles.

1.2 New Approach

The study described in the previous section clearly shows that experiments conducted in diffusion reactors and high enthalpy wind tunnels are inherently unable to decouple gas phase and gas surface reactions. Therefore, true surface oxidation rates cannot be predicted from these experiments. Furthermore, it is possible that an accurate rate model must take into account the different microscopic morphology of the various carbon materials, which can affect the net oxidation through differences in surface area, roughness etc.

The new approach taken here is to use simulation and experiments that probe atomistic interactions individually and then, based on an understanding of the relevant fundamental processes under a set of well defined conditions, build a predictive model that will be accurate over a wide range of pressures and temperatures.

Initial computational studies were performed using molecular dynamics (MD) [9, 22] to study oxygen and carbon gas-surface interactions at the atomic level. For highly oriented pyrolytic graphite (HOPG) at low surface temperature (500 K), large MD simulations qualitatively reproduced experimental data from molecular beam experiments [23]. The HOPG surface rapidly developed a high surface coverage of oxygen atoms and carbon-removal reactions occurred rapidly at defect sites leading to etch pits similar to those observed experimentally. The MD results are discussed in Chapter 2. Next, the effect of microstructure on the net composition of oxidation products was analyzed using direct simulation Monte Carlo (DSMC) and discussed in Chapter 3. Due to the computational expense limitations, the MD simulations could only simulate etch pits in the order of nanometers. The experimentally observed etch pits ranged up to, and above, micrometer-diameter with vastly more complex morphology than the MD simulations. Unfortunately, the precise configurations of atoms on the surface (required by MD simulations) is highly complex and unknown for ablating materials. Furthermore, MD simulations are only capable of capturing phenomena that occur over a timescale of nanoseconds. Chapter 4 discusses at length, the results from molecular beam experiments [24] performed at high surface temperature which show that most surface reactions are thermal [24, 25]. That is, they require the adsorption of oxygen and reaction products leave thermally accommodated to the surface over much longer timescales than are accessible to MD simulations. The molecular beam experiments [24] provide many details about the precise chemical reactions occurring between gas-phase molecules and a carbon surface. Furthermore, molecular beam results can be used directly to deduce surface reaction probabilities. Chapter 4 discusses the key results and observations from molecular beam experiments and this chapter also discusses the generation of *real* microstructure surfaces using X-ray microtomography and simulation of flow over *real* microstructures using DSMC. Finally, Chapter 5 discusses the development of a new finite rate model using molecular beam experiments.

Chapter 2

Molecular Dynamics

Interactions between dissociated gases and carbon-based surfaces are important in a number of engineering fields other than hypersonic vehicles. For example, graphene is a promising candidate for building atomistic-based electronic devices [26, 27]. Many of the unique properties of single-layer and few-layer graphene [28, 29, 30, 31] change due to edge state effects [32, 33] and crystallographic direction [34]. One possible method of creating nanoscale graphene topology with desired crystallographic and edge orientations is dry-etching. For example, hexagonal pits have been observed after high temperature gas treatment of highly oriented pyrolytic graphite (HOPG) [35, 36, 37]. In more recent experiments, exposure of HOPG to a gas of N atoms above 600°C (in a reactor tube) resulted in hexagonal etch pit formation, and longer strips were etched out of few-layer graphene (FLG) [38]. Many experiments have also shown cylindrical etch pit formation of HOPG when exposed to a high temperature gas (for example see Ref. [39]). Finally, low Earth-orbit is an O(^{3}P) rich chemical environment where hyperthermal impacts affect the durability of structural materials employed on orbiting spacecraft [40, 41, 42]. Nicholson, Minton and Seibner [8, 40] conducted several molecular beam experiments to study the effect of hyperthermal O atom (5 eV) impacts with HOPG at various surface temperatures. These experimental results [8, 40] document the etching of cylindrical pits on the HOPG surfaces and provide the motivation for the computational research presented in this chapter.

Since the experiments were performed on HOPG, composed of crystallites that have their c-axis parallel to the surface normal [43], only one facet of the crystal is exposed to the gas. HOPG is a commercially available material with very low defect densities

[44], thereby enabling detailed molecular chemistry analysis of the oxidation process. Furthermore, the O atom environment in a molecular beam is precisely characterized, enabling rigorous comparison between simulation and experiment. The molecular beam experiments on HOPG thus provide an ideal model problem where Molecular Dynamics (MD) simulation becomes a tractable model able to investigate the active chemical sites (crystallographic orientation and defects), the precise chemical mechanisms, as well as the activation energies associated with reactions on these surface sites, which combined, lead to the observed etching morphology. Ideally, if such etching could be fully understood at the atomistic level, engineers could tailor dry etching techniques for microelectronics manufacture to create nanoscale graphene topologies with desired crystallographic and edge orientations. For aerospace applications, understanding the oxidation mechanisms, activation energies, and dominant product species are important for modeling high temperature oxygen-carbon interactions that occur on vehicle heat shields [45]. It has been observed, for example, that injection of CO_2 gas into a high-speed boundary layer can delay transition to turbulent flow due to an overlap in frequencies between the dominant fluid instability mode and the vibrational mode of a CO_2 molecule, which enables the fluid instability energy to be transferred into internal energy of the CO_2 gas [46]. Thus, specific oxidizing reactions forming CO_2 could be highly beneficial to delaying turbulent flow and thus lowering drag and heating rates on such vehicles.

The experiments by Nicholson, Minton and Seibner [8, 40] motivated a density functional theory (DFT) study by Paci *et al.* [23] and MD simulations by Srinivasan and van Duin [47]. These computational studies were performed for a single layer of graphene and few atoms (approximately 24 atoms in the MD study). Morón *et al.* [48] have studied oxygen collisions with surfaces consisting of two graphene layers, however, considered only two lattice units. The MD simulations of Srinivasan and van Duin [47] indicated that simulation results would differ if a wider graphene sheet was simulated, however, this dependence was not analyzed in detail.

This chapter studies the collision of hyperthermal O atoms with HOPG (matching experimental conditions of Ref. [8]) through large-scale MD simulation, where larger HOPG surfaces are simulated for longer times, compared to prior computational research. Such larger simulations enable a more direct comparison with experimental data and thus more rigorous validation of the inter atomic potential used in the MD

simulations. In addition, qualitative and quantitative information regarding etch pit growth, precise reaction mechanisms, reaction products, and activation energies can now be obtained by the simulations. In this work, HOPG is simulated as multilayered graphene. The current simulations differ from previous work in that a larger surface area as well as many sub-layers are simulated, surfaces are bombarded with O atoms sequentially, and the surface continually evolves due to these sequential collisions. Prior computational simulations that were performed exposed the same graphene surface to all the incoming oxygen atoms (in effect studying independent simulations) and thus did not directly simulate the evolution of an etch pit. Also, in single layer graphene, Paci *et al.* [23] observed gaseous products leaving from below which would not be observed in a real HOPG sample.

The chapter is organized as follows. Section 2.1 describes the inter atomic potential function used for the MD simulations and discusses its accuracy compared to relevant *ab-initio* data, MD simulation initialization, surface thermostating, and etching simulation methodology. Section 2.2 presents simulation results for surface coverage and initial defect formation due to oxygen impact. This chapter ends with conclusions from this study.

2.1 Molecular Dynamics Simulation Methodology

2.1.1 Inter atomic potential

ReaxFF is a transferable bond order dependent potential that uses a relationship between bond distance and bond order on the one hand and a relationship between bond order and bond energy on the other to describe bond formation and bond breaking realistically [49]. Many body interactions such as the valence and torsion angle interactions are formulated as a function of bond order so that their energy contribution vanishes smoothly upon bond dissociation [49]. Atomic charges are calculated using the EEM scheme of Mortier *et al.* [50]. ReaxFF is an empirical potential that is parametrized against an extensive quantum chemical database [49, 51]. While quantum chemical methods enable accurate simulation of chemical reactions, the large computational cost of these methods limit them to systems of size $\sim$100 atoms and time scales of a few pico-seconds. ReaxFF provides the capability to simulate much larger systems ($>>$1000 atoms) [52] for times scales of the order of a few nano-seconds while retaining most of

the quantum chemical accuracy [49, 51]. The system energy using ReaxFF is expressed as the sum of a number of terms:

$$E_{\text{sys}} = E_{\text{bond}} + E_{\text{over}} + E_{\text{under}} + E_{\text{lp}} + E_{\text{val}} + E_{\text{pen}} + E_{\text{tors}} + E_{\text{conj}} + E_{\text{vdWaals}} + E_{\text{Coulomb}} \tag{2.1}$$

A detailed description of each of these terms can be found in the original work [49]. In the present work, we have used the C/H/O ReaxFF parameter description developed by Chenoweth *et al.* [51]. Since its development, this parameter set has been used to study a diverse set of phenomena such as the combustion of various fuels [53, 54] and fullerene self-assembly from benzene precursor [55]. Specific to the problem of graphene (or graphite) oxide chemistry, this parameter set has been shown to reproduce experimentally observed chemical changes during the reduction of graphene oxide [56] and DFT data on the chemical events occurring during the hyperthermal oxidation of graphene [47]. An important aspect of the ReaxFF potential is that the parameters can be refined in an iterative manner by building a larger training set as research on a specific problem proceeds [57].

2.1.2 HOPG surface model and temperature control

The simulations were performed using LAMMPS (Large-scale Atomic/Molecular Massively Parallel Simulator) [58] with the ReaxFF parametrization described above. This enables the simulation of large systems for long time scales. The HOPG surface is modeled as bulk hexagonal graphite crystal with ABAB stacking (Fig. 2.1). Apart from the bond lengths within the plane, the ReaxFF potential used must also predict the spacing between planes accurately. A bond length of 1.42 Å and an interplanar spacing of 3.35 Å were reported from experiments [43, 44]. An energy minimization was performed on an HOPG structure (initiated with the experimental bond lengths and interplanar spacing) using the ReaxFF potential. The new bond lengths were then determined at the end of the minimization process. During the minimization, the simulation box was allowed to expand to reduce the internal stresses in the structure. The final bond length and the interplanar spacing obtained were 1.44 Å and 3.35 Å respectively. Thus, the ReaxFF potential predicts equilibrium values very close to that observed in experiments.

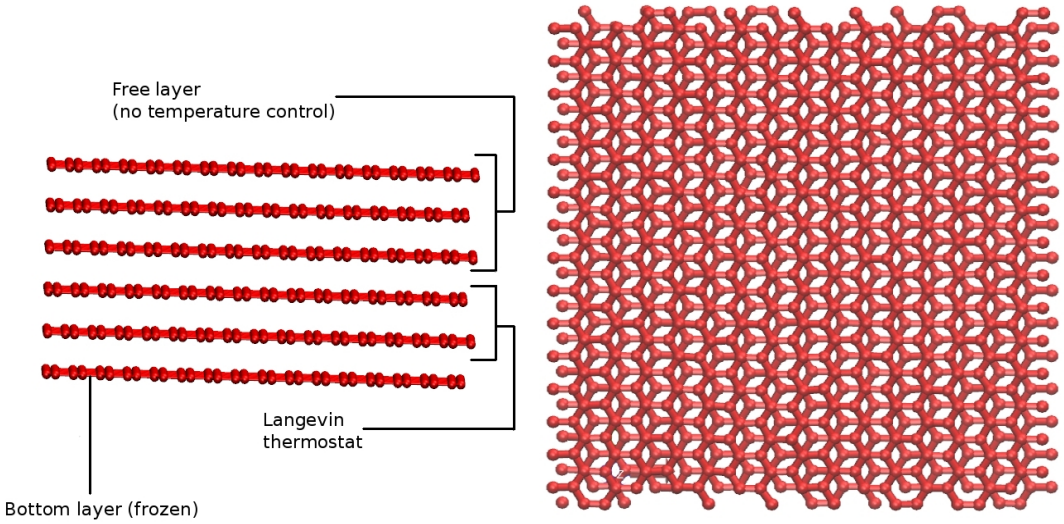

Figure 2.1: Simulated HOPG crystal structure.

Initial studies were performed on a 6 layered HOPG crystal as shown in Fig. 2.1 with each layer containing 480 atoms. The bottom layer was frozen, the two layers above it were temperature controlled through the Langevin thermostat (damping parameter of 500 units) to simulate the effect of a bulk system and the other layers did not have any temperature control allowing for local increase in temperature for reactions. Periodic boundary conditions were implemented in the intraplanar directions while the direction normal to the surface had a supercell dimension of 100 Å in order to simulate the system in vacuum [59]. This also ensured that the atoms or molecules leaving the surface by scattering (atomic oxygen) or reaction (CO, CO_2 and O_2) do not strike the image of the surface from below. The lateral dimensions were large enough such that self interactions of collisions were avoided in the system. Only one side of the HOPG structure was exposed to O atoms. The O atoms were placed 15 Å above the top surface to ensure that the surface and the O atoms do not interact initially and they were given velocities corresponding to 5 eV normal to the surface. The bottom layer was frozen to ensure that the center of mass of HOPG does not translate during the simulation. Integration was performed using the velocity-verlet algorithm, and a time step of 0.25 fs was used for which conservation of energy was verified within the simulations.

Initially, collisions of high energy O atoms on the virgin sample (pristine HOPG) was

simulated. Collisions were integrated for a time of 1 ps. Under low pressure experimental conditions [8] (where collisions on the simulated surface area would be separated by nanoseconds), any transfer of energy to the surface by the collision would transfer into the bulk material long before the next collision of an O atom. As evident in Fig. 2.2, allowing for 12.5 ps between successive collisions is sufficient time to avoid build up of energy in the simulation slab which would otherwise reach a very high temperature. This unphysical increase in temperature would strongly influence surface oxidation reactions [23, 47]. The simulations of Srinivasan and vanDuin [47] indicate that a single graphene sheet reaches a temperature above 4000 K within 70 collisions which is close to the sublimation temperature of HOPG. However, the experiments were performed under constant surface temperature and thus it is essential to control the temperature of the simulated system.

Waiting for such a long time between successive collisions is computationally expensive and unnecessary since no surface reactions or reconstructions occur during this time between collisions. The simulations here and other works [23, 47] have indicated that the collision-based reactions occur over very short time scales ($\sim$ 100-200 fs). To avoid this long wait time between collisions, the top three layers (free layers) are integrated without temperature control for 1 ps during which the hyperthermal O atom collides with the surface and adsorption, scattering, or reaction can occur. At this point, any atoms or molecules above a certain datum (30 Å) are deleted since these are the reaction products or scattered atoms that have left the surface. Thereafter, the entire system (except the bottom layer) is thermostated using the Langevin thermostat with a damping parameter of 500 units for 0.75 ps to the specified material temperature, after which the next collision is performed in the same manner. About 100 collisions are performed, using this two-step process and compared to the simulations where there was a time of 12.5 ps between collisions. Through the two-step process there were 39 O atoms that were adsorbed on the surface while when waiting the full 12.5 ps resulted in 37 adsorbed O atoms on the surface. Such tests indicate that the two-step process is able to speed up our simulations by $\sim$7 times without affecting the reaction dynamics. The final surfaces resulting from both simulation techniques are shown in Fig. 2.3. Carbon atoms are shown in green color and oxygen atoms are shown in purple color.

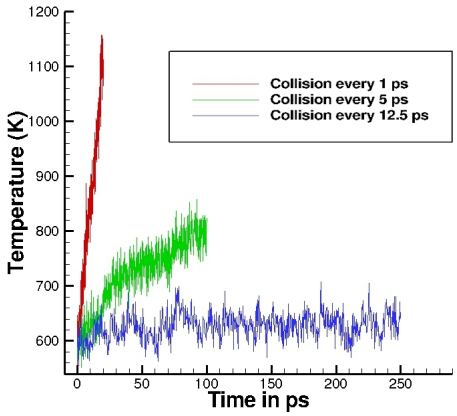

Figure 2.2: Effect of time between subsequent collisions on simulated HOPG sample temperature.

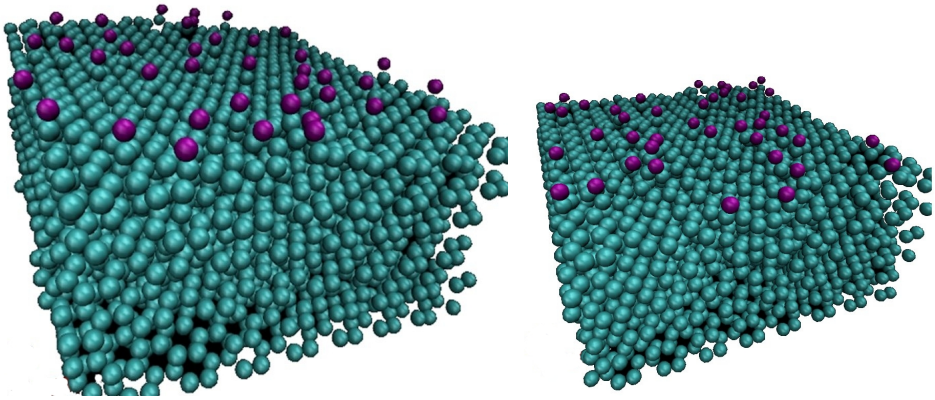

Figure 2.3: Oxygen surface coverage resulting from exposure to O atom beam with surface temperature control.

2.2 Results and Discussion

2.2.1 Surface coverage and initial defect formation

The C-C bond in the hexagonal layer is very strong and thus, the removal of a C atom from a pristine un-functionalized HOPG surface structure does not occur even on impact with a 5 eV O atom [42]. However, defects and adsorbed oxygen atoms on

the surface produce dangling and weaker bonds which enable the removal of C atoms from the surface. Experimental work [8, 40, 42] has indicated that pre-existing defects in manufactured HOPG samples are insufficient to explain observed oxidation results and that new defects are created when a pristine surface is exposed to atomic oxygen. Nudged elastic band (NEB) calculations [60] have shown that certain precursors that form on graphene sheets reduce the energy barrier for oxidation.

In these simulations, it was observed that after exposure to oxygen impacts, using the methodology described in section 2.2, a pristine HOPG surface obtains a surface coverage of adsorbed oxygen atoms (see Fig. 2.3 as an example). This surface coverage acts as a precursor and at some point a subsequent collision results an oxidation reaction (removal of a C atom) and produces a defect on the surface. After the initial defect is formed, collisions impacting the vicinity lead to further oxidation and thus more defect sites and an increased rate of removal of C atoms. Molecular beam experiments and ablation during flight occur over very long time scales ($\sim$ minutes). The interest here is not as much in studying the initial oxidation process but rather the steady rate of oxidation that is observed over long time scales in these experiments. MD simulation of the initial defect formation on a pristine sample is not representative of the steady oxidation processes occurring on an already heavily-oxidized material over experimental time periods. Ideally, molecular dynamics collisions should be performed and studied on a surface which has already undergone sufficient oxidation. The approach used here is to perform sequential MD collisions on a virgin sample. Since the collisions are sequential, one obtains a new surface after every collision and the collisions are performed until a steady rate of oxidation is observed. This enables to naturally *predict* an accurate representation of a significantly oxidized surface (an etch pit) through numerical simulation, which can then be analyzed in detail.

A pristine HOPG surface becomes covered with adsorbed O atoms after many collisions mostly as epoxide (C-O-C) groups and fewer O atoms as C-O groups. The experimental work in Ref. [61] shows emission spectra corresponding to epoxide groups on pristine surfaces and both epoxide and C-O groups once oxidation is initiated. The surface gets saturated with O atoms in a very short experimental time but over a rather long time scale relative to an MD simulation ($\sim$ 100 collisions). Thus, it is computationally efficient to start with a surface coverage of O atoms on the surface. Using the two step procedure for simulating continuous O atom collisions, and starting with a

pristine HOPG surface, an oxygen coverage is gradually established on the surface and after $\sim$ 175 collisions, a C atom is removed from the surface. In order to accelerate the calculations, a coverage of O atoms is initialized on the HOPG surface before starting the collisions and also artificially create a single defect on the top layer. This initial surface is shown in Fig. 2.4 (left) and is qualitatively the same as the surface resulting from collisions on an initial pristine surface without coverage or defect. As seen in Fig. 2.4 (right) oxygen atoms adsorb as either C-O-C (epoxide) groups or as C-O groups. Reducing the number of collisions simulated (to build a coverage of O atoms on the surface) saves approximately 28 hours of run time on a cluster of 64 core-processors (2.3 GHz processors). As will be detailed in the next section, the etch pit evolution proceeds rapidly about the defect.

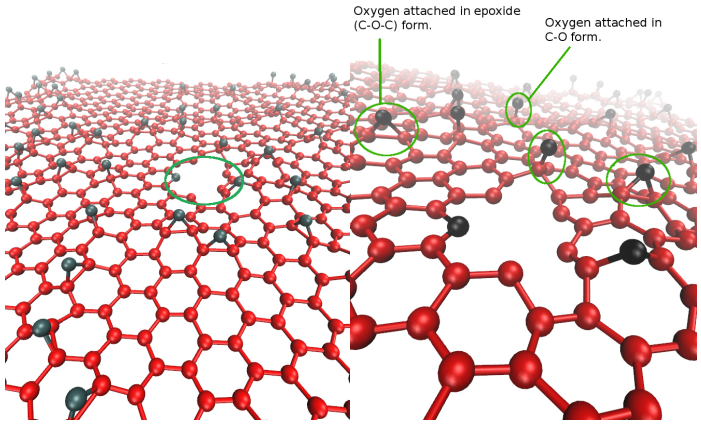

Figure 2.4: Initial HOPG surface used for etch pit simulations. Only the top layer is shown.

2.2.2 Etch pit evolution

A large number of continuous collisions were performed on a four-layer HOPG crystal with 760 atoms in each layer where the top surface layer was initialized as seen in Fig. 2.4. In this simulation, the two-step collision integration methodology was employed with temperature control to match the experimental surface temperature. Each layer of HOPG was wide enough so that the pit edges were sufficiently far away from the periodic boundaries of the HOPG surface. Here, the bottom layer was frozen, the layer above it had temperature control through the Langevin thermostat (damping factor of

500 units) and the top two layers had no temperature control.

A total of 1000 sequential oxygen atoms, with 5 eV energy, were collided with the HOPG surface. A snapshot of the resulting surface is shown in Fig. 2.5 along with an inset of an experimental image from Ref. [8]. The simulation predicts etch pit growth in the intraplanar direction to be much more rapid than the etching in the interplanar direction. As the simulations employ multiple graphene layers, it can be seen that the second layer ultimately develops a defect which also oxidizes to form a circular edge. This was observed experimentally [8] where shallow but wide etch pits were created. Such cylindrical pits are observed in both molecular beam experiments and high temperature gas oxidation experiments [39]. Thus, the MD simulations are in qualitative agreement with the experiment, although at a much smaller scale. Experimental analysis focused mainly on the widest etch pits observed on the HOPG samples due to measurement constraints. The pit diameters reported by Nicholson, Minton and Siebner [8] are on the order of $O(\mu m)$. In the MD simulations, the pit size is in the order of $O(nm)$. Despite the huge variation in length scale, it is possible that the edges of the simulated $O(nm)$ etch pits are chemically identical to the edges of the $O(\mu m)$ etch pits found in experiments.

The removal of C atoms (which herein is referred to as oxidation) occurs around the initial defect and the pit becomes wider with increase in exposure to O atoms. Oxidation primarily occurs around the edges because the C-C bonds in the graphite hexagonal network are extremely strong and stable. However, at the periphery of the pit, some carbon atoms have a dangling bond or are bonded to O atoms which reduces the energy barrier of oxidation. An incoming O atom is then able to remove the C atom from the periphery of the etch pit exposing new C atoms and the diameter of the pit increases.

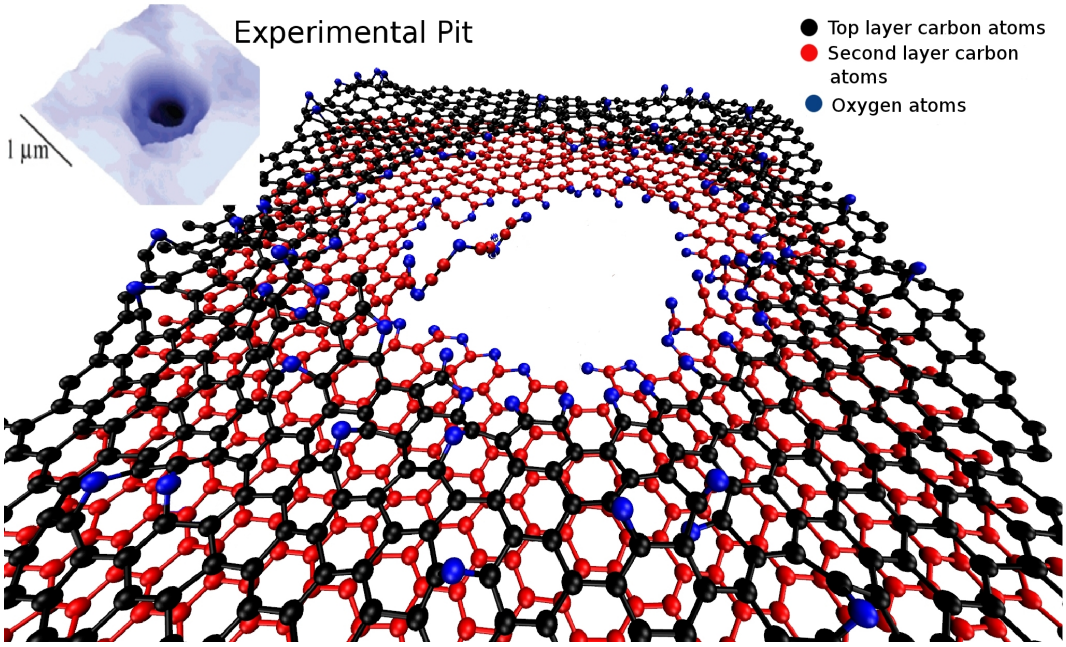

Figure 2.5: Evolution of a cylindrical pit predicted by MD simulation similar to those reported in experiments [8] (seen in the inset here).

Figure 2.6 plots the number of carbon atoms removed versus the number of collisions for a surface temperature of 600 K. As seen in the inset of Fig. 2.6, the first oxidation event (beyond the initialized single defect in Fig. 2.4) occurs after approximately 100 collisions. However, after approximately 200 collisions, the oxidation rate is approximately steady and the number of C atoms removed increases linearly with the number of O atoms that strike the surface. Considering only the data after 200 collisions and performing a linear fit (Fig. 2.6), results in a slope of 0.198. This corresponds to 1 C atom removed for every 5 incident O atoms and therefore indicates a very high oxidation probability for this high energy beam impacting a significantly oxidized surface.

Experimental observations [8] also found that the rate of oxidation increases with an increase in surface temperature for the same 5 eV beam energy. The experiments were performed in the temperature range of 298 K- 573 K. For our MD collision simulations, this temperature range is too narrow to investigate due to statistical variations. However, large-scale sequential collision simulations were conducted at different surface temperatures (300 K, 600 K, 1000 K and 1500 K). As seen in Table 2.1, the simulations predict an increased oxidation rate as the surface temperature is increased. This was

somewhat unexpected since the kinetic energy of surface C atoms due to the substrate temperature is negligible compared to the beam energy. Thus, the experimental (and numerical) result that oxidation increases with surface temperature points towards a contribution from thermal oxidation reactions; reactions not resulting directly from a collision. Indeed, such reactions occur within the MD simulations and will be discussed later.

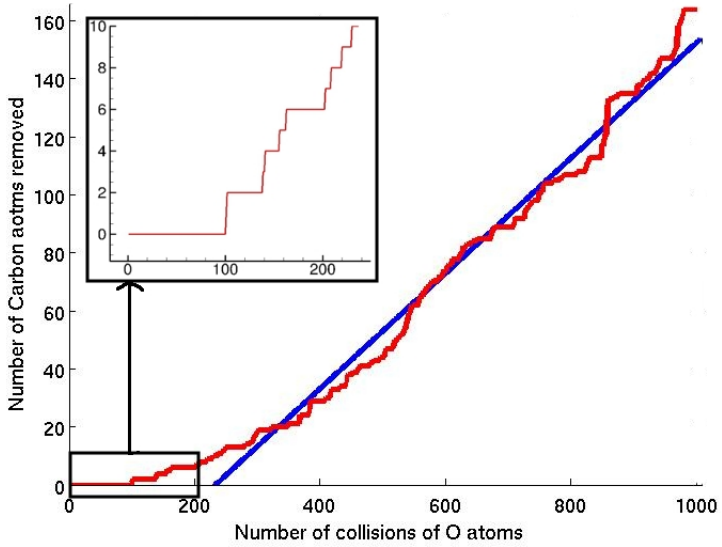

Figure 2.6: Number of carbon atoms removed from HOPG surface versus the number of O atom collisions at a surface temperature is 600 K.

Table 2.1: Surface temperature effect on the number of C atoms removed.

Surface Temperature (K)	Number of Carbon atoms removed
300	115
600	164
1000	224
1500	360

Such oxidation rates (or net removal of C atoms) cannot be quantitatively compared with the existing experimental measurements which record all oxidation products

leaving a macroscopic HOPG sample containing a huge number of etch pits of varying sizes. However, if all etch pit edges (where oxidation reactions are dominant) are chemically similar, then the ratio of certain reaction products detected experimentally may be quantitatively comparable to molecular simulation results. In another set of similar experiments [23] performed at a surface temperature of 503 K, the experimental data determine the ratio of CO to CO_2 leaving the surface as 1:2. Our MD simulations predict the ratio to be approximately 1:4 (26:98). It is noted that the MD simulation sample size is small, making a precise comparison difficult. In addition, both the simulations and experiment consistently determined the number of recombination reactions (producing O_2) to be far larger than the number of oxidation reactions.

Overall, the qualitative agreement between simulation and experiment is very promising, and the simulation data can be further analyzed for insight into realistic defect sites, associated reaction mechanisms and activation energies.

2.2.3 Reaction mechanisms and activation energies

Within the large-scale MD simulations it is possible to isolate each recombination and oxidation reaction (release of O_2, CO and CO_2) and determine on which type of chemical defect site the event occurred. Once such reaction sites are determined, the precise reaction mechanisms can be investigated along with associated activation energies. Two numerical strategies are employed for such analysis. The first involves isolating a specific defect chemistry and analyzing it using a small MD system. For example, the defect could be isolated on a small graphene sheet and a potential energy surface (PES) scan could be performed where system energies are computed for reactant and product species oriented in a range of geometries relative to a defect site corresponding to a presumed reaction pathway. The second strategy involves performing a large number of independent trajectory calculations on the actual etch pit surface (i.e. Fig. 2.5) at finite surface temperature, where the trajectories are localized to impact a single defect on the large surface. In this manner the full multidimensional PES is explored, including finite temperature surface dynamics and more realistic edge defects. Since the trajectory calculations are independent, a large number of trajectories can be efficiently computed using a range of impact energies. Average probabilities of specific reactions can then be computed as functions of impact energy for a given defect, which may better model the true reactions occurring on an oxidized HOPG surface during an experiment.

Catalytic recombination reactions

In analyzing the large-scale sequential collision simulation corresponding to a surface temperature of 600 K, $\sim 50\%$ of all O_2 molecules were produced through an Eley-Rideal (ER) type recombination where the incoming O atom reacts with a C-O group (as seen in Fig. 2.7) to form an O_2 molecule that leaves the surface. This specific catalytic recombination reaction is analyzed in this section.

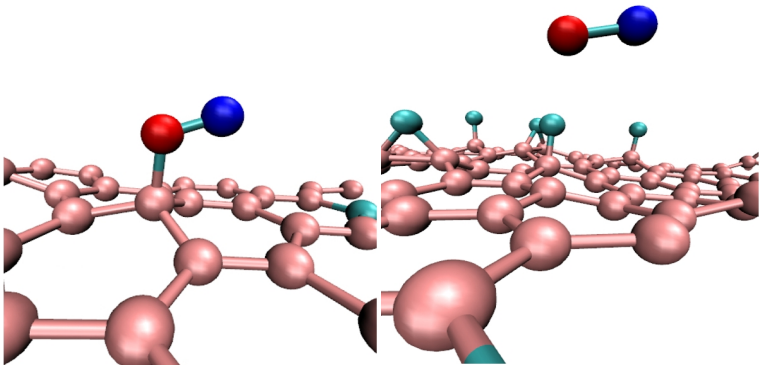

Figure 2.7: Atomic configuration of the dominant mechanism for production and release of O_2.

Recombination occurs on the entire surface and not just around the defects and thus, the first strategy (a PES scan) may be representative of the recombination occurring within the large-scale MD simulation. An approximate energy barrier for this reaction is obtained by dividing into two steps. First, the energy barrier that must be overcome for an incoming O atom to form an O_2 on the surface is computed by a one-dimensional PES scan. As depicted in Fig. 2.7, an oxygen atom is moved normal to the C-O defect at a lateral distance of 1 Å from the the adsorbed O atom (this is the approximate location of the minimum energy binding location). The energy scan is shown in Fig. 2.8 and the energy barrier is 0.3 eV. Second, as depicted in Fig. 2.7, the O_2 molecule is moved normal to the surface. The energy scan is shown in Fig. 2.8 and the energy barrier that must be overcome for the O_2 molecule to leave the surface is only 0.1 eV. Thus, the overall energy barrier required for this dominant recombination reaction is approximately 0.3 eV.

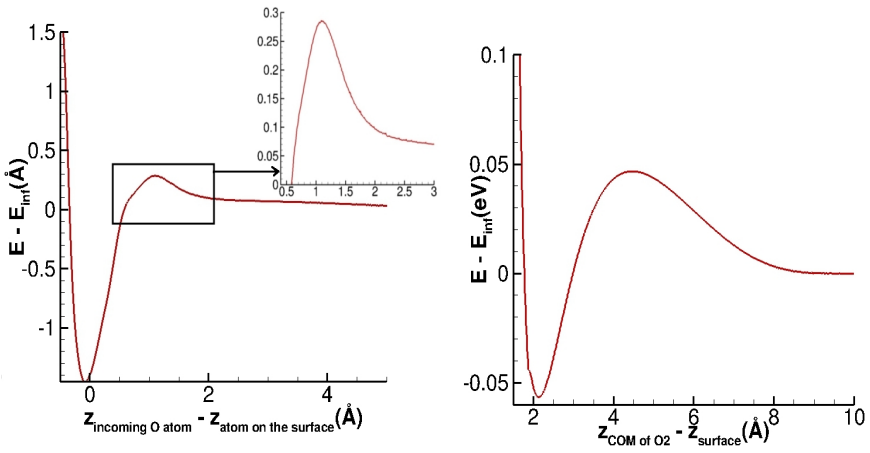

Figure 2.8: Energy barrier for the above reactions.

Trajectory analysis is also performed for this dominant recombination reaction. Specifically, in Fig. 2.7 the red O atom is the reactive site and the blue O atom is the incoming atom which collides on the reaction site. The incoming O atom is given various random initial positions within a circle centered about the red atom (the reaction site) and the surface is maintained at 600 K in the same manner as for the large sequential MD simulations. The trajectory calculations indicate that the probability of this recombination reaction increases drastically from 0.02 to 0.72 when the incident energy is increased from 0.25 eV to 0.6 eV (Fig. 2.10). Thus, as expected for this reaction, the trajectory analysis is very consistent with the PES scan analysis, verifying the trajectory methodology employed. The simulations therefore predict that the amount of recombination observed on HOPG samples (at 600 K) should decrease substantially below beam energies of approximately 0.2 eV.

Oxidation reactions

In analyzing the large-scale sequential collision simulation corresponding to a surface temperature of 600 K, it was determined that roughly 50% of all oxidation reactions where "thermal" and not the direct result of collision. Specifically, 48% of all CO_2 and 54% of all CO molecules produced were determined to be thermal reactions. The dependence of oxidation reactions on surface temperature (see Table 1) is due to such thermal reactions. However, since HOPG material is not simulated fully between collisions (in

fact all layers are thermostated including the top layer between collisions), these thermal oxidation predictions should be considered qualitative only. Such longer time-scale thermal reactions may require an alternate simulation methodology and further experimental characterization in order to make quantitative predictions and comparisons. Such reactions are important to the overall oxidation behavior of graphitic materials and certainly should be considered in future research. For the collision-based oxidation reactions, focus on the most dominant CO_2 reaction, which accounted for $\sim 43\%$ of all collision-based CO_2 production and is explained in this section. Similarly, the most dominant CO reaction is also analyzed and explained here.

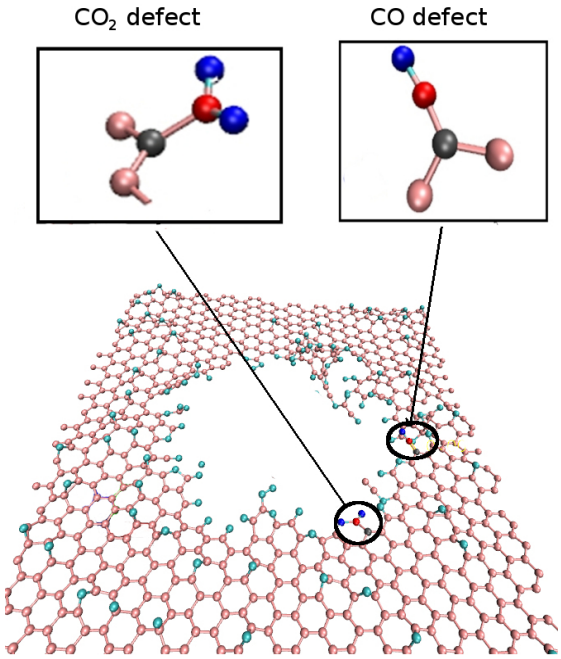

Figure 2.9: Example surface used for oxidation trajectory calculations (only top layer shown).

The inset in Fig. 2.9 shows the dominant reactive site for CO_2 determined from the large-scale sequential simulation. In this reaction, the formation of the CO_2 molecule on the surface requires several steps and trajectory calculations are unable to predict the energetics for each step of this process. However, the resulting CO_2 group is strongly bound to the surface and is unlikely to leave the surface due to thermal excitation. An

incoming O atom bonds to the the gray carbon atom (inset in Fig. 2.9) releasing the CO_2 molecule from the surface. This reaction step, where the incoming O atom adsorbs on the surface and the CO_2 molecule leaves the surface, can be simulated by trajectory analysis, where the probability of CO_2 leaving the surface as a function of incident O atom energy can be obtained. The gray carbon atom on the surface is considered as the reactive site for the trajectory simulations. Figure 2.10 shows that the probability of CO_2 leaving the surface due to collision is below 0.1 for an incident energy of 0.5 eV. The reaction probability increases to 0.3 at 1 eV and 0.7 at 5 eV. Similar trajectory and isolated defect analysis was performed for the dominant CO reaction shown in the inset of Fig. 2.9. Again, the C-C bond is very strong and the CO group is unable to leave the surface due to thermal excitation. For this mechanism, the incoming O atom adsorbs on the gray carbon atom and the CO molecule leaves the surface. As seen in Fig. 2.10 the probability of CO leaving the surface due to O atom impact is negligible below 1 eV and gradually rises to its maximum value for energies > 3 eV. It is noted, as seen in Fig. 2.10, that the maximum probability determined for each reaction is not the same. This is due to the impact parameter range used for the trajectories (i.e. the area centered at the defect within which trajectories are initialized). Although this may appear to be related to a pre-exponential factor for the reaction, such a determination requires a consistent treatment between the impact parameter range and a specific rate equation formulation, which is not a focus of this work.

In order to obtain the activation energy for the loss of a CO and CO_2 molecule from the edge of the etch pit as shown in Fig. 2.9, two model systems are considered representative of the carboxyl-like ($C_{53}H_{18}O_3$ + O) and carbonyl ($C_{49}H_{18}O_3$ + O) terminated edges shown in the inset of Fig. 2.9. These two model systems along with the mechanism for loss of a CO_2 and CO molecule are shown in Figs. 2.11 and 2.12, respectively. From Figs. 2.11 and 2.12, it is clear that the loss of both CO_2 and CO molecules from the edge of an etch pit in graphene is exothermic in nature. The energetics of these reactions are obtained by a two-step process which involves a low temperature (1 K) MD simulation to drive a reaction along the desired reaction co-ordinate followed by the energy minimization of the highest energy configuration along the reaction coordinate. For instance, in Fig. 2.11, the first step of the reaction leading to the loss of a CO_2 molecule involves the adsorption of an oxygen atom onto the carbon atom to which the carboxyl-like group is attached. This reaction is performed by slowly moving a

faraway oxygen atom towards the desired carbon atom in a low temperature (1 K) MD simulation. Then, the maximum energy configuration along this pathway is extracted and energy minimized while restraining the carbon-oxygen distance to that value of the reaction coordinate. This two pronged strategy provides a natural means of allowing the system to relax while a reaction proceeds along the desired pathway.

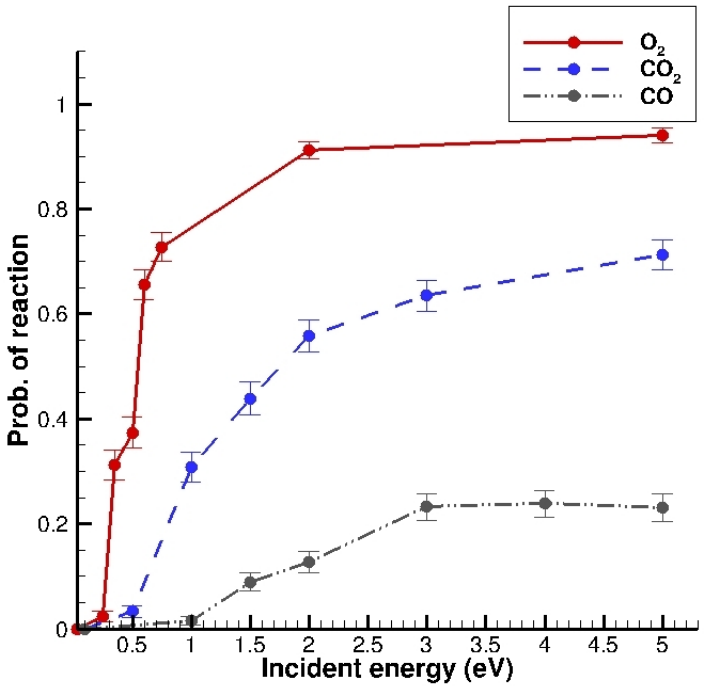

Figure 2.10: Reaction probabilities versus incident beam energy.

The reference configuration for the reactions leading to the loss of a CO_2 molecule (Fig. 2.11) and CO molecule (Fig. 2.12) was taken to be the respective model system with an oxygen atom far away from it. The relative energies of the intermediates along the reaction path with respect to the chosen reference are provided underneath each image in Figs. 2.11 and 2.12. From Fig. 2.11, it can be noticed that the adsorption of an oxygen atom onto the edge of the graphene etch pit has an energy barrier of 0.52 eV while the proceeding step (i.e. the desorption of the carboxyl-like group as a CO_2 molecule) is barrier less. The reaction on the whole is exothermic by 4.87 eV.

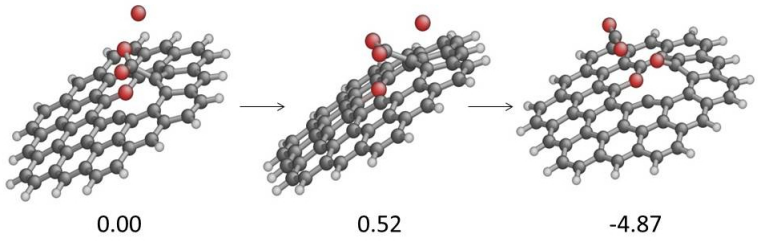

Figure 2.11: Sequence of reactions leading to the loss of CO_2 molecule from a carboxyl-like group. Image taken from Ref. [9].

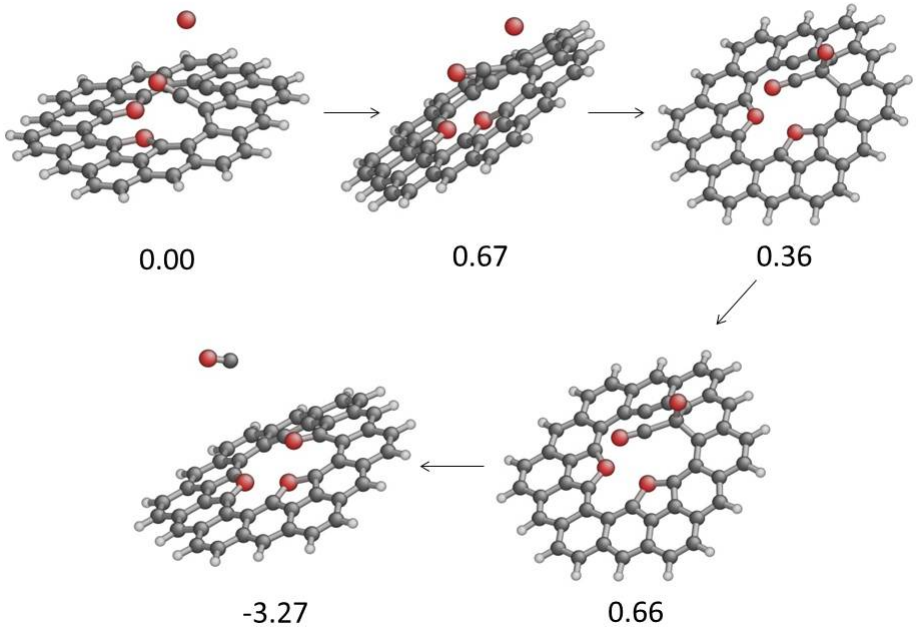

Figure 2.12: Sequence of reactions leading to the loss of CO molecule at the edge of a graphene etch pit due to the impingement of an oxygen atom. Image taken from Ref. [9].

Consistent with this energy barrier, the trajectory calculations predict a negligible probability of CO_2 loss below 0.5 eV (see Fig. 2.10). Above 0.5 eV, the probability of CO_2 loss increases rapidly, reaching an approximately constant value for energies above

3 eV. Figure 2.12 shows that the adsorption of an oxygen atom onto edge of the etch pit terminated by a carbonyl group has an associated energy barrier of 0.67 eV. This reaction is endothermic in nature with the adsorbed complex lying 0.36 eV higher in energy than the reactants. Subsequent loss of a CO molecule has an energy barrier of only 0.3 eV. Thus, the loss of a CO molecule due to the impact of an oxygen atom has an energy barrier of $\sim$0.67 eV, similar to that for CO_2 loss. The reaction on the whole is exothermic by 3.27 eV. The predictions from the trajectory analysis are consistent with an energy barrier of 0.67 eV associated with this reaction. It can be noticed that (see Fig. 2.10) the probability of loss of a CO molecule below 1 eV is negligible while the probability increases with increase in energy beyond 1 eV. The difference in reaction rate probability compared to CO_2 loss is likely due to the fact that the CO reaction is more complex, where energy must be channeled into overcoming two reaction barriers. Thus, the trajectory analysis suggests that the CO reaction has a smaller cone of acceptance compared to the CO_2 reaction.

In summary, the large-scale sequential collision MD simulations predict etch pit evolution, recombination rate, oxidation rate, and product species in good qualitative agreement with experimental measurements. Through more detailed analysis of the simulations, the precise active sites on a realistic oxidized HOPG surface and dominant reaction mechanisms are determined. The mechanisms are investigated using trajectory simulations in order to characterize the energy barriers for the dominant recombination and oxidation reactions on a realistic HOPG surface. The trajectory simulations are shown to be consistent with isolated defect analysis on smaller graphene sheet models, although they predict non-zero reaction probabilities over a range of impact energies due to geometrical effects of the etch pit edges at finite temperature. Overall, as evident in Fig. 2.10, recombination occurs everywhere on the oxygen covered graphene sheets with the lowest energy barrier. Oxidation reactions occur on the etch pit edges, where the dominant mechanism for CO_2 production has a lower energy barrier than that for CO production. At a beam energy of 5 eV however, all reactions occur with their maximum probability.

2.2.4 Interactions between oxidation products and the molecular beam

In addition to non-reactive oxygen scattering collisions, recombination reactions forming O_2, and oxidation reactions forming CO and CO_2, the sequential collision simulations

also predicted a small number of other oxidation products such as O-C-C-O and other larger molecules leaving the surface. In one simulation, 26 CO, 98 CO_2, and 7 larger molecules left the surface due to collisions. Since no other large-scale etch pit simulations have been performed in the past, such large molecule reaction products have not been reported in the computational chemistry literature. Also, the molecular beam experiments do not report detection of such larger molecules.

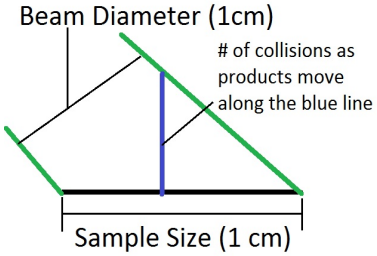

Figure 2.13: Schematic of interactions between O atoms in the beam and oxidized products leaving the surface.

It is possible that these larger molecules are an artifact of the ReaxFF C/H/O potential. However, it is also possible that these molecules leave the surface and proceed to interact (collide) with the O atoms in the beam before reaching the experimental detector. In order to assess this possibility, a simple kinetic theory analysis is performed to determine the probability that certain products that leave the surface react within the beam before escaping the near surface and reaching the experimental detector. For the analysis it is assumed that the surface oxidation products leave normal to the surface and from the center of the HOPG sample, on average. That is, products leave along the blue line as shown in Fig. 2.13 and may interact with the atoms in the beam during motion along this path. The number of reacting collisions (r) is then be given by [62] :

$$r = N \times f \times P \tag{2.2}$$

where N is the average number of collisions, f is the fraction of collisions with sufficient energy and P is the steric factor. From the beam experiments in Ref. [63], the number density of O atoms in the beam is obtained as $n = 2 \times 10^{18} m^{-3}$ and the velocity (c_b) of O atoms is obtained from the average translational energy of the beam ($c_b = 7937.25\ m/s$). Further, it is assumed that the oxidized products leave normal to the surface with an

average thermal velocity (c_p) at equilibrium with the surface temperature (500 K) which is equal to

$$c_p = \sqrt{\frac{8kT_s}{\pi m}} \tag{2.3}$$

where m is the mass of the oxidized product and T_s is the surface temperature.

Collision frequency and reaction probability for CO_2

The relative velocity (c_r) between CO_2 and O is $c_r = c_b cos(\Theta) + c_{p_{CO_2}}$, where ($\Theta = 45°$) which is the angle of the beam with the surface. The average time that CO_2 is present in the beam is $t = 1.02 \times 10^{-5}$ s. The frequency of collisions (ν) is given by $\nu = nc_r\sigma_T$, where $\sigma_T = \pi d_{ref}^2$ and d_{ref} is the collision cross-section [64] ($d_{ref_{CO_2}} = 5.62 \times 10^{-10}$ m). The average number of collisions experienced per CO_2 molecule is then given by $N = \nu t = 0.1235$.

Next, the fraction of collisions with sufficient energy to react is computed. Considering the combined K.E. (ϵ) of the two species (CO_2 and O) along the direction of line of centers [62],

$$\epsilon = 0.5 \times m_r[(c_{p_{CO_2}} cos(\theta) - c_b cos(45°))^2 + (c_{p_{CO_2}} sin(\theta) + c_b sin(45°))^2] \tag{2.4}$$

where, m_r is the reduced mass. Here, it is assumed that the velocity vector of the O atom has a fixed angle of 45° and that of CO_2 is θ with the horizontal. By varying θ in the interval $[0, \pi]$, $\epsilon_{max} = 4.32$ eV and $\epsilon_{min} = 3.51$ eV are obtained. For the reaction ($O + CO_2 \rightarrow CO + O_2$), the activation energy (E_a) from the chemical kinetic data [65] is 2.2827 eV and thus, the fraction (f) of collisions with sufficient energy for reaction is 1.

To compute the steric factor, the discussion in Ref. [66] is followed. By comparing the kinetic rate theory and Arrhenius rate equation, the pre-exponential factor (A) is:

$$A = \frac{P\hat{N}d_{ref}^2}{\Gamma(\frac{3}{2})}\sqrt{\frac{8\pi E_a}{m_r}} \tag{2.5}$$

where P is the steric factor, $\hat{N}$ is the Avogadro constant and Γ is the gamma function. The pre-exponential factor (A) is obtained from Ref. [65] and using the above equation, the unknown P is found to be 3.62×10^{-3}. Thus, the final average number of reacting collisions (r) for a CO_2 molecule is :

$$r = N \times f \times P \sim 4.47 \times 10^{-4} \tag{2.6}$$

Thus, on average very few CO_2 molecules would undergo a reaction within the beam.

Collision frequency and reaction probability for large product molecules

The average thermal velocity (c_p) of a large oxidized molecule (Molecular Weight $\sim$ 100 gm/mol) is of the same order as that of CO_2. A similar analysis could be performed as above for this molecule to obtain N. Although the exact value of d_{ref} cannot be determined for this large molecule, it is of the order of $10d_{ref_{CO_2}}$. Thus, the average number of collisions for the large molecule would be 100 times greater than that of CO_2. The activation energy for the reaction would be less and the steric factor of the reaction would be greater than that for the reaction of CO_2 with O and thus, it can be assumed that f and P are conservative. Therefore, the number of reacting collisions (r) in this case would be at least 100 times that of CO_2. The analysis indicates that the probability of a such a large molecule reacting within the beam prior to reaching the experimental detector is significantly higher than that for CO_2.

2.3 Conclusions

Large-scale molecular dynamics simulations are performed of HOPG exposed to a 5 eV atomic oxygen beam, matching the experiments of Nicholson, Minton, and Seibner [8, 40]. Since both the HOPG surface and the atomic beam are well-characterized at the atomic level, direct comparison of reacting Molecular Dynamics simulations with experimental data is possible. The MD simulations are performed using the C/H/O ReaxFF parameter description developed by Chenoweth *et al.*[51], which in previous studies, has been shown to reproduce experimentally observed chemical changes during the reduction of graphene oxide[56] and DFT data on the chemical events occurring during the hyperthermal oxidation of graphene[47]. In the present work, the C/H/O ReaxFF potential is further validated by demonstrating close agreement with *ab-initio* energies for the heterogeneous evolution of a CO_2 molecule from a naphthoxy radical upon exposure to atomic oxygen; a relevant interaction for the current study. In contrast to prior numerical studies for this problem [23, 47], HOPG is simulated as a large multilayered graphene slab ($\approx$ 3000 atoms), which furthermore, is exposed to a large number of sequential atomic oxygen impacts, thereby enabling simulation of etch pit evolution. The frequency of collisions and the temperature of the simulated HOPG are

carefully controlled to realistically represent experimental conditions.

The large scale MD simulations predict no carbon removal from pristine HOPG even with 5 eV impacts. Rather, O atom beam exposure first establishes an oxygen coverage of epoxide and C-O groups. These groups act as precursors that reduce the energy barrier for reactions involving the removal of a carbon atom. After the first such reaction, a defect is created in the top graphene layer and subsequent collisions impacting the vicinity quickly lead to increased carbon removal and rapid growth of an etch pit. Once exposed, HOPG sub layers also develop an oxygen coverage and initial defects due to carbon removal reactions, although the intra-planar reaction rate is much faster than the inter-planar rate. The result predicted by the MD simulations is a wide but shallow cylindrical etch pit, in qualitative agreement with experimental observation.

A steady-state rate of carbon removal from a heavily oxidized HOPG surface (an etch pit) is eventually reached during long time scale MD simulations, in qualitative agreement with experiment. Despite disparate length scales, it is possible that the precise chemical reactions occurring on the edges of the simulated ($O(nm)$) etch pit are identical to those occurring on the ($O(\mu m)$) etch pit edges in the experiment. Due to the disparate length scales, quantitative comparison with experimental etching rates are not possible. However, the fraction of CO_2 to CO reactions predicted by the simulations was found to be 4:1, in good quantitative agreement with the experimentally measured value of 2:1. Furthermore, the simulations predicted a much higher percentage of O_2 products (due to recombination reactions) compared to CO_2 and CO, consistent with the experiment.

The dominant chemical mechanisms leading to the production O_2, CO_2 and CO were isolated on the actual oxidized HOPG surface (a simulated multilayer etch pit) and further investigated using trajectory analysis to obtain probabilities of reaction versus incident O atom energy. The dominant recombination reaction producing O_2 required impact energies greater than 0.3 eV, while the dominant reactions leading to CO_2 and CO required energies greater than 0.5 eV and 0.67 eV, respectively. These trajectory calculation results on the fully oxidized HOPG etch pit were shown to be consistent with an activation energy analysis on isolated defect model chemistries. The trajectory analysis revealed lower probabilities of CO loss compared to CO_2 loss since energy is channeled into overcoming two reaction barriers for the CO reaction. The overall number of carbon-removal reactions was determined to increase with increasing surface

temperature, a trend also observed experimentally. Since the thermal energy of the surface is insignificant compared to the beam energy, both simulation and experimental results indicate that "thermal" reactions (not a direct result of a collision) contribute significantly to the overall etching process (approximately 50% of simulated reactions were "thermal"). Further effort, and an alternate simulation technique, is required to fully characterize these reactions.

Overall, the qualitative and quantitative agreement between MD simulation and experiment is very promising. Thus the MD simulation approach and C/H/O ReaxFF parametrization may be useful for simulating high-temperature gas (or high energy beam) interactions with graphitic materials where the micro structure is more complex than HOPG. For such materials, it is possible that despite more complex micro structure, the local chemistry leading to recombination and oxidation reactions is similar to that of HOPG etching.

Chapter 3

Effect of Microstructure

This chapter aims to analyze and understand the second aspect of ablation, namely the diffusion of reactive gas species within the ablator microstructure and it's effect on oxidation. Ultimately, understanding of this second aspect could connect information regarding chemical reactions at the atomistic scale to macroscopic surface reaction mechanisms and rates used within continuum flow solvers where microstructure is not explicitly modeled. In non-porous ablators, the matrix and the fiber are carbon based, thus the reactivity of fiber and the matrix are similar but the matrix has lower density and ablates faster compared to the fiber [10]. The fibers or the granules protrude into the flowfield exposing the microstructure of the TPS to gaseous species as shown in Fig. 3.1. The morphology and surface area of the microstructure that is exposed into the flowfield may affect the magnitude of ablation under different regimes.

Micro-scale analysis has been previously performed on porous ablators. Lachaud and Vignoles [67] developed a Brownian motion technique to study the diffusion of oxygen through porous ablators. Lachaud *et al.* [68] have investigated the in-depth ablation due to the diffusion of oxygen inside the ablator resulting in volume ablation of the fibers and derived a volume averaged model for the oxidation process. More recently, Lachaud and Mansour [69] have used the Brownian motion technique to demonstrate temperature regimes where the diffusion of oxygen atoms through the microstructure is critical to the oxidation process.

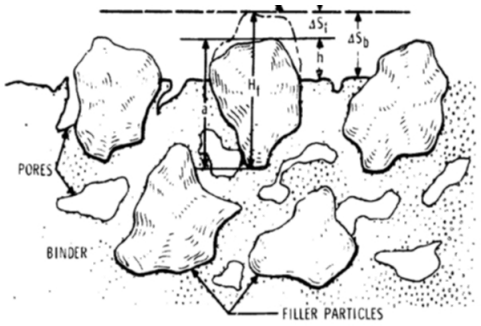

Figure 3.1: Schematic of microstructure in the flowfield [10, 11].

Martin [70] coupled the volume averaged model with a material response code and observed that the oxygen penetration is higher than previously reported by Lachaud *et al.*. Experimental studies, in an inductively coupled plasma jet facility, of carbon fiber preform [71] observed needle-like fibers resulting from the oxygen diffusion process, and also observed in-depth pitting of the fibers, also observed by Panerai *et al.* [72] in side-arm reactor experiments. Recently, experimental work by Panerai *et al.* [73] to obtain tomographic images of carbon fiber preform have made it possible to simulate the flow of gases through realistic porous ablator geometries to understand the reaction/diffusion processes occurring at the micro-scale.

In porous ablators the diffusion of gases through the pores supply reactive species along the entire length of the carbon fibers resulting in volume ablation. This is fundamentally different from the non-porous ablators where the ablation process is still a surface phenomena but the surface is modified due to the protrusion of the fibers or granules in the flowfield. The mechanical failure of the exposed microstructure where the shear stress and the pressure drag removes the exposed microstructure from the surface has been studied by Gosse and Candler [10] and also observed by McVey *et al.* [11] and Zeiring and DiCristina [74]. However, the effect of the microstructure on the concentration of oxidized products in the boundary layer has not been examined before.

The focus of this chapter is to simulate and analyze the flow around a non-porous 3D C-C microstructure using direct simulation Monte Carlo (DSMC) [64]. DSMC is an accurate flow model for conditions ranging from continuum to free-molecular, and therefore provides an accurate model for the entire boundary layer including flow within the

microstructure, where the size of the fibers may approach the mean-free-path of the flow. The work is a qualitative parameter study on the effect that material microstructure has on the chemical composition of the boundary layer. The DSMC method naturally lends itself to the simulation of flows on micro-scales as those occurring at the surface of a carbon based ablator because the small length scales can be resolved and at small length scales, the continuum approximation may not be valid entailing a need for particle based technique is to simulate the flow.

The reaction rates observed macroscopically is a combination of the atomistic gas-surface reaction, diffusion of reactive species and gas-phase reactions that would occur within the microstructure. An effort to quantify the rates would require accurate modeling of gas-surface chemistry and gas-phase chemistry occurring within the microstructure which is not a focus of the work in this chapter. This chapter is focused on understanding the underlying physics and obtaining qualitative features of the flow characteristics that have to be accounted for while designing a new model and creating a framework within DSMC where the complexity required can be added sequentially. This would eventually combine all the aspects required to help improve the quantification and modeling of the reaction rates occurring during ablation.

3.1 Simulation Description

The flow around the microstructure of 3D C-C is simulated. 3D C-C can be further classified into Biaxial3D, Triaxial3D, Cartesian3D and Polar3D based on the weave characteristics. The most widely used 3D C-C ablator is Cartesian3D where the carbon fibers are aligned along the three orthogonal directions [75]. Different quality of carbon composites can be obtained by changing the fiber diameter and spacing, and typically a number of individual fibers are arranged in cylindrical fiber bundles. Currently, such fiber bundles (simply referred to as fibers for the remainder of the paper) are simulated as cylinders of 1 mm diameter, aspect ratio of 1:6 (diameter:height) and the microstructure consists of several such fibers equally spaced (by 1 mm) along the x-axis, with their main axis aligned with the y-axis. In the work of Gosse and Candler [10], a discussion is entailed of the mechanical failure of the fiber. A fiber that protrudes into the flowfield can be considered as a cantilever beam fixed at one end and at a certain critical height the pressure drag and the shear stress from the flow pull the fiber away from the surface

which is not accounted for in the current study.

The parallel Molecular Gas Dynamics Simulator (MGDS) [76] code developed at University of Minnesota is used which has a multi-level cartesian grid [77] for the flowfield and a robust cut-cell algorithm to identify a surface in the flowfield [78]. The algorithm determines a surface by computing the intersection of the triangles with the cartesian cells. In a given timestep, the gas particles in a cell collide with each other exchanging momentum and energy and move with the post-collision velocities. When a gas particle in the flow collides with the surface, it reacts with a specified microscopic probability (r) [79]. A random number is generated and if the specified reaction probability is greater than the random number, the reaction is performed. The reaction product or the colliding gas particle leaves the surface with diffuse reflection and thermally accommodated to the surface temperature. It is important to note that the microscopic reaction probability (r) is different from the macroscopic reaction probability (α) which is obtained empirically and accounts for both the atomistic chemistry and the microstructure morphology. The probability (r) used in the DSMC simulations accounts only for the atomistic chemistry occurring at the fiber surface. In the current study, simulations are performed with specified reaction probabilities but probabilities from atomistic simulations [9] could be included in future. The reaction C(s) + O $\rightarrow$ CO is modeled and the concentration of O and CO are analyzed for different probabilities and different microstructures with varying surface area. Two different simulations are performed;convection-diffusion within a boundary layer and isolated diffusion.

3.1.1 Convection-Diffusion Setup

A supersonic inflow ($M_\infty = 2.0$) at high temperature (7500 K) is allowed to develop over a flat plate and microstructure, where the fibers of the microstructure are contained within the boundary layer as shown in Fig. 3.2. The flow conditions are arbitrarily chosen to ensure fully dissociated oxygen atoms and a supersonic inflow. The enthalpy of the flow is higher than those experienced by typical hypersonic vehicles but the focus of this work is only to understand the qualitative behavior of surface oxidation when microstructure is accounted for. The microstructure (carbon fibers) that are modeled as cylinders start at x=0.2 m. The inflow velocity (5000 m/s), temperature (7500 K) and density(3×10^{-4} kg/m^3) are prescribed at x=0.0 and y=0.1. Symmetric boundary conditions are applied in the z direction. At the inlet (x=0.0, y=0.1) oxygen atoms are

regenerated every timestep based on inflow density and velocities are assigned to each atom. The velocities have two components, mean inflow velocity and thermal velocity corresponding to the inflow temperature which is obtained from the Maxwell-Boltzmann distribution. The cell spacing is fixed to 1 MFP (mean free path) and timestep to 0.05 MCT (mean collision time) of oxygen atoms corresponding to the given temperature and density. The surface temperature is fixed at 1500 K.

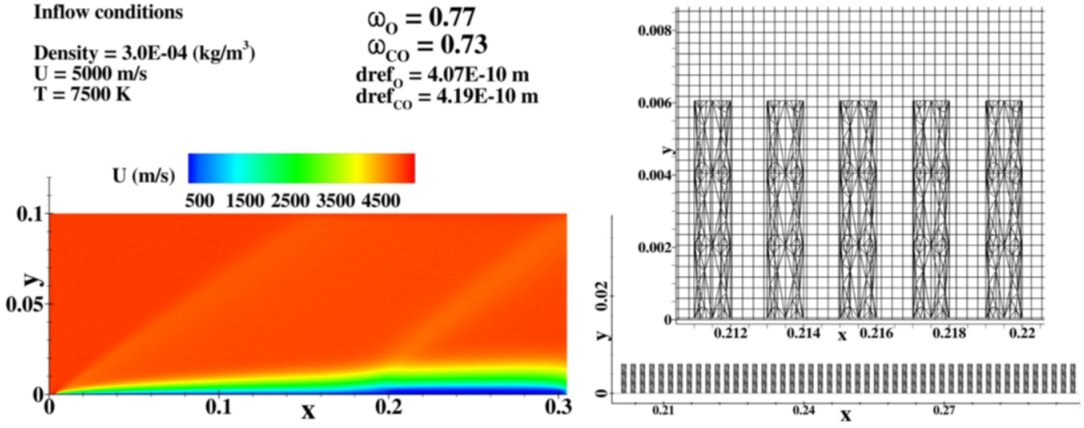

Figure 3.2: Description of the simulation setup to analyze the combined effects of convection and diffusion.

The sampling is done after observing that the total number of particles in the domain are roughly constant which occurs after 100,000 timesteps and flow statistics are collected for 400,000 timesteps. The concentration profile of CO and O at a given x-location have been compared for 400,000 sampling timesteps and 900,000 sampling timesteps to verify convergence to a steady state. Figure 3.3 shows that converged statistics are obtained after 400,000 timesteps and the concentration profiles only differ very close to the

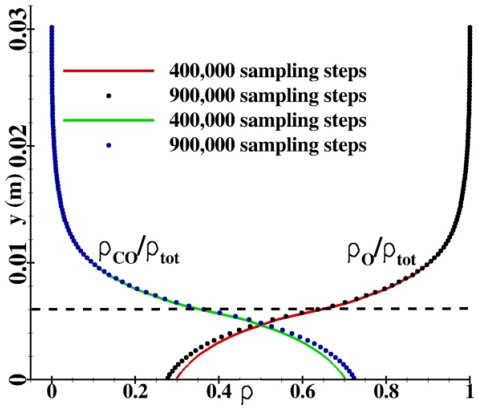

Figure 3.3: Two sampling timesteps are compared at x=0.2343 m with r = 0.0029 to verify the convergence of simulation.

bottom of the microstructure.

These simulations help to analyze the combined effect of convection and diffusion of gases around the microstructure. The oxygen atoms would diffuse around the microstructure and react to form CO as it collides with the surface. As the product of oxidation (CO) diffuses into the boundary layer, the high mean velocity would convect away CO and an interplay of the two factors would be observed. Three different surface reaction probabilities are analyzed and three different microstructures with different spacing and fiber diameter are also analyzed for a given probability. The results for these simulations are discussed in Section 3.2.

3.1.2 Isolated Diffusion Setup

The diffusion of gases within the microstructure (fibers) and subsequently into the boundary layer is critical to understanding the production and concentration of CO in the boundary layer. An infinite array of equally spaced fibers are simulated using a small symmetric simulation domain with no bulk velocity, shown in Fig. 3.4. Symmetric boundary conditions are applied along the x and z directions. The cell spacing, timestep, wall temperature and gas-surface reactions are similar to that explained in the previous section.

At y_{max}=0.02, a flux of oxygen atoms is specified based on the inflow density. The velocities of the oxygen atoms have two components; a thermal velocity corresponding to the inflow temperature as described before and a mean velocity of 0 m/s to neglect convection. The oxygen atoms are regenerated every timestep at y=0.02. Oxygen atoms diffuse into the domain (initially

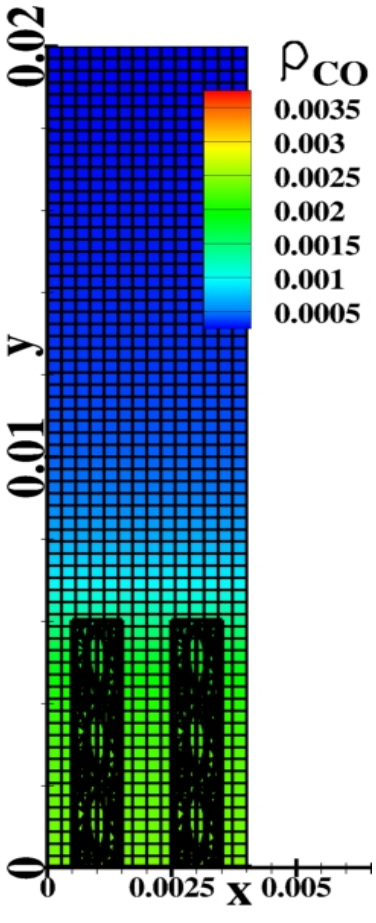

Figure 3.4: Description of the simulation setup to analyze the effect of diffusion.

evacuated) resulting in CO production as they start colliding with the surface. The domain will begin to fill with CO products introducing a changing concentration gradient as CO molecules diffuse upwards and O atoms diffuse downwards. The concentration profiles resulting from all simulations for various microstructures and microscopic probabilities are compared at the same physical time. First, different microscopic probabilities are analyzed on a single microstructure and thereafter several different microstructures with varying surface area are considered.

3.2 Results

3.2.1 Convection-Diffusion Results

The effect of microscopic probability (r) is initially examined. The macroscopic surface reaction probability (α) from Park's model for C + O $\rightarrow$ CO is given by 0.63exp(-1160/T_w). At $T_w = 1500$ K, the probability is 0.29 and it is used for the initial calculation. This probability, which is inferred empirically and therefore includes microstructure effects, is likely much higher than the actual microscopic reaction probability that should be applied for each particle-surface collision. Thus, to analyze the consequence of the microscopic reaction probability (r), three cases are analyzed with r = $0.29, 0.029$ and 0.0029 to investigate high, intermediate and low probability respectively.

Fig. 3.5 shows the density profile of CO at various x-locations perpendicular to the flow for $r = 0.0029$.

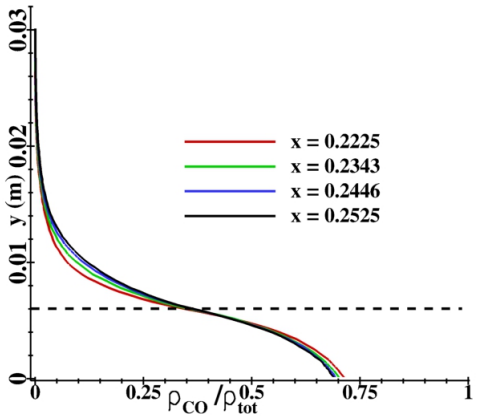

Figure 3.5: Comparison of CO density profiles at various x-locations.

It can be seen that the variation in concentration profiles above the fibers in the boundary layer (y>0.006 m) is very small indicating that the gradients along the flow direction are negligible. This is expected because the fibers are uniformly spaced and the gradients in the streamwise direction for this flow should be small. This also indicates that a profile extracted at a single x-location is sufficient to study the boundary layer behavior. This result is also verified for the other two probabilities.

The CO and O density profiles at x = 0.2343 m are compared for the three probabilities in Figs. 3.6 and 3.7 along with that of a flat plate which is located at y=0.006 m (the height of the fibers). It can be seen from the figures that when r is high (0.29), the O concentration within the microstructure is small and the CO concentration is high indicating that most of the oxygen atoms that have diffused into the microstructure have reacted to form CO. This suggests that at high reaction probability, the oxidation process is not sensitive to the probability and the oxidation is primarily diffusion limited. This has been previously observed by Driver *et al.* [80] where CO formation is analyzed using the DPLR (Data Parallel Line Relaxation) code with reaction probability of 0.9. Interestingly, a similar feature is also seen for the flat plate simulations where the concentration of oxygen at the wall is very low creating a very high species gradient in the boundary layer.

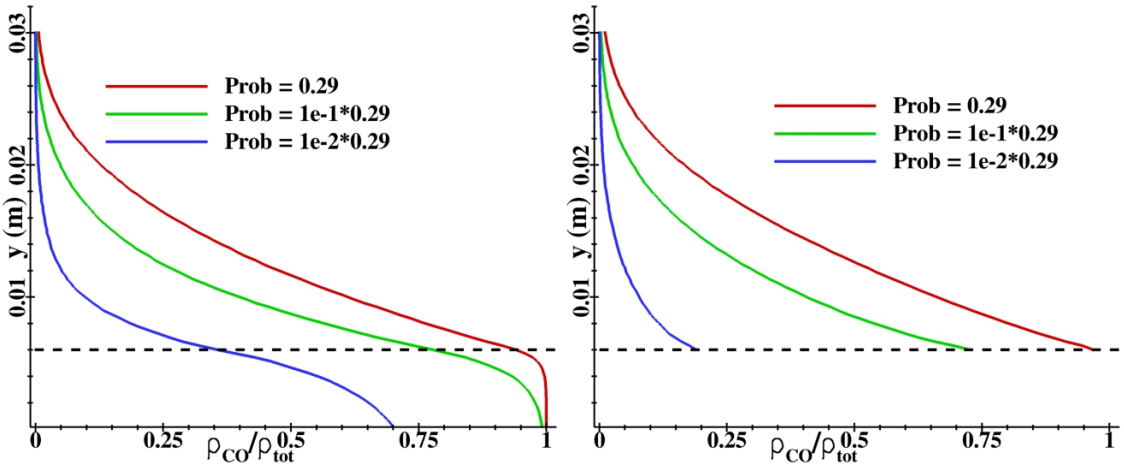

Figure 3.6: Comparison of CO density profiles for three different surface reaction probabilities of the microstructure and plate.

To determine the effect of microstructure surface area, two different microstructures

(shown later in Fig. 3.10) are simulated with twice the surface area and half the surface area of the initial microstructure. A similar concentration profile is observed for all three microstructures (Fig. 3.8) substantiating that the effect of surface area is negligible when microscopic probability is high. In fact, the CO concentration for the flat plate simulation is seen to be slightly higher than for all three microstructure simulations throughout the boundary layer. This is attributed to the fact that the boundary layer is shifted towards the surface slightly for the microstructure simulations compared to the flat plate fixed at the fiber tips. Therefore, it can be concluded that the concentration profiles for the flat plate and all three microstructures are very close when the microscopic probability is high.

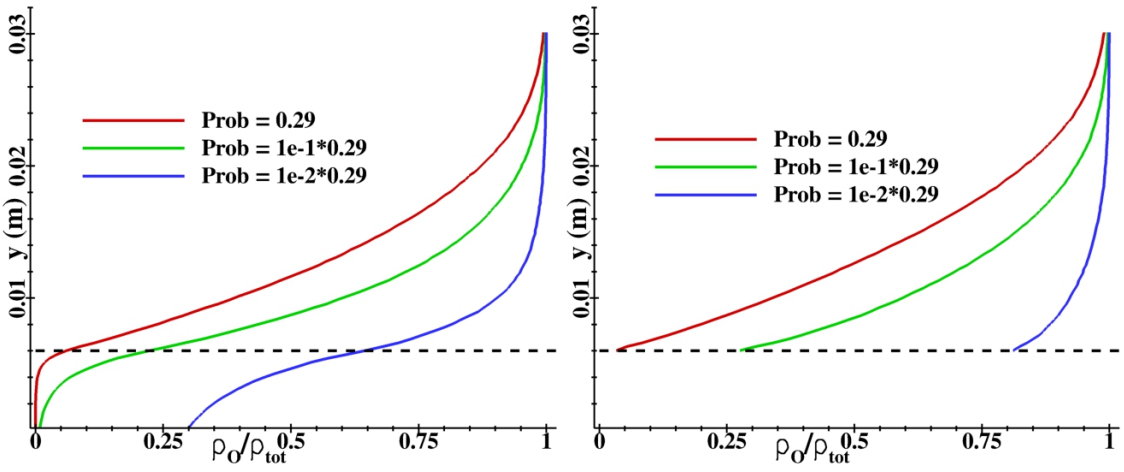

Figure 3.7: Comparison of O density profiles for three different surface reaction probabilities of the microstructure and plate.

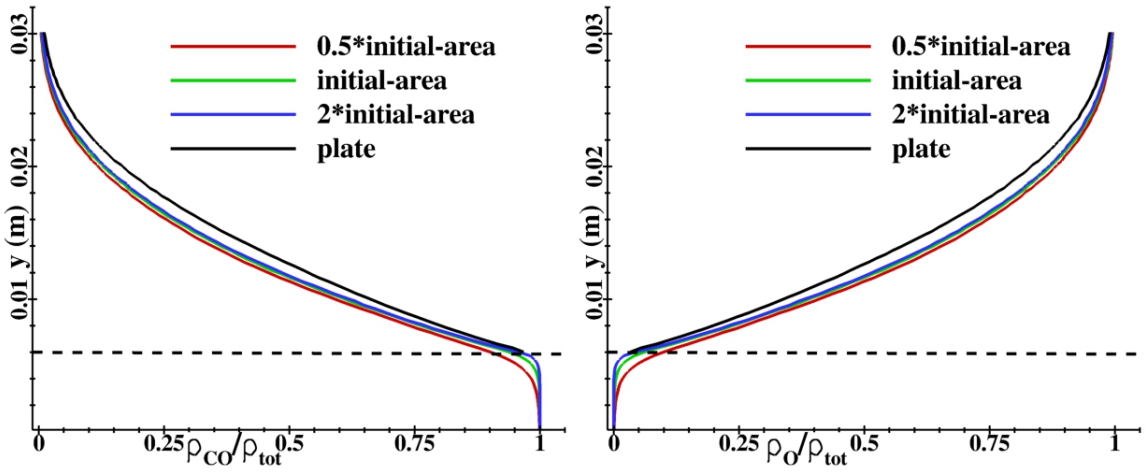

Figure 3.8: Comparison of CO and O density profiles for three different microstructures and plate at r=0.29.

At low reaction probabilities (0.0029), the concentration of oxygen atoms within the microstructure is not negligible indicating that all the oxygen atoms that diffused into the microstructure do not react. This is significantly different from the high probability simulations where the CO production is diffusion limited. Here, the CO production is rate limited and the reactive species collides several times with the surface before it reacts. Therefore, an increase in available surface area for collisions would lead to higher production of CO. Three different microstructures are examined similar to the the high probability study and the concentration profiles are shown in Fig. 3.9. It can be seen that an increase in surface area results in higher CO production. Moreover, unreacted oxygen atoms are also present within the microstructure and the concentration of oxygen atoms is comparable to CO indicating that a mixture of CO and O are present within the microstructure as opposed to the high probability case where almost no oxygen is present within the microstructure. As expected, the concentration of CO in the boundary layer for the flat plate simulation is now less compared to the microstructure simulations.

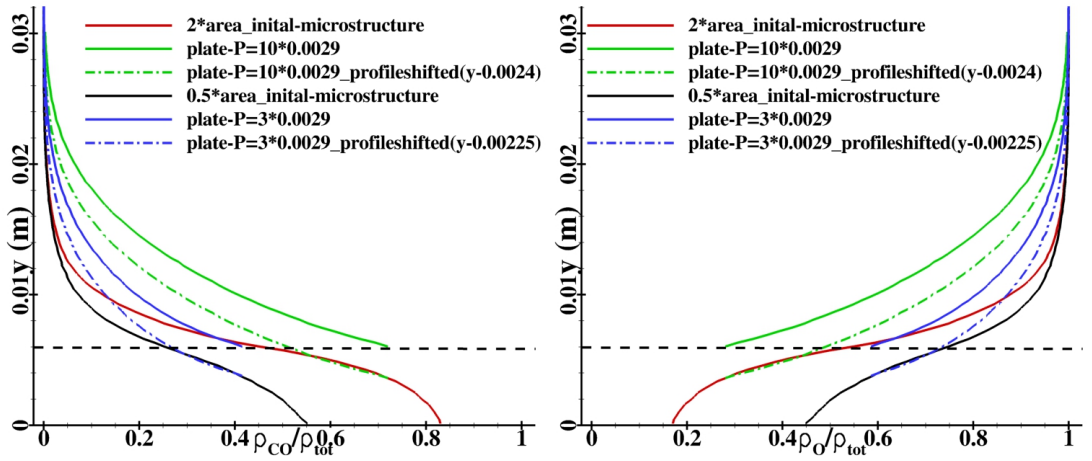

Figure 3.9: Comparison of O and CO density profiles for different microstructures and plate at r=0.0029.

One objective of this work is to connect microscopic reaction probabilities (atomic-level information) to macroscopic reaction rates to be used in CFD and material response solvers. It is evident that surface probabilities obtained from atomistic simulations cannot be used directly without modifying the probability to account for (at a minimum) the microstructure surface area. For this purpose, two more simulations are performed with a flat plate at y=0.006 m where the reaction probabilities are 3×0.0029 and 10×0.0029 respectively and the profiles are compared in Fig. 3.9. The profiles are also compared by shifting the flat plate profiles by a certain distance vertically (2.225×10^{-3} m for 3×0.0029 and 2.4×10^{-3} m for 10×0.0029). It is found that the shifted profiles agree with the microstructure profiles in a region below the tip of the fiber ($y \leq 0.006$ m) but not above. The differences in profile above the microstructure could be due to the convective effect which acts differently for the flat plate and the microstructure as discussed before. The profiles also show that CO concentration for the microstructures are lower compared to the flat plate concentrations in both cases (3×0.0029 and 10×0.0029). Although the concentration profiles in the boundary layer could not be matched, the microstructures could be replaced with an equivalent flat plate where the microscopic reaction probability is modified by a multiplying factor between $3 - 10$ as a conservative estimate.

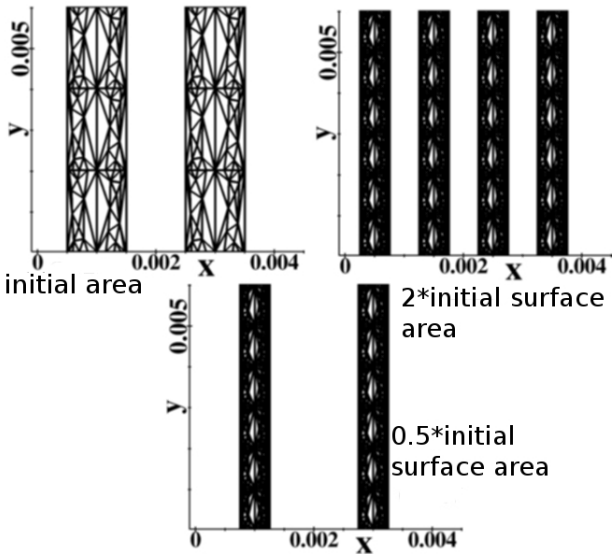

Figure 3.10: Different microstructures that are simulated.

To summarize, at high surface probabilities (0.29), the oxidation process is diffusion limited where the CO production is influenced by the diffusion of reactive species (O atoms) from the boundary layer into the microstructure region, but is not influenced by the details of the microstructure itself or the microscopic surface reaction probabilities. However, at low probabilities (0.0029), the oxidation process is rate limited where several collisions of the oxygen atoms with the surface are needed for the reaction to occur and the CO production is dictated by both the microscopic reaction probability and the surface area of the microstructure. In order to approximate the microstructure with an idealized flat surface, the reaction probability (α) could be 10 times larger than the microscopic probability (r) for the microstructures considered. Furthermore, the concentration profile within the boundary layer of a microstructure simulation could not be matched with a flat plate approximation even after adjusting the surface reaction probability in this manner.

3.2.2 Isolated Diffusion Results

The effect of diffusion within the microstructure is studied by isolating a small substructure from the big microstructure within a symmetric domain (Fig. 3.4) and allowing O atoms to diffuse into the domain with their mean thermal speeds. This allows us to

understand the diffusion process alone by neglecting the convection effects which affects the concentration profiles as seen in the previous section.

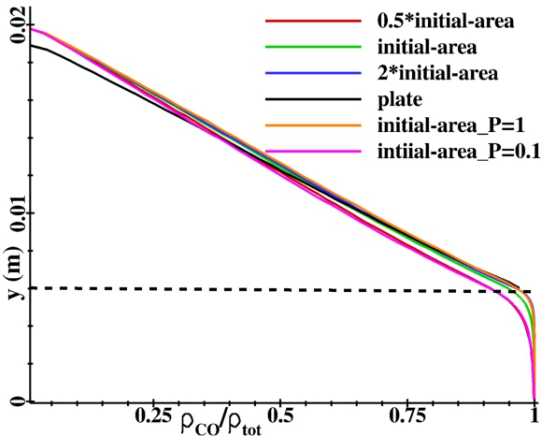

Figure 3.11: Comparison of CO profiles for different microstructures at r=0.29.

The diffusion study confirms the previous observation that surface reactions at high probability (r=0.29) are diffusion limited and very few collisions are needed for surface reactions to occur. Fig. 3.11 shows the concentration profiles for r = 0.29 and it indicates that when the surface area is 2 times larger or smaller, the concentration profiles are similar. This further validates the observation that when the reaction probability (r) is high, the effective increase in surface area does not increase the concentration of CO. As seen in the convection-diffusion study, the mass fraction of CO within the microstructure is very high with very little or no oxygen atoms present within the microstructure. Two other simulations are performed with the probability of surface reaction as 1 and 0.1 respectively to examine the sensitivity of reactions at high probabilities. It can be clearly seen from Fig. 3.11 that overall CO concentration is not sensitive to the changes in probability when the reaction probability is high. As observed before, the concentration of CO in the boundary layer for a flat plate simulation is similar to the three microstructure simulations. This result further illustrates that when reaction probability is high, microstructures do not affect the concentration of oxidation products.

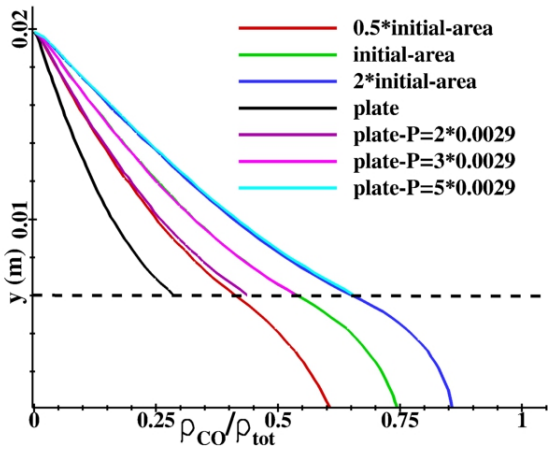

Figure 3.12: Comparison of CO profiles for different microstructures at r=0.0029.

As seen in the previous section, the simulations at low probability (0.0029) are predominantly rate limited and significantly different from high probability simulations. This is verified again through the diffusion simulation. A notable difference is seen in the profiles between the three microstructures (Fig. 3.12) and the concentration profile of the flat plate simulation is now lower compared to the other three microstructures. It substantiates the previous observation that oxygen atoms collide several times with the surface before reacting to form CO and as expected, there is a comparable mixture of CO and O within the microstructure and not all of the oxygen atoms that diffuse into the microstructure react.

As discussed before in the convection-diffusion section, the microstructure could be replaced with an equivalent flat plate where the rate from atomic calculations could be modified with a multiplying factor to account for the microstructure. To examine the effect of probability, three simulations of the flat plate are performed with probabilities 2×0.0029, 3×0.0029 and 5×0.0029 respectively. First, it can be seen from Fig. 3.12 that the CO profile resulting from a flat plate simulation can be matched to the profile in a microstructure simulation as long as the surface reaction probability is adjusted. Thus, the disagreement between flat plate and microstructure profiles shown earlier in Fig. 3.9 is likely due to differences in the convective-behavior of the boundary layers above a flat plate and above a microstructure. This behavior will be dependent on the size of the microstructure compared to the boundary layer height, which in our simulations is set arbitrarily to be approximately 40%.

The total CO produced during the diffusion simulations (number of CO molecules created at the surface during the simulation time) is also compared when using the low probability in Table 3.1 and several interesting features can be observed. First, when the surface area is increased, a change in CO production is observed. However, an increase in surface area by 200% (2*initial-area) only results in an increase of CO concentration by 26%. To understand this observation, the concentration of CO for the flat plate cases are compared. As expected, in the flat plate study a 3-fold increase is seen in the concentration when the probability is increased by a factor of 5 but when the probability is increased to $0.0145(5 \times 0.0029)$ for the microstructure, the increase in CO concentration is only 67% which clearly suggests that an increase in reaction probability or surface area of the microstructure does not result in an equivalent increase in the production of CO due to diffusion processes inside the microstructure. Also, different microstructure geometries with fibers aligned along different directions with the same surface area could result in different CO production and a surface area correction to the microscopic probability may not be sufficiently general to accurately model the macroscopic surface reaction rate.

Table 3.1: Comparison of total CO produced with respect to the initial microstructure and flat plate at r =0.0029.

Simulations (microstructure)	$[CO]/[CO]_{initial}$	% change
initial-area	1	-
0.5*initial-area	0.769	-23.14
2.0*initial-area	1.26	26.02
initial-area-Prob=5*0.0029	1.617	61.74
plate	0.326	-67.43

Simulations (flat-plate)	$[CO]/[CO]_{plate}$	% change
Prob=0.0029	1	-
Prob=2*0.0029	1.699	69.9
Prob=3*0.0029	2.2167	121.68
Prob=5*0.0029	2.9346	193.462

The effect of increasing microstructure surface area is also shown in Fig 3.13 for low probability. Surface area ratio of 1 corresponds to the initial microstructure. It can be seen that the CO concentration initially increases quickly when the surface area is increased but the increase gets slower as more fibers are added to the domain and the total production plateaus at high surface areas. A similar effect has been observed by Thoemel *et al.* [81] for catalysis on silica-based surfaces. It can be seen that an increase in 10 times the surface area has only resulted in 1.8 times increase in CO production. Moreover, when the surface area increases to 7.6 times the original area, almost no oxygen is present within the microstructure and the profile obtained is similar to the high probability case. The CO profiles when the surface area is 7.6 and 10.73 are similar which is analogous to the high probability case where surface area or the microstructure had minimal effect on CO production which reiterates previous observations that increase in surface area does not result in an equal increase in the reactive surface area.

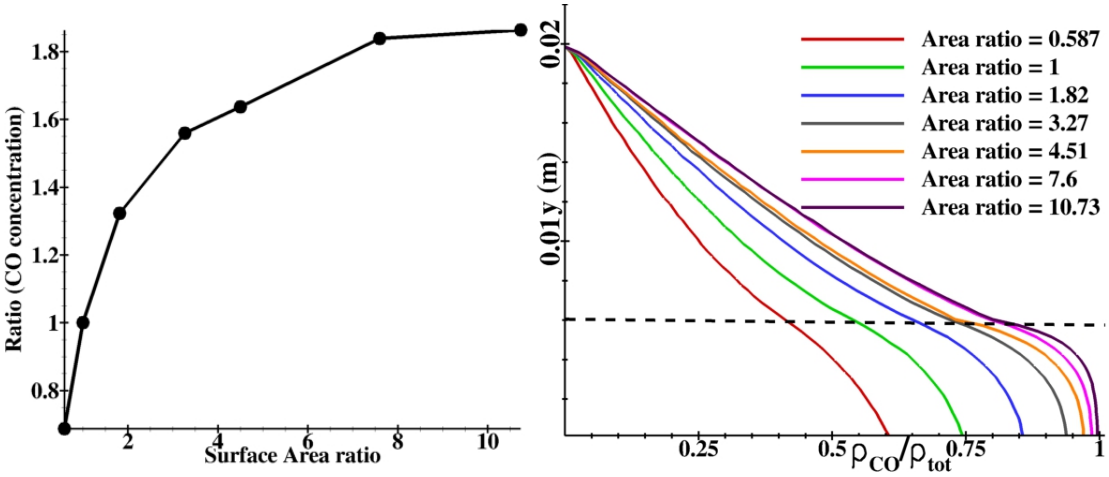

Figure 3.13: Comparison of CO density profiles and CO concentration for different microstructures at r=0.0029.

3.3 Conclusions

In this chapter, DSMC has been used to simulate flow around the microstructure of a non porous carbon ablator that protrudes into the flowfield to understand its effect on

macroscopic reaction rates. Two different studies are performed; convection-diffusion where a high temperature supersonic flow is simulated to analyze the combined effect of convection and diffusion and isolated diffusion where a small substructure from the entire microstructure is isolated to neglect any effects of convection.

The surface oxidation reaction to form CO is modeled with three different microscopic probabilities, $r = 0.29, 0.029, 0.0029$ which covered the high, intermediate and low probabilities respectively. The reaction at high probability is predominantly diffusion limited and almost no oxygen is present within the microstructure. Changing the surface area of the microstructure or the reaction probability to 1 and 0.1 also does not have an effect on the concentration profiles. However, the reaction at low microscopic probability (0.0029) is significantly different from high probability and is rate limited where different microstructures produce different CO concentrations. Concentration profiles of the microstructure and flat plate are matched by adjusting the probability for the flat plate in the diffusion study but could not be precisely matched in the boundary layer for the convection-diffusion study. Further, as total surface area increases, the total CO produced plateaus, exhibiting that an increase in surface area does not result in an equivalent increase in reactive surface area.

This preliminary study has helped to understand the qualitative features of the effect of microstructure on the concentration of reaction products in the boundary layer. In future, the simulations will be extended to study the effect of density to analyze the continuum and the rarefied regime along with realistic microstructures where the fibers align along different directions. A gas-surface reaction model for DSMC will also be developed where the reaction probability would be a function of the energy of incident atom, surface atoms and the atomistic chemistry that dictates the reaction. Quantification of macroscopic rates for reactions occurring during the ablation process.

Chapter 4

Molecular Beam Data Analysis

Computational studies performed using MD were discussed in Chapter 2. In the study for HOPG at low surface temperature (500 K), large MD simulations qualitatively reproduced experimental data from molecular beam experiments. However, due to computational expense limitations, MD simulations are only capable of capturing phenomena that occur over a timescale of nanoseconds. Whereas, as discussed in this chapter, molecular beam experiments performed at high surface temperature clearly show that most surface reactions are thermal [24, 25]. That is, the reaction products leave thermally accommodated to the surface over much longer timescales than those that are accessible to MD simulations.

Molecular beam experiments from Murray and co-workers [24] have provided many details about the precise chemical reactions occurring between gas-phase atomic oxygen and a vitreous carbon surface at high temperatures. These measurements clearly show that the majority of surface reactions are thermal reactions that are not dependent on the beam energy. Rather, the beam simply provides a source of oxygen to the surface and reactions are driven by the surface coverage and surface temperature. Also, despite near-vacuum conditions in the molecular beam facility, the oxygen coverage on the carbon surface is high. As discussed, the surface reactions and measured products may therefore be directly relevant for boundary layer conditions expected under hypersonic conditions. Although MD simulations could be useful to understand the molecular beam results at some point in the future, the experimental results themselves contain a large amount of data that can be directly used to formulate finite-rate gas-surface models for DSMC and CFD.

In this chapter, for a single surface temperature of 800 K, molecular beam data is used to develop a surface reaction probability model. The surface reaction probabilities obtained from the molecular beam experiments are incorporated into DSMC simulations of gas flows over realistic microstructure, now including gas-phase chemical reactions.

The chapter is organized as follows. Section 4.1 describes the experimental measurements and the reactive scattering data set, and also discusses the assumptions involved in incorporating the molecular beam data within DSMC simulations. Section 4.2 details the surface reaction probabilities used in DSMC, the description of the microstructure that is resolved and the details of DSMC models used. Section 4.3 presents DSMC simulation results for diffusion, convection, and gas-phase reaction processes at near-surface conditions. Section 4.4 describes the method to obtain the microstructure of a *real* ablator and simulate flow over them using DSMC.

4.1 Molecular Beam Experiments

The experiments were performed with the use of a crossed molecular beam apparatus [82, 83] that was configured for beam-surface scattering [24, 84]. The laser-detonation atomic-oxygen beam source that was used is based on an original design by Physical Sciences, Inc. [85] and has been further refined in the laboratory at Montana State University [24, 83, 84]. A pulsed beam of atomic and molecular oxygen, traveling at a nominal velocity of ~ 7756 m s^{-1}, was directed at a vitreous carbon (VC) surface that was resistively heated to high temperatures. The samples were Grade 22 SPI-Glass vitreous carbon obtained from SPI, Inc. This hyperthermal beam was operated at a repetition rate of 2 Hz and was composed of 93% atomic and 7% molecular oxygen. The average translational energies of the atomic and molecular components of the beam were 4.99 and 9.98 eV, respectively, with energy widths (full width at half maximum) of 0.57 and 1.66 eV, respectively. Both atomic and molecular oxygen were in their ground electronic states: O(^{3}P) and $O_2(^3\Sigma_g^-)$ [86, 87]. A rotatable mass spectrometer was used to monitor both the incident molecular beam and the volatile species that scattered from the surface. The mass spectrometer was rotated within the plane defined by the surface normal and the beam, allowing for time-of-flight (TOF) distributions, which are number density as a function of time, $N(t)$, to be obtained for a variety of final angles, θ_f, with a given angle of incidence, θ_i. Using the known distance from

the interaction region on the surface to the electron-impact ionizer of the detector and the simple relationship between number density and flux, $P(E) \propto t^2 N(t)$, translational energy distributions, $P(E)$, were derived from the TOF distributions of the scattered products. Because these translational energy distributions are proportional to scattered flux, they were integrated to yield total relative flux for products (of a particular mass) that were scattered into the detector at a given final angle. Experiments were performed at various surface temperatures for vitreous carbon (VC) samples. O and O_2 were observed to scatter through non-reactive processes, whereas CO and CO_2 were the dominant reactive products.

Figure 4.1 shows representative TOF distributions for O, O_2, CO, and CO_2 that scattered from a vitreous carbon surface held at 800 K following impingement of the hyperthermal O/O_2 at $\theta_i = 45°$. Total values, non-thermal scattering (IS for O and O_2), and thermal desorption (TD) are represented by yellow, blue, and red colors, respectively. Time zero in the TOF distributions corresponds to the nominal time at which the incident gas pulse strikes the surface. Scattering of volatile species from the surface is considered in terms of two limiting cases, non-thermal scattering (impulsive scattering, IS, in the case of energy transfer without reaction) and thermal desorption (TD). Each TOF distribution is assumed to be composed of a component that can be described by a Maxwell-Boltzmann (MB) distribution, characterized by the surface temperature (in this case 800 K) and a non-thermal component with an unknown functional form. In practice, a MB distribution at the relevant temperature is scaled such that it describes the slow (thermal) portion of the TOF distribution as well as possible, and then the non-thermal component is found by subtracting the MB component from the overall TOF distribution.

The incoming atoms have high incident energies with a narrow energy spread, so the TOF distributions for the non-thermal products (blue curves in Fig. 4.1) tend to be narrow, especially for more grazing collisions where energy transfers are small. The thermal products (red curves in Fig. 4.1) have longer arrival times and relatively broad TOF distributions. The TOF data in Fig. 4.1 show that impulsive (non-thermal) scattering dominates the inelastic scattering of O and O_2 but that thermal processes dominate the reactive scattering of CO and CO_2. The product angular distributions, presented in Fig. 4.2, show the quantitative relationship between the thermal (red) and non-thermal (blue) scattered flux for each product.

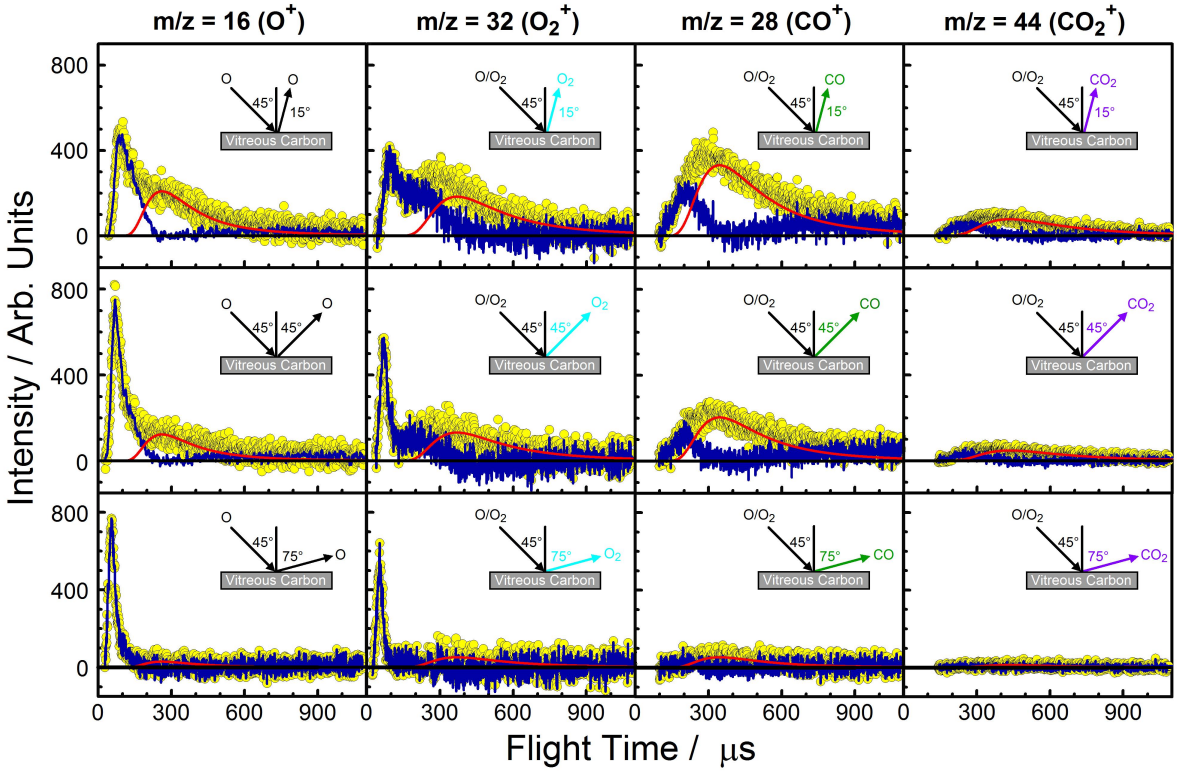

Figure 4.1: Representative time-of-flight (TOF) distributions.

As implied by the TOF distributions, the majority of the CO and CO_2 products exit the surface in thermal equilibrium. The angular distributions of these products also suggest the possibility that even a larger fraction of the CO and CO_2 products are produced through thermal mechanisms, because the non-thermal products (blue) also scatter mainly toward the surface normal. The scattering of reactive products toward the surface normal with non-thermal translational energies would be consistent with thermal desorption over a barrier [88]. Thus, it is possible that essentially all the CO and CO_2 molecules are produced through reactions that occur in thermal equilibrium with the surface.

The predominantly thermal reaction products indicate that the majority of the carbon oxidation reactions are not dependent on the incident beam energy and angle. Given the preponderance of thermal reaction processes at the surface, the beam is treated as a

supply of oxygen atoms to the surface and assume that the scattered product distributions measured in the molecular beam experiments can be applied directly to thermal gas conditions with high surface oxygen coverage. The surface oxygen coverage on vitreous carbon in the molecular beam experiments is probably high, as indicated by the broad angular distributions of the IS components of both O and O_2. It has been shown in literature [89] that a high surface adsorbate coverage broadens the angular distribution and shifts its peak to lower final angles, similar to what is observed in the angular distributions for O and O_2 in Fig. 4.2. It is not surprising that the data would suggest a high coverage, because the experiments were conducted under steady-state conditions that had been achieved following surface bombardment of more than 10,000 monolayers of O atoms. The flux of atomic and molecular oxygen to the surface within a typical hypersonic boundary layer is expected to be orders of magnitude higher than the time-averaged flux provided by the molecular beam. However, as the surface coverage is high in the molecular beam experiment, the results should be directly applicable to the high surface-coverage conditions expected under hypersonic conditions.

The experimentally measured scattering distributions represent a free molecular flux of reactants to a carbon surface that is flat at the micron scale but contains atomic-level roughness and complexity. Furthermore, the free flux of scattered products is directly measured. This is precisely the information required to formulate a boundary condition in a DSMC simulation where the microstructure of the TPS is resolved. Here, the measurements from the VC sample are used to provide boundary conditions for DSMC at a single surface temperature of 800 K. Future work will include molecular beam data for other material samples, and over a wide range of surface temperatures and surface coverage conditions, in order to create even more realistic boundary conditions.

4.2 Surface Reaction Probabilities and Microstructure

4.2.1 Surface reaction probabilities

The scattered species fluxes (denoted as N_s for species s), can be equated to the incoming beam flux as follows:

$$N_{O_{beam}} + 2N_{O_{2beam}} = N_O + 2N_{O_2} + N_{CO} + 2N_{CO_2} + N_{O_{desorb}} - N_{O_{adsorb}} \tag{4.1}$$

An important aspect of the reactive scattering measurements is that they are accumulated over long time scales under steady-state surface conditions. Given such steady-state conditions at a relatively low temperature (800 K), it can be assumed that there is no no net adsorption or desorption ($N_{O_{desorb}} = N_{O_{adsorb}}$). In addition, based on the experimental evidence of a low probability for the direct (Eley-Rideal) reaction of an incident O atom with a surface-adsorbed O atom to produce O_2 [24], it is assumed that all of the scattered O_2 comes from the O_2 component in the hyperthermal beam ($N_{O_{2beam}} = N_{O_2}$). With these assumptions, the fluxes of scattered products can be related to the incoming beam flux of atomic oxygen as:

$$N_{O_{beam}} \approx N_O + N_{CO} + 2N_{CO_2} \tag{4.2}$$

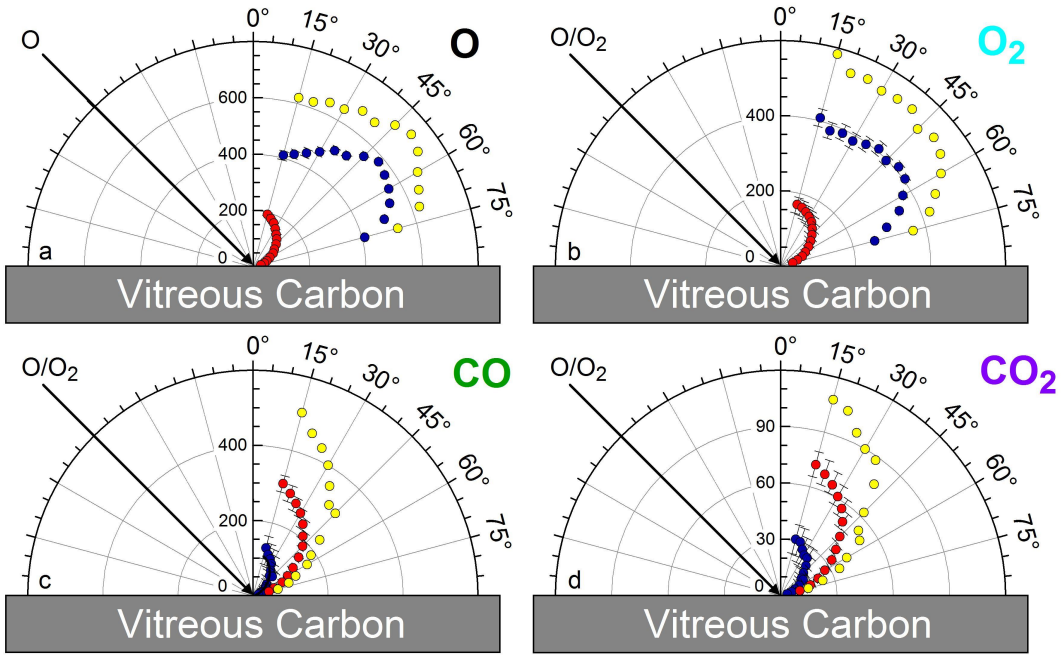

Figure 4.2: Flux-integrated angular distributions.

Although the majority of CO and CO_2 products scatter thermally, there is a non-negligible fraction of impulsively scattered O atoms (Fig. 4.2), which is presumably not involved in a surface reaction. It is not clear whether the incident O-atom flux that leads to this IS component would remain unreactive if the incident O-atom energy were

reduced significantly (thermal gas conditions) or whether this flux would be available for surface reactions to produce CO and CO_2. Thus, two limiting cases are considered. Case I assumes that the IS N_O component remains unchanged under thermal gas conditions (lower O-atom incident energy), that is, a significant fraction of the incoming N_O is scattered without reacting with the surface. Case II assumes that the measured IS N_O component in the beam experiments would undergo reactive scattering if the N_O atoms in this component had thermal energies. Specifically, in Case II it is assumed that the IS N_O component that is observed undergoes nonreactive and reactive scattering with the same proportions as the thermally scattered N_O , N_{CO}, and N_{CO_2} components seen in Fig. 4.2.

The numbers for N_O, N_{CO}, and N_{CO_2} were obtained by fitting a function to the angular distribution (Fig. 4.2) and integrating over all final angles. Under steady-state oxygen coverage, the summation of all the products is equal to the total number of incoming O atoms ($N_{O_{beam}}$) as seen in Eqn. 4.2. The ratios of the fluxes of scattered O, CO, and CO_2 to the incoming flux of O atoms ($N_{O_{beam}}$) can thus be calculated to give reaction probabilities for the scattered species. Incoming O atoms can participate in the reactive/scattering events listed in Table 4.1 with associated probabilities corresponding to the two limiting cases. (s) indicates surface atom, Exp indicates values from experiment and i represents O, CO or CO_2.

Table 4.1: Gas-surface events occurring in the simulations along with the associated probabilities for Case I and II.

Event	$P_{Exp\text{-}i} = N_i/N_{O_{beam}}$	
	Case I	Case II
C(s) + O → C(s) + O	0.743	0.431
C(s) + O → CO	0.193	0.421
C(s) + O + O → CO_2	0.032	0.074

The event, or reaction, probabilities obtained in Table 4.1 are used as input to surface boundary conditions in DSMC, and the velocities of scattered products are sampled from thermal distributions (accommodated to the surface temperature). It is noted that the reaction probabilities for CO formation are high (well above 0.1). Previous work performed by Poovathingal and Schwartzentruber [90] and by Driver *et*

al. [80] showed that when reaction probabilities are high, species concentrations in the near-surface region may not be sensitive to the precise values of the probabilities, as the gas-surface interaction tends to be diffusion limited. It was verified that DSMC results using Case I probabilities were very similar to results using probabilities from Case II. Thus, all simulations presented in this study correspond to the probabilities from Case II.

4.2.2 Microstructure of Carbon-Carbon (C-C) composite

Carbon-carbon (C-C) composites are composed of carbon fibers in a carbon matrix; thus, the reactivity of the fiber and the matrix are similar but the matrix has lower density and ablates faster compared to the fiber [10]. After ablation of the composite, the fibers protrude into the flowfield, which exposes a complex surface microstructure to gaseous species in the near-wall boundary layer, shown in Fig. 4.3 (right figure).

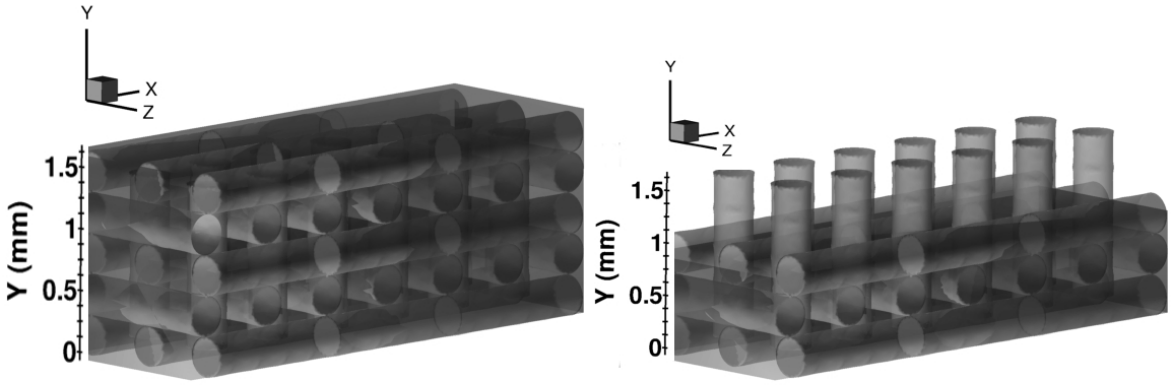

Figure 4.3: Schematic of the microstructure of a 3D C-C composite before and after ablation.

The morphology and surface area of the microstructure that is exposed into the flowfield will affect the magnitude of ablation under different regimes. The fibers in C-C composites can be continuous or short and can range from the isotropic variety that have low elastic moduli and modest strengths to highly oriented, high-performance

fibers. The carbon fibers are generally 7-10 μm in diameter and are derived from polyacrylonitrile (PAN) resin, petroleum pitch, or rayon [91]. C-C composites are classified as unidirectional, bidirectional, three-directional, and multidirectional based on fiber orientations and through thickness fiber alignments [75]. Thornel is a class of three-directional (3D) composites that is primarily used in the nose of reentry vehicles or hypersonic bodies [92]. The fibers in Thornel are aligned along the three orthogonal directions, and several different types of Thornel composites are available based on fiber diameter and spacing. Several fibers are tightly packed together to form a cylindrical yarn, which comprises 1,000-12,000 fibers. The diameter of a typical yarn would be on the order of 1 mm. Currently, the microstructure of Thornel is considered, which has a fiber diameter of 6.5 μm and a yarn consisting of 3,000 fibers with a cross-section of 0.1 mm^2. Therefore, the microstructure is modeled as cylinders in a carbon matrix orthogonal to the three Cartesian coordinates with a diameter of 0.34 mm (Fig. 4.3). The differential density between the fibers and the matrix exposes the fibers into the flowfield. Surface recession of 0.5 mm of the fibers due to ablation would result in 0.8 mm of recession in the matrix. Thus, the microstructure consists of fibers protruding at a height of 0.3 mm into the flowfield.

It is now possible to characterize the exact microstructure of an ablator sample. The dimensions and surface gridding methodology of a real sample are discussed later in Section 4.4. The reconstructed image of a 2D C-C composite is shown in Fig. 4.19. This *real* ablator sample is compared to the artificial microstructure (Fig. 4.3) in Table 4.2. It can be observed that the dimensions of the artificial microstructure closely resembles the microstructure dimensions of a real ablator sample.

Table 4.2: Comparison of dimensions between the microstructure of a *real* ablator sample obtained through tomography and the artificial microstructure used in the simulations.

Dimensions (in mm)	Real	Artificial
Width of the fiber	0.23	0.34
Height of the fiber	0.18	0.3
Distance between the fibers	0.13	0.34

4.2.3 DSMC simulation details

For a wide range of hypersonic conditions and corresponding boundary layer conditions, TPS microstructure dimensions are on the order of the local mean free path in the vicinity of the surface. For this reason, the DSMC method is an appropriate simulation technique, since it is accurate for flows ranging from continuum to free-molecular. Additionally, the DSMC particle method naturally handles complex surface geometry even in the presence of sharp flow gradients. DSMC simulations are therefore able to bridge the gap from the microstructure level to the boundary layer, and the results can be used to determine effective gas-surface models for use in CFD calculations of full vehicle flow-fields.

Gas-surface Reactions

In the simulations, 3 reactions in Table 4.1 to occur. When an O atom strikes the surface, there are three possible events with their respective probabilities. When a flux of O atoms strike, 43.11% of it scatters, 42.2% converts to CO and the remaining 7% is used up for CO_2 formation. Thus, for a single collision event, O scatters with a probability of 0.4311 and forms CO with a probability of 0.422. CO_2 formation requires removal of 2 O atoms. This is achieved by converting a single O atom that strikes the surface to CO_2 with a probability of 0.07/2 and deleting it with the same probability (0.07/2), thereby, effectively removing 2 O atoms to form a single CO_2 molecule. Four events can occur when an O atom collides with the surface. The gas-surface model must ensure that only one of the four events occurs and it must also reproduce the probabilities when the respective species fluxes are compared. To this purpose, the sequential probability selection procedure for gas-phase reactions [93] is extended to gas-surface reactions. The probability for a given event is computed as follows:

$$\begin{aligned} \mathrm{A} = 1; \quad & \mathrm{P_O} = \mathrm{A} \times \mathrm{P_{Exp\text{-}O}} \\ \mathrm{B} = 1/(1-\mathrm{P_O}); \quad & \mathrm{P_{CO}} = \mathrm{B} \times \mathrm{P_{Exp\text{-}CO}} \\ \mathrm{C} = 1/(1-\mathrm{P_{CO}}); \quad & \mathrm{P_{CO_2}} = \mathrm{C} \times \mathrm{P_{Exp\text{-}CO_2}} \\ \mathrm{D} = 1/(1-\mathrm{P_{CO_2}}); \quad & \mathrm{P_{O\text{-}remove}} = \mathrm{D} \times \mathrm{P_{Exp\text{-}O\text{-}remove}} \ . \end{aligned}$$

where $\mathrm{P_{Exp\text{-}O}}$ is the probability of O scatter, $\mathrm{P_{Exp\text{-}CO}}$ is the probability of CO formation, $\mathrm{P_{Exp\text{-}CO_2}}$ is the probability of CO_2 formation, and $\mathrm{P_{Exp\text{-}O\text{-}remove}}$ is the probability of

removing an O atom from the system and $P_{\text{Exp-}CO_2} = P_{\text{Exp-O-remove}}$.

Only one event is allowed to occur for a given collision of the O atom with the surface. The pseudo code for the process is as follows

repeat
  A = 1; P = AP_{expt-O}
  if random number < P **then**
    reaction occurs
  end if
  if no reaction **then**
    B = 1.0/(1.0-P); P = B$P_{expt-CO}$
    if random number < P **then**
      reaction occurs
    end if
  end if
  if no reaction **then**
    C = 1.0/(1.0-P); P = C$P_{expt-CO_2}$
    if random number < P **then**
      reaction occurs
    end if
  end if
until reaction occurs

The condition for this method to work is $P_{expt-O} + P_{expt-CO} + P_{expt-CO_2} \leq 1.0$ which will always hold true. The order in which the events are tested does not affect the results and this method can be extended for any incoming species and any number of products. Species concentrations were compared for several different timesteps over several simulations and it was noted that the probabilities were being reproduced.

Gas phase chemistry

A molecule formed due to surface oxidation (like CO, CO_2) could react within the microstructure in the gas phase and a different molecular species would diffuse into the boundary layer. Gas phase reactions have to be modeled accurately to characterize this process. There are several DSMC models that handle gas phase chemistry but the

Total Collision Energy Model (TCE) [64] is most widely used for its simplicity and direct correlation to the Arrhenius rate equation. During the collision process of 2 particles, the net energy (sum of the center-of-mass collision energy and internal energies) of the 2 particles is compared to the activation energy. If the net energy is greater, the reaction probability is computed. If the probability of reaction is greater than a random number generated, the reaction is performed and the remaining energy is redistributed based on the Larsen-Borgnakke model. The probability of reaction in the TCE model is a function of the Arrhenius or modified Arrhenius rate parameters. The probability of reaction is the ratio of total cross-section (σ_T) to the reactive cross-section (σ_R) and is of the form

$$\frac{\sigma_R}{\sigma_T} = C_1(E_c - E_a)^{C_2}(1 - E_a/E_c)^{\zeta+1.5-\omega}$$

where C_1, C_2 are constants, E_c is the total collision energy, E_a is the activation energy, ζ is the degrees of freedom participating in the reaction and ω is the collision cross-section. C_1 and C_2 are constants that have to be determined. The reaction rate from kinetic theory is obtained as

$$k(T) = \frac{2C_1\sigma_{ref}}{\pi^{0.5}\epsilon}(\frac{2kT_{ref}}{m_r})^{1/2}\frac{\Gamma(\zeta + 5/2 + C_2 - \omega)}{\Gamma(\zeta + 5/2 - \omega)}\frac{k^{C_2}T^{C_2+1-\omega}}{T_{ref}^{1-\omega}}exp(-\frac{E_a}{kT})$$

where σ_{ref} is the reference cross-section, ϵ is the symmetry factor, T_{ref} is the reference temperature, T is the temperature and m_r is the reduced mass. The expression above can be compared to the modified Arrhenius equation $k(T) = AT^{\eta}exp(-\frac{E_a}{T})$ to obtain the unknown constants C_1 and C_2. After determining the unknown constants, the reaction probability now is

$$(\frac{\sigma_R}{\sigma_T})_{forward} = \frac{\pi^{1/2}\epsilon AT_{ref}^{\eta}}{2\sigma_{ref}(kT_{ref})^{\eta-1+\omega}}\frac{\Gamma(\zeta + 5/2 - \omega)}{\Gamma(\zeta + \eta + 3/2)}(\frac{m_r}{2kT_{ref}})^{1/2}\frac{(E_c - E_a)^{\eta+\zeta+1/2}}{E_c^{\zeta+3/2-\omega}}$$

The backward reaction rates are obtained through the partition functions $K_{eq} = \frac{k_f}{k_r} = \frac{Q^{P_1}Q^{P_2}}{Q^{R_1}Q^{R_2}}exp(-\frac{E_a}{kT})$ where Q is the total partition function of a given molecule and P_1, P_2, R_1, R_2 represent the products and reactants respectively. Through a similar analysis, the reaction probability for backward rate can be obtained as

$$(\frac{\sigma_R}{\sigma_T})_{backward} = \frac{AT^{\eta}}{(2/\epsilon)\pi^{-1/2}\sigma_{ref}(T/T_{ref})^{1-\omega}(2kT_{ref}/m_r)^{1/2}}\frac{Q^{R_1}Q^{R_2}}{Q^{P_1}Q^{P_2}}$$

A detailed description of the TCE model (forward and backward) is given in Ref. [64]. The advantage of the TCE model is that the probability of reaction depends only on Arrhenius rate parameters and other numerically dependent parameters are not required. Therefore, several species and reaction lists can be added to the solver without any difficulty. In order to validate the implementation of the TCE model and post reaction redistribution of energies, two different tests were performed.

In the first test, the rate of reaction obtained from the DSMC simulations was compared to the Arrhenius rate equations with published rate parameters obtained experimentally. A detailed list of all the rates is given in the work of Park *et al.* [94]. A box was initialized at a given temperature only with the reacting gas species. Collision pairs were then selected and tested for reaction. If a reaction occurred, a counter was increased. The post collision energy redistribution and species changes were not done. This was repeated for several randomly selected pairs over several timesteps. The reaction probability was then computed as $\frac{\text{number of reactions}}{\text{number of collisions}}$. This probability was then converted into a rate that can be directly compared to the input Arrhenius rate [95].

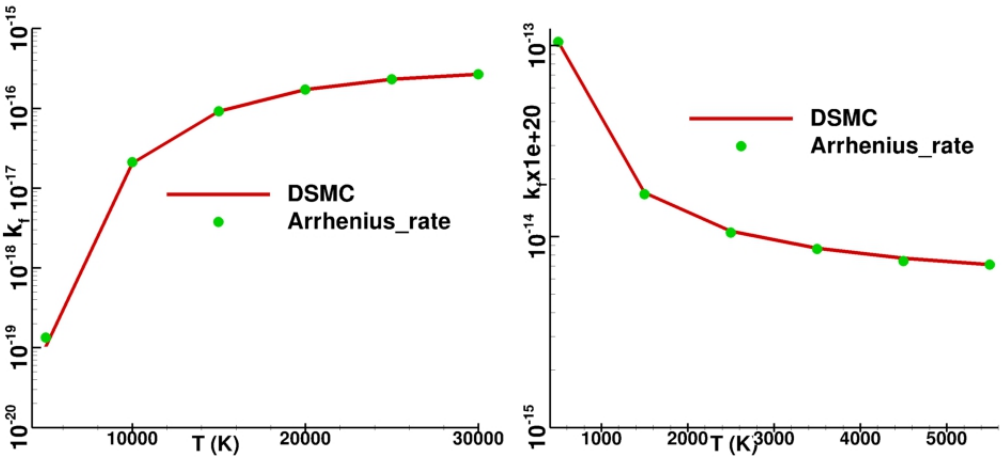

Figure 4.4: Comparison of rates obtained from DSMC and Arrhenius rates for dissociation (left figure) and recombination (right figure).

Figure 4.4 show the comparison of rates obtained from DSMC simulations and the Arrhenius rates obtained experimentally for both dissociation and recombination of CO_2. In the second test, a box of all species involved in the reaction was initialized in chemical non-equilibrium and the box was allowed to relax to equilibrium. Figure 4.5

shows a box relaxing to equilibrium for the reactions, $CO_2 + CO_2 \longleftrightarrow CO + O + CO_2$ and $CO_2 + O \longleftrightarrow CO + O_2$ respectively. It will be seen later that the reaction $CO + O_2 \longrightarrow CO_2 + O$ inside the microstructure is critical in the concentration of products that diffuse into the boundary layer.

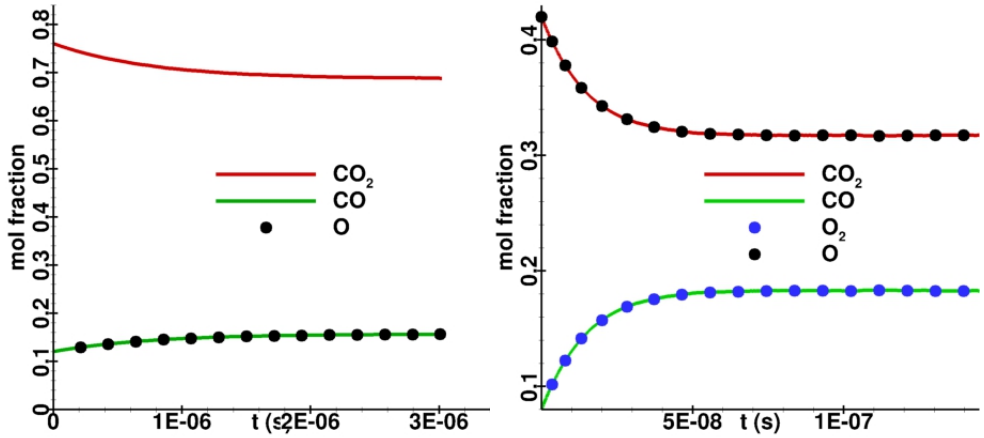

Figure 4.5: Isothermal heat bath relaxing to chemical equilibrium. The left figure is for dissociation-recombination and the right figure is for exchange reaction.

Selection Procedure for Linear Polyatomic Molecules in DSMC

One of the products of oxidation on the carbon surface is CO_2 which is a linear triatomic molecule. It has 2 rotational degrees of freedom and 4 vibrational modes. The vibrational modes are symmetric stretching (Θ_v = 1890 K), asymmetric stretching (Θ_v = 3360 K) and two bending modes (Θ_v = 954 K) which are degenerate. Several models have been proposed in DSMC for the energy exchange between the translational and the internal energy modes. In these models, a probability P_i is computed for every colliding particle and selection rules are applied to determine the modes that exchange energy. Haas *et al.* [96] proposed the particle selection prohibiting double relaxation selection rule and modifications were proposed by Gimelshein *et al.* [97] and Zhang and Schwartzentruber [93]. It is demonstrated here that this modified rule can be extended for polyatomic molecules. Vibrational relaxation is modeled in continuum solvers by the Landau-Teller equation which has the form $\frac{dE(t)}{dt} = \frac{E^*(t)-E(t)}{\tau}$, where E(t) is the instantaneous energy of the mode, $E^*(t)$ is the equilibrium energy and τ is the relaxation time constant of the mode. The equilibrium vibrational energy (E^*) is computed from

the translational temperature (T_t), $E = \frac{\zeta}{2} k_b T_t$, where k_b is the Boltzmann constant and ζ is the number of vibrational degrees of freedom which for a harmonic oscillator is given by $\zeta = \frac{2\theta_v/T}{exp(\theta_v/T)-1}$.

The time constant, τ is calculated from the expression $P\tau = exp(40.58T^{-\frac{1}{3}} - 17.50)$ [98], where P is the pressure in atm. τ can be expressed as as $\tau_c Z_v$ where τ_c is the mean collision time and Z_v is the vibrational collision number used to compute the probability P_i for a colliding pair. The probability of vibrational-translational energy exchange in DSMC is given by $\frac{\Gamma_i+\zeta_t}{\zeta_t}\frac{1}{Z_v}$, where ζ_t is the translational degree of freedom and $\Gamma_i = \xi_v(T)^2 exp(\Theta_v/T)/2$ and $\xi_v(T) = \frac{2\Theta_v/T}{exp(\Theta_v/T)-1}$. Thus, for a given Z_v, the different vibrational modes will relax to equilibrium at different rates.

Isothermal heat bath calculations were performed in DSMC for CO_2-CO_2 collisions and the relaxation rates were compared with the analytical expression. Fig. 4.6 compares the temperature profiles of all the four internal modes. Fig. 4.7 compares the temperature of each internal mode with the corresponding Landau-Teller solution. At low initial temperatures, the internal modes relax at different rates but at higher initial temperatures all the internal vibrational modes relax at the same rate because all the vibrational modes are equally populated.

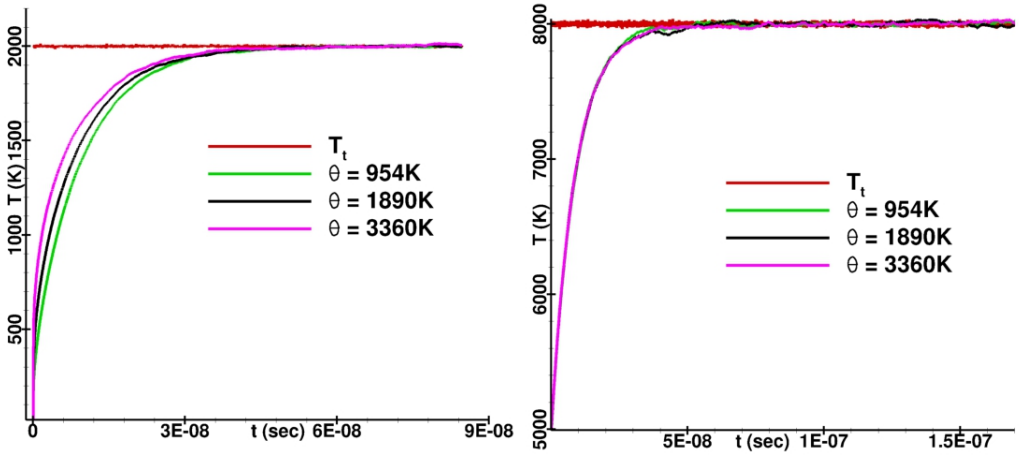

Figure 4.6: Comparison of all vibrational modes at different initial temperatures.

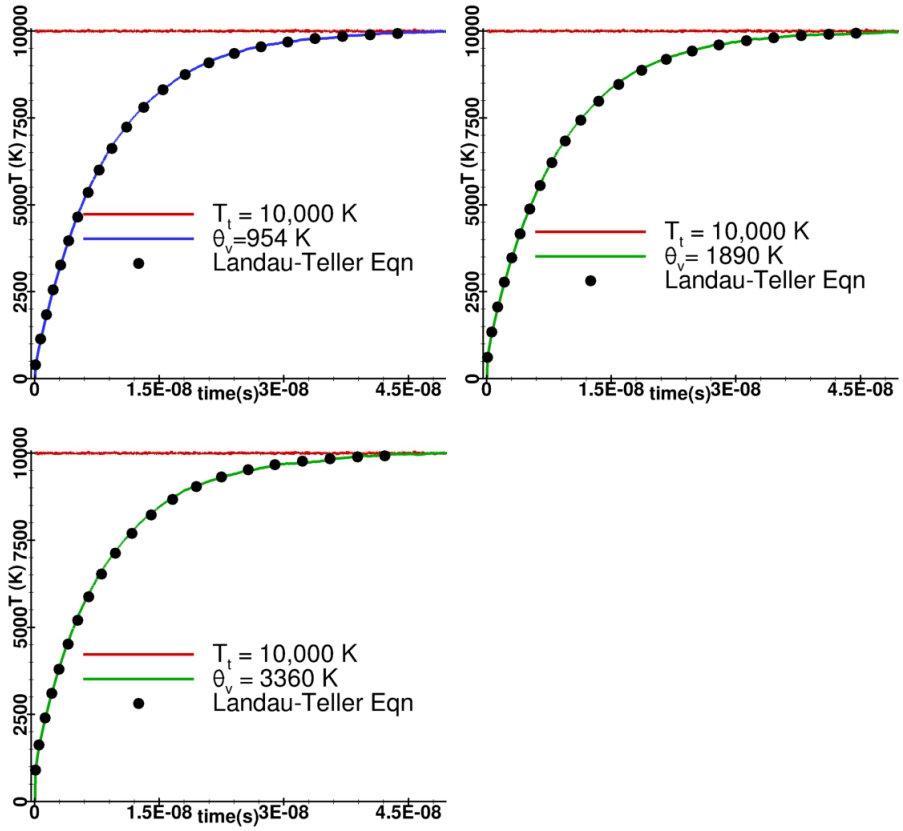

Figure 4.7: Comparison of vibrational relaxation of each mode with analytical expression from Landau Teller equation.

The surface mesh of a TPS sample is extremely complicated, and therefore a parallel and computationally efficient solver is required to simulate the flow over such a geometry. The parallel Molecular Gas Dynamics Simulator (MGDS) [76] code developed at the University of Minnesota is used which has a multi-level Cartesian grid [77] for the flowfield and a robust cut-cell algorithm to handle complex surface geometries [78]. This efficient and robust DSMC implementation ensures that one can perform accurate, large scale, simulations on very complicated geometries.

4.3 Results and Discussion

4.3.1 Diffusion Simulation Setup

Diffusion simulations were performed on a small section of the microstructure. Specifically, fluxes of O atoms and O_2 molecules were specified at y_{max} (the height of the domain in y) and symmetric boundary conditions were applied in the x and z directions. The molecules and atoms at the inflow were given zero mean velocity but had thermal velocities corresponding to 800 K. Therefore, O and O_2 diffused into the domain and collided with the surface to produce CO and CO_2, which in-turn diffused back towards the inflow. Only atomic oxygen was reactive with the surface and all other species impacting the surface were scattered thermally. A schematic of such a diffusion simulation is shown in Fig. 4.8, where the inflow and surface boundary conditions lead to steady-state gradients in species concentrations.

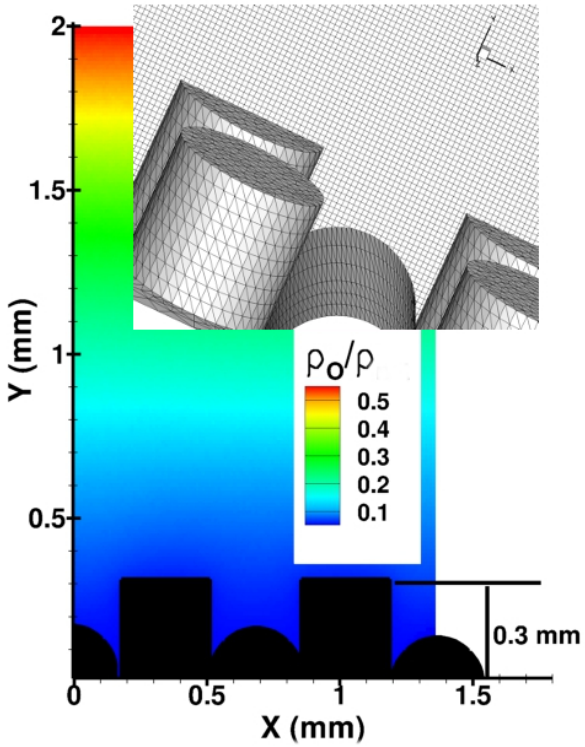

Figure 4.8: Schematic of the microstructure and domain simulated for $\rho = 4.7 \times 10^{-3}$ kg m^{-3}.

The contours are mass fraction of O atoms and the inset shows the intersection of Cartesian flow cells and surface triangles that determine the surface of the microstructure. This situation is analogous to a chemical boundary layer, where the bulk convection is absent and the thickness of the boundary layer is artificially imposed as y_{max}. As discussed in the next section, this chemical boundary layer thickness is similar to that when convection is included, and many of the resulting trends are the same. For all simulation results presented, the surface reaction probabilities corresponding to Case II (Table 4.1) is used, described in section 4.2.1.

4.3.2 Diffusion Results

The mass fraction profiles for the four species in the simulations are compared in Fig. 4.9 at a Knudsen number (Kn) of 0.04 for an inflow density of 4.7×10^{-3} kg m^{-3} and inflow mass fractions of 0.4 O_2 and 0.6 O. The figure on the left corresponds to the mass fractions of CO and CO_2 and right corresponds to the mass fractions of O and O_2. The dashed lines correspond to the simulations where no gas-phase reactions were allowed and the solid lines correspond to the simulations where gas-phase reactions were allowed only within the microstructure ($y < 0.3$ mm). This was done to isolate and study the importance of gas-phase reactions inside the microstructure. It can be clearly observed that the CO_2 mass fraction is much higher when gas-phase reactions were allowed indicating that gas-phase reactions are dominant inside the microstructure.

Gas-phase reactions occur over several mean free paths of the flow and thus, the effect of Knudsen number (Kn) was studied further. The Kn number is defined as Kn $= \lambda/\mathrm{L}$, where λ is the mean free path of the flow and L is a relevant length scale which is the height of the microstructure (0.3 mm) in the simulations. Figure 4.10 shows the ratio of product species mass fraction for the simulations with an inflow mass fraction of 0.4 O_2 and 0.6 O with gas-phase reactions and without gas-phase reactions as a function of Kn number.

The ratios are computed in the first cell above the microstructure which would correspond to the first cell in the boundary layer (the mass fractions are averaged along the x and z directions). It can be seen that as the Kn number is lowered (more continuum), gas-phase reactions occur within the microstructure. At a Kn number of 0.04, the CO_2 mass fraction is ~ 1.8 times higher when gas-phase reactions were allowed in the microstructure.

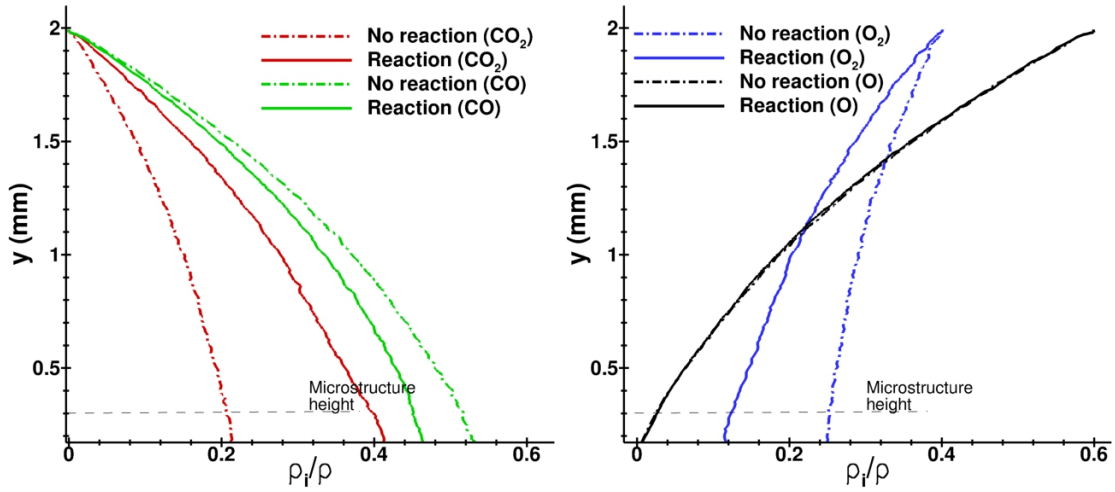

Figure 4.9: Mass fraction profiles for fiber with gas-phase reactions and without gas-phase reactions.

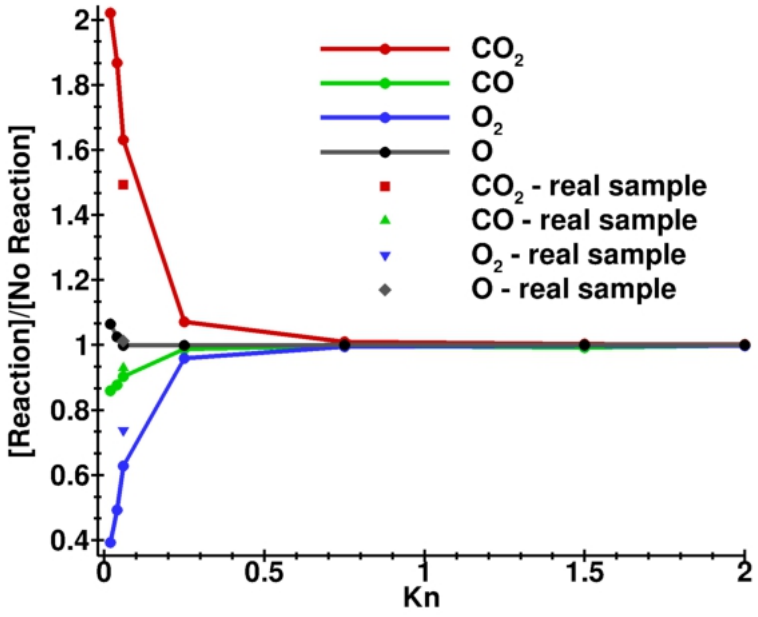

Figure 4.10: Mass fraction ratio obtained by varying the Kn number at fixed inflow O_2 mass fraction of 0.4.

The two reactions that produce CO_2 are the recombination reaction CO + O + M $\longleftrightarrow$ CO_2 + M and the backward exchange reaction CO + O_2 $\longleftrightarrow$ CO_2 + O. The total number of exchange reactions and recombination reactions occurring inside the microstructure are compared for three Kn numbers in Table 4.3 which shows that the dominant reaction of the two is the exchange reaction. The exchange reaction should result in the depletion of O_2 and CO.

Table 4.3: Ratio of the exchange and recombination gas-phase reactions that form CO_2 are tabulated at different Kn numbers to evaluate the dominant reaction.

Kn	$\frac{CO+O+M \rightarrow CO_2+M}{CO+O_2 \rightarrow CO_2+O}$
0.04	1.1089×10^{-3}
0.75	1.3726×10^{-4}
1.6	9.0335×10^{-5}

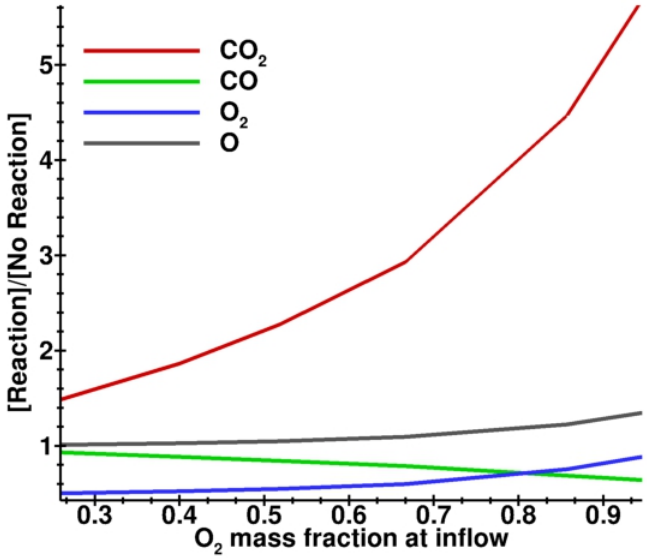

Figure 4.11: Mass fraction ratio obtained by varying the inflow O_2 mass fraction at fixed Kn number of 0.04.

The O_2 mass fraction ratio does decrease corresponding to the increase in the ratio of CO_2 mass fraction but there is very little change in the ratio of CO mass fraction.

This is because the exchange reaction also produces O atoms that further react with the surface to form CO. Therefore, the CO that was consumed in the exchange reaction is replenished by the gas-surface reaction C(s) + O $\rightarrow$ CO + (s).

The results indicate that CO_2 formation in the near-wall region is dependent on the amount of CO and O_2. This is further examined by varying the inflow mass fraction of O_2 at Kn= 0.04. Figure 4.11 shows the ratio of species mass fraction as a function of the inflow O_2 mass fraction. It can be observed from Fig. 4.11 that the ratio of CO_2 mass fraction increases as the O_2 mass fraction at the inflow increases. At low inflow mass fraction of O_2, formation of CO_2 is limited by the availability of O_2. However, as the O_2 mass fraction at the inflow is increased, it is seen that the ratio of O_2 in the boundary layer increases which implies that some O_2 does not react because the exchange reaction is now limited by the availability of CO. The gas-phase chemical reaction rates used in this study [94] indicate that the backward exchange reaction is dominant at 800 K. However, it is important to note that this reaction rate is evaluated assuming no energy barrier for the process [99]. In fact, there is experimental evidence [100] that this reaction has a significant energy barrier. Further analysis of this reaction is warranted; however, such analysis is beyond the scope of the current work.

The results above demonstrate that gas-phase reactions in the near-surface region may have a significant effect on the composition of species diffusing into the boundary layer from the microstructure. In particular, the simulations predict a coupled reaction mechanism where CO produced through a gas-surface reaction went on to react in the gas phase with O_2 to produce CO_2 and O atoms that could go on to participate in additional gas-surface reactions. This would result in higher mass loss from the surface of the microstructure due to the additional O atoms produced in the gas-phase within the microstructure. Figure 4.12 show the increase in mass loss from the surface (total carbon atoms removed) as a function of Kn number and inflow mass fraction of O_2 when gas-phase reactions are allowed. The percentage is computed as $\frac{\text{Mass loss}_{\text{reacting case}} - \text{Mass loss}_{\text{non reacting case}}}{\text{Mass loss}_{\text{reacting case}}} \times 100$. It can be observed that the mass loss increases with lower Kn number (continuum) and greater influx of O_2 which directly correlates to the increase in the number of exchange gas-phase reactions that produce CO_2 and O.

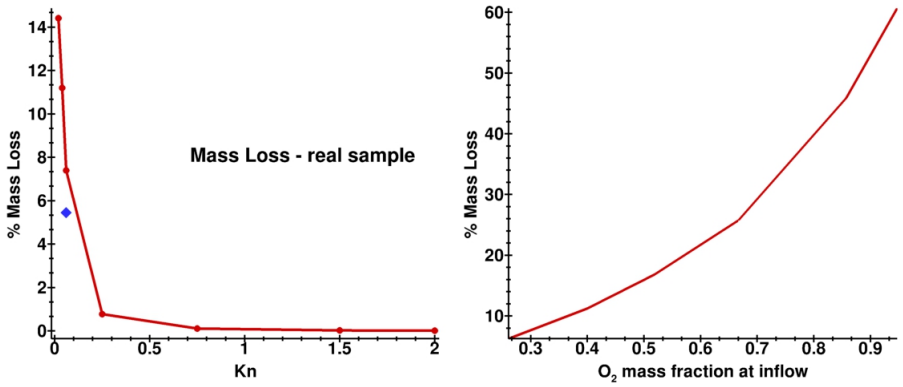

Figure 4.12: Percentage of mass loss is compared for the reacting and non reacting case.

4.3.3 Convection Simulation setup

The effect of mean flow is now examined. Initially, flow over a flat plate was simulated with freestream properties of $T = 750$ K, $\rho = 4.5 \times 10^{-3}$ kg m^{-3} and $U = 4030$ m s^{-1}. Gas-surface reactions were allowed to occur but no gas-phase reactions were allowed. A boundary layer profile was extracted downstream where the boundary layer thickness (δ_{99}) was ~ 10 times the height of the microstructure (0.3 mm). This extracted boundary layer (profiles shown in Fig. 4.13) was then imposed over the microstructure and four different cases were analyzed. The Kn number was kept constant at 0.04.

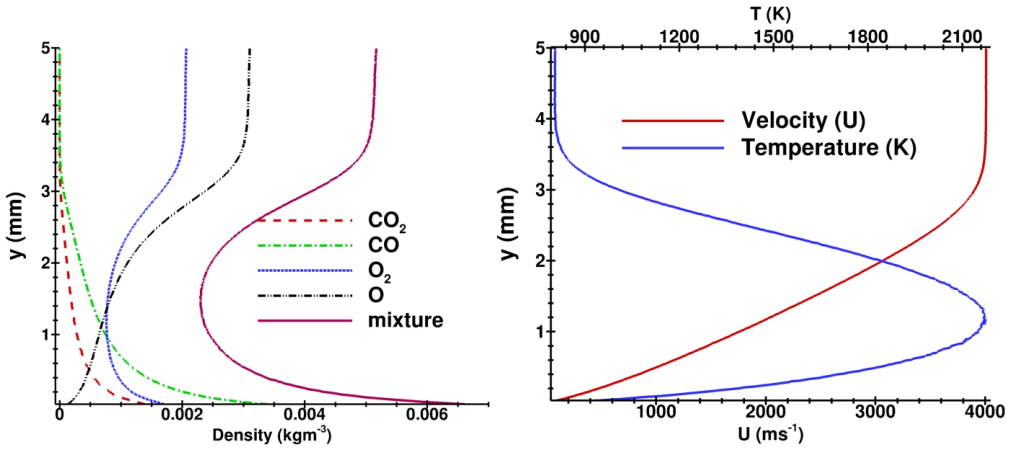

Figure 4.13: Imposed mean boundary layer profile.

4.3.4 Convection Results

Four different cases were simulated to study the interplay of mean convection and diffusion on gas-phase reactions. In the first case, gas-phase reactions were allowed only inside the microstructure (referred to as Case RI). In the second case, gas-phase reactions were allowed only outside the microstructure (referred to as Case RO). In the third case, gas-phase reactions were allowed everywhere (referred to as Case RE). Gas-phase reactions were not allowed in the fourth case (referred to as Case NR). Figure 4.14 shows the mean flow velocity contour for the case where reactions were allowed everywhere (Case RE). Two profiles were extracted along line 1 and line 2 as indicated in Fig. 4.14 and were compared for the four cases. The mean velocity and temperature is shown in Fig. 4.15. There is not much variation in either the mean velocity or mean temperature profiles between the four test cases.

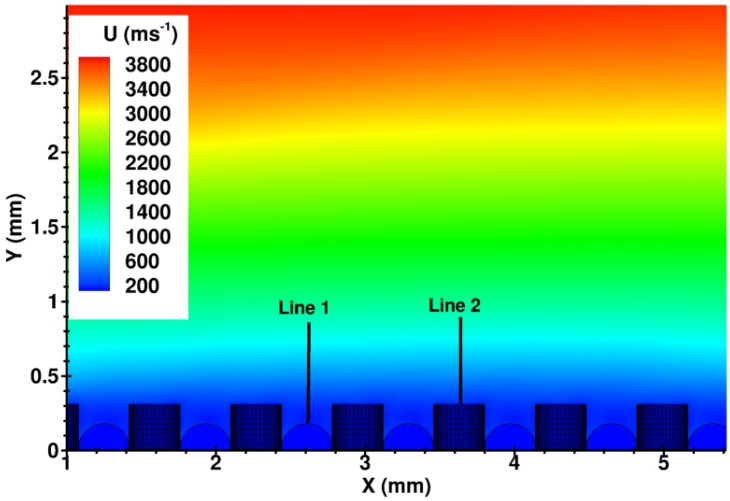

Figure 4.14: Contours of mean velocity in the x direction.

Differences can be observed when individual species mass fractions are compared (Fig. 4.16). Firstly, it is interesting to observe that Case RE has the highest CO_2 mass fraction inside the microstructure. The total number of gas-phase reactions occurring inside the microstructure to produce CO_2 for Case RI is 10% higher than Case RE. However, the mass fraction of CO_2 inside the microstructure is lower for Case RI. This is because the concentration gradient between the species in the boundary layer and the species inside the microstructure is higher for Case RI. Thus, more species diffuse out

into the boundary layer from inside the microstructure for Case RI. However, the gases convect downstream and the profile outside the microstructure for Case RI matches Case NR. The opposite effect is observed when gas-phase reactions are allowed only outside the microstructure (Case RO).

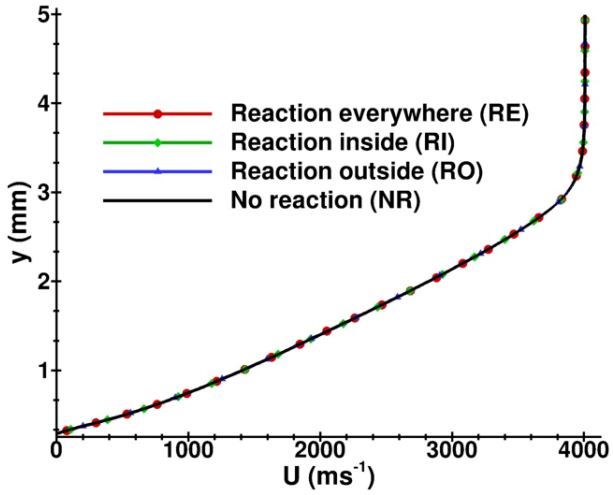

Figure 4.15: Mean velocity profile for all the four cases.

The total number of gas-phase reactions between Case RO and Case RE is also approximately same. The profiles between Cases RE and RO agree well outside the microstructure but not inside the microstructure. Moreover, if no diffusion were allowed into the microstructure, the profile inside the microstructure for Case RO would be close to the Case NR. However, the concentration gradient results in species diffusing inside the microstructure and the mass fraction is actually closer to the case where reactions are only allowed inside (Case RI). As expected, Case NR had the lowest mass fraction of CO_2. Similar results were observed for the profiles extracted along line 2. The profiles of a flat plate simulation where reactions are allowed everywhere are compared to the microstructure (Case RE) for CO and CO_2 and shown in Fig. 4.17. The flat plate profiles are shifted in height (y) depending on the height of the protruded microstructure. It can be observed that CO_2 mass fraction is higher for the microstructure compared to the plate close to the surface. This suggests that the reaction probabilities cannot be directly used in CFD or compared to macroscopic experiments without accounting for the microstructure of the material being studied.

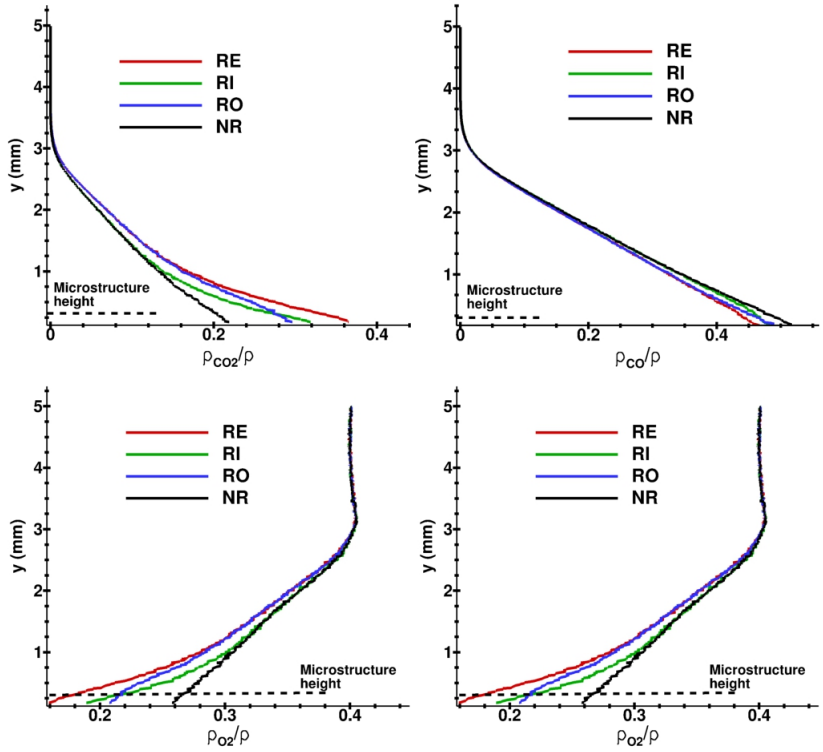

Figure 4.16: Mass fraction profiles extracted at line 1 for the four cases.

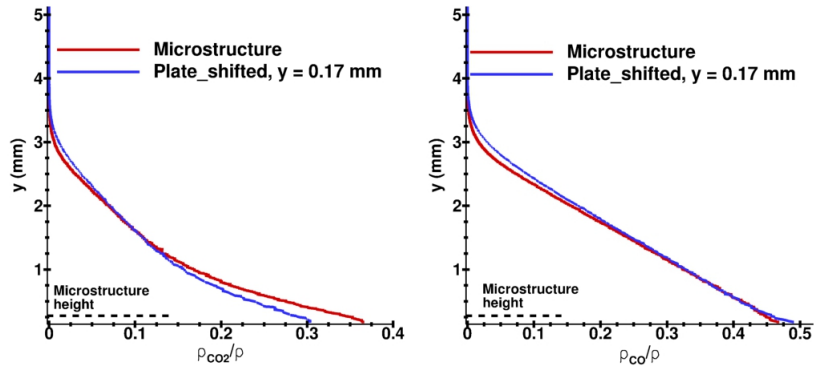

Figure 4.17: Mass fraction profiles comparing flat plate and microstructure simulations where gas-phase reactions are allowed everywhere.

Finally, the total mass losses (net number of carbon atoms removed) are compared in Fig. 4.18 which further shows the differences in the simulations. The percentage increase

or decrease in mass loss is compared to the case where reactions are allowed everywhere (Case RE). The flat plate has the least mass loss of all the four cases as a result of two factors: lower surface area and additional O atoms produced due to the gas-phase reactions in the microstructure that resulted in further gas-surface reactions (described earlier in Section 4.3.2). However, the mass loss for the case where reactions were allowed only inside (Case RI) and the case where reactions were allowed only outside (Case RO) is also lower than the case where reactions were allowed everywhere (Case RE). The surface areas in these three cases were the same and the differences arise only because of the backward exchange reaction. Thus, the inclusion of gas-phase reactions influences mass loss from the surface, which corroborates the observation in the previous section of a coupled mechanism that was also present in the diffusion simulations.

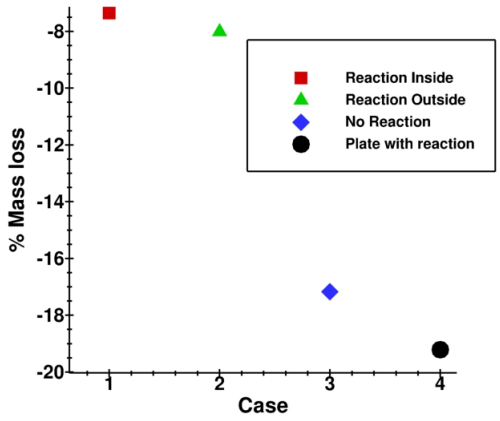

Figure 4.18: Percentage of mass loss is compared for all the convection cases with respect to Case RE.

These results thus suggest that modeling of gas-phase reactions inside the microstructure of an ablator sample may be important in determining not only the composition of the species that diffuse into the boundary layer but the total surface mass loss. It is important to emphasize that the current study is performed at a single temperature of 800 K and the results are specific to the gas-phase chemical reaction rates of Ref. [94].

4.4 Microtomographic reconstruction of a *real* ablator

The advantage of DSMC is that it can resolve flows at micro scales and the cut-cell algorithm in the MGDS solver can handle very complex geometries. Thus, it is possible to simulate flows over the cracks, crevices, and protruding granules of a real ablator sample. This is achieved through 3D reconstruction of a sample using X-ray tomography. Such simulations have been done previously for porous ablators, specifically carbon fiber preform [101] but the microstructure of non-porous carbon ablators (2D C-C, 3D C-C) has not been examined. A 2D C-C sample was provided by the Corral Laboratory at University of Arizona and is shown in the red inset of Fig. 4.19.

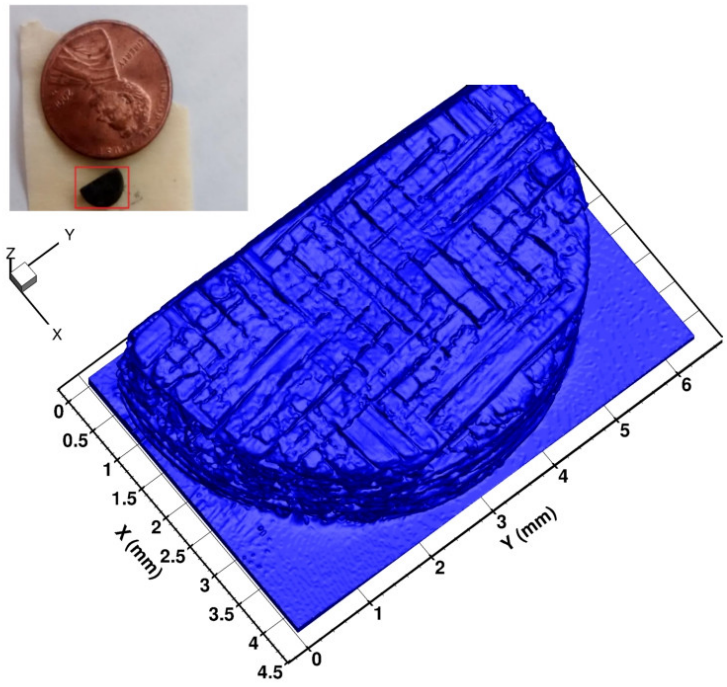

Figure 4.19: 3D reconstruction of a "real" TPS sample (2D C-C composite) obtained from tomography.

The diameter of the sample is 4 mm and the unablated height is 2 mm. The sample was ablated for 15 min at 1600°C and an O_2 partial pressure of 0.29 kPa. The sample was scanned in an X-ray facility at University of Minnesota and 3-D reconstructed using tomographic techniques. The resolution of the reconstruction was 5.4 μm. The

reconstructed surface can now be used to measure the dimensions and also triangulated as shown in Fig. 4.20. The analysis and surface triangulation was done using the commercial software Avizo.

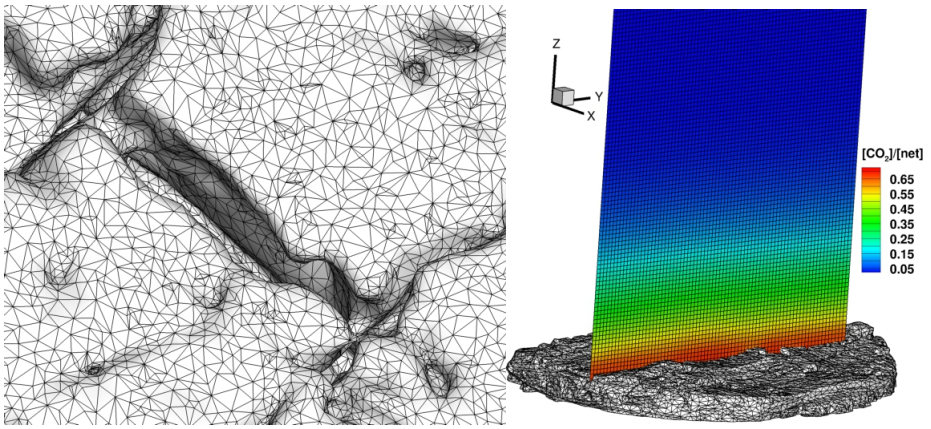

Figure 4.20: The grid on the surface of a *real* ablator sample and DSMC simulations of the flow over a *real* ablator sample.

A section of the non porous heat shield was isolated and triangulated. The surface grid (triangles) shown in Fig. 4.20 was used in the DSMC solver MGDS to simulate the flow over the microstructure. The cracks/crevices between the fiber bundles can be clearly seen. Similar to the previous sections, gas molecules will diffuse into the microstructure and react inside the microstructure affecting the species composition outside the surface. Initially, two grid resolutions of 100,000 triangles and 5,000,000 triangles were generated and diffusion type simulations like those presented in Section 4.3.2 were performed over the real microstructure. The mass fractions at the inflow for O_2 and O were 0.4 and 0.6, respectively. The Kn number of the flow was 0.06 with a characteristic length of 0.6 mm. Gas-phase reactions were allowed to occur only within the characteristic length of the microstructure. The CO_2 mass fraction contour from the reacting case is shown in Fig. 4.20. The total mass loss, total number of gas-phase reactions, and the individual mass fractions at the first cell above the microstructure were compared for 100,000 triangles and 5,000,000 triangles and the difference was less than 1%. Further simulations were done using the surface grid of 100,000 triangles.

Diffusion simulations with and without gas-phase reactions were performed and the results were compared to the simulated microstructure (microstructure generated in the

previous sections). The mass fraction ratios and mass loss are shown as symbols in Figs. 4.10 and 4.12. It is interesting to note that the mass loss and the species compositions between the ideal microstructure and the real microstructure are comparable. The real microstructure used in this study is weakly ablated and it is not clear what the microstructure would look like for a strongly ablated sample. In future, the study over the real microstructure will be extended to a variety of different carbon samples at different stages of ablation.

4.5 Conclusions

Molecular simulations were performed of high temperature dissociated oxygen reacting with a carbon-carbon composite material, where the microstructure was resolved. The DSMC method was used to simulate the convection and diffusion of reactants towards the microstructure and the transport of surface reaction products away from the microstructure. Simulations were performed with and without gas-phase chemical reactions in order to determine the relative importance of gas-surface reactions compared to gas-phase reactions next to the material surface. The simulations incorporate reaction probabilities for individual gas-surface collisions based on new reactive scattering data obtained in a molecular beam facility. The molecular beam experiments clearly indicate that a majority of surface reaction products accommodate to the surface and are scattered thermally. The experiments provide detailed data on the relative magnitudes of O, O_2, CO, and CO_2 scattering from a representative material sample, made of vitreous carbon. For a gas-surface temperature of 800 K, it was found that despite CO being the dominant surface reaction product, a gas-phase exchange reaction forms significant CO_2 within the microstructure region. The amount of CO_2 production within the microstructure region was shown to be dependent on the local Knudsen number, based on the exposed microstructure height. It is important to emphasize again that these results are specific to 800 K and are specific to the gas-phase chemical reaction rates of Ref. [94]. Consistent results were obtained using a real ablated sample where a complex surface mesh was constructed using X-Ray Computed Tomography to render a 3D image and triangulate the TPS surface.

The results of this study demonstrate a methodology (and required assumptions) to

incorporate gas-surface measurements from molecular beam facilities into DSMC simulations where material microstructure is resolved. This approach enables the influence of gas-surface reactions, gas-phase reactions, and material microstructure to be analyzed separately. At the same time, this approach is able to simulate the net effects on the full boundary layer and therefore aid in the development of improved boundary conditions for CFD simulations. This study was restricted to a single material temperature of 800 K, where a complete experimental data set was available and, most importantly, for which the surface coverage condition was well-characterized in the experiments. The next chapter will use experimental data [24] over a range of higher surface temperatures where changes in surface coverage during the experiment must be understood and properly accounted for when using the data in simulations of thermal-gas conditions (i.e. boundary layer simulations).

Chapter 5

Finite Rate Model

The previous chapter discussed the molecular beam results in detail. Here, the molecular beam data [24], taken over a wide range of surface temperatures is used to construct a temperature-dependent oxidation model that can be implemented in CFD and material response codes. The new model provides reaction mechanisms and rate parameters and is implemented into the UnStructured 3-Dimensional (US3D) CFD code with demonstrative calculations presented later in this chapter. The experimental details are repeated here again for clarity.

5.1 Molecular Beam Experiments

The experiments were performed with the use of a crossed molecular beam apparatus [82, 83] that was configured for beam-surface scattering [24, 84]. A molecular beam containing 93% hyperthermal O atoms and 7% O_2 molecules, both in their ground electronic states, $O(^3P)$ [86] and $O_2(^3\Sigma_g^-)$ [102], with a nominal velocity of 7756 ms^{-1} and corresponding translational energies of 4.99 eV and 9.98 eV, respectively, was produced using the laser detonation source described in Refs. [24, 83] and [84]. The molecular beam was directed at the surface of resistively heated grade 22 vitreous carbon from SPI Inc. The vitreous carbon surface was rotatable on an axis that was coincident with the rotation axis of a rotatable mass spectrometer detector. Thus, the detector rotated in the plane defined by the molecular beam and surface normal. The beam was directed at the surface at a given angle of incidence with respect to the surface normal, and scattered products were detected at a variety of final angles, with positive final angles

being defined as those opposite the surface normal from the incident beam. Both reactively scattered CO and CO_2 and inelastically scattered O atoms and O_2 molecules were monitored with the mass spectrometer. Time-of-flight (TOF) distributions of these scattered products were collected for a variety of final angles (θ_f) corresponding to a given incidence angle (θ_i). A TOF distribution, $N(t)$, records the number density of a scattered product as a function at its arrival times at the electron-impact ionizer of the detector, located 33.7 cm from the surface. Translational energy distributions, $P(E_T)$, were derived from the TOF distributions using a simple density-to-flux conversion that assumes a monoenergetic incident beam [84, 103, 104]. The $P(E_T)$ distributions are proportional to flux and were integrated to yield the relative flux of the scattered products. The integrated flux of a specific product species as a function of final angle for a given incidence angle yielded a flux angular distribution for that species.

A detailed description of the experiments is given in a previous publication that focused on the scattering dynamics [24]. A temperature survey was conducted by varying the surface temperature from 600 to 2100 K while collecting TOF distributions for fixed incidence and final angles of 45°. Angular distributions were obtained by collecting TOF distributions for final angles of $\theta_f = 10°$ to 80° for incidence angles of $\theta_i = 45°$ and 60°, with fixed surface temperatures of 800 K and 1875 K. Figure 5.1 shows the relative total flux of O, O_2, CO, and CO_2 as a function of surface temperature for $\theta_i = \theta_f = 45°$. It was shown previously [24] that almost all the O atoms scatter impulsively (direct inelastic scattering) from the surface at low temperatures, but as the surface temperature increases above 1100 K, O atoms that have chemisorbed to the surface start to desorb in appreciable fluxes. Thus, the sudden rise in the integrated O-atom flux seen at a surface temperature of 1200 K corresponds to thermally desorbing O atoms. Essentially all of the O_2 scatters impulsively from the surface at all temperatures; therefore, surface temperature does not have an appreciable effect on the scattered flux of O_2. The TOF distributions of CO and CO_2 [24] are well described by Maxwell-Boltzmann distributions characterized by the surface temperature, revealing that most of these products are produced through a Langmuir Hinshelwood type reaction. CO_2 is a minor product even at low temperatures, and the flux of CO_2 is below detectable limits for surface temperatures above 1100 K.In contrast, the flux of CO initially increases dramatically as surface temperature is increased. However, above 1200 K the CO flux begins to decrease as temperature is increased further. Remarkably, the temperature at which

the CO flux begins to decline is also the temperature at which the flux of desorbing O atoms rapidly increases.

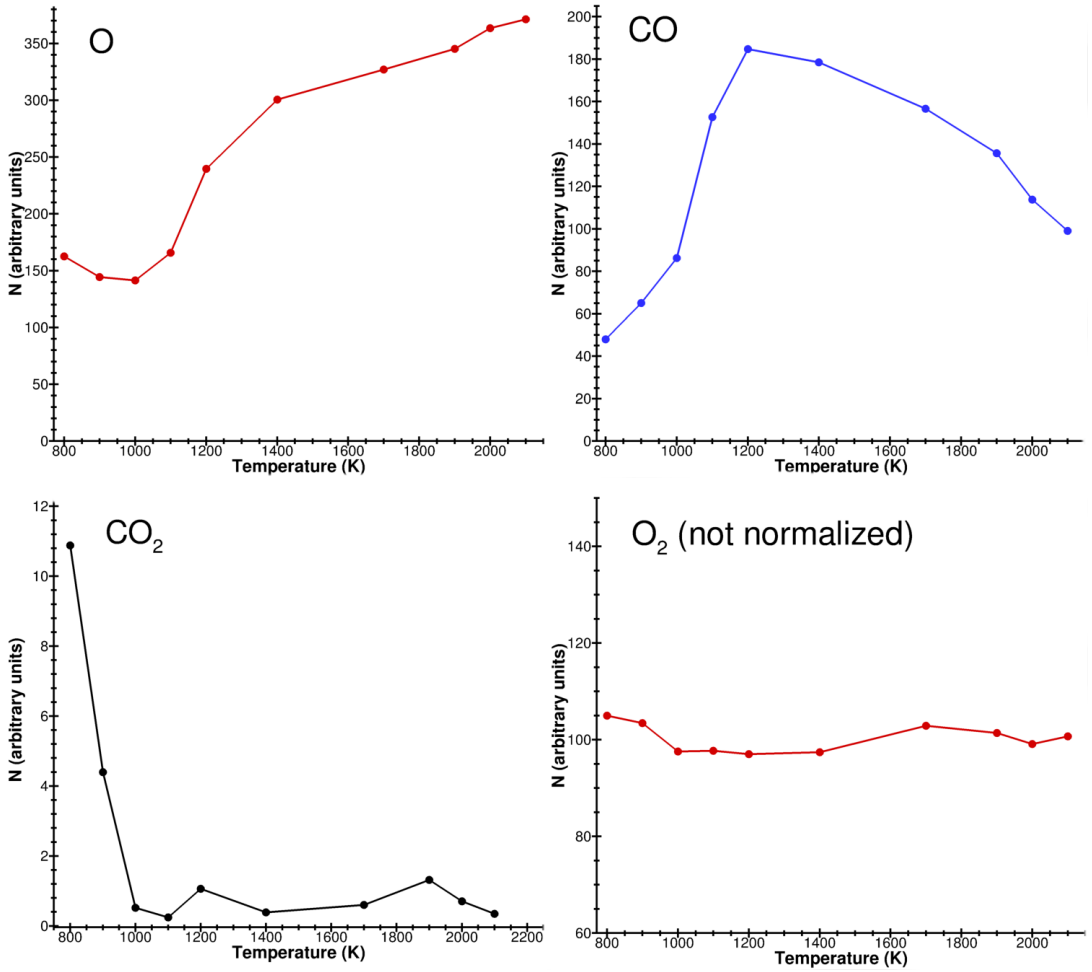

Figure 5.1: Flux of products as a function of surface temperature.

These behavior of the desorbing products are important for two reasons. First, the observation that thermal processes are dominant for all species on a hot carbon surface indicates that the O atom beam acts primarily as a supply of O atoms to the carbon surface, despite the high energy of the beam. That is, the scattering dynamics are not strongly dependent on the beam energy and surface reactions are driven by oxygen coverage and surface temperature. Therefore, such scattering data may be directly

relevant to boundary layer conditions where the material is exposed to a thermal gas composed of partially dissociated oxygen [25]. Second, the rapid increase in thermal scattering of O atoms coincides with the surface temperature where CO production begins to decrease. This correlation is strong evidence that the mechanism to produce CO is dependent on the surface coverage of O atoms. At high temperatures, the O atoms begin to desorb and lead to a reduction in the rate of CO formation, despite increasing energy available from the surface for the reaction to produce CO from adsorbed O atoms. A rate model describing the oxidation of carbon surfaces should capture the competition between these two processes. These molecular level experimental data, which quantify individual oxygen-carbon reaction mechanisms at high temperature, are the first of their kind and provide a new approach to constructing ablation models. These results vitreous carbon may apply to other forms of sp2 carbon, especially when long-range order is limited, as it is in vitreous carbon. Highly ordered graphitic carbon (e.g., HOPG) may behave differently because of the reduced sticking of O atoms on the basal planes. Such carbon surfaces, as well as others, are also being investigated and will be of focus in future work.

5.2 Construction of Reaction Probabilities

Detailed angular distribution data from the experiments are available at surface temperatures of 800 K and 1875 K. Data are available for intermediate temperatures only at a scattering angle of 45°. It is desirable to work with a consistent set of scattering data across the entire temperature range, so we first reconstruct the angular distributions, approximately, for the intermediate temperature conditions.

The temperature survey data are now divided into two regimes: high surface coverage (800-1100 K) and low surface coverage (1200-2100 K). The desorption of O atoms from a carbon surface is a rate activated process with an energy barrier. At low temperatures (800-1100 K), the adsorbed oxygen atoms are below the energy barrier, hence, the surface is populated with oxygen atoms and the carbon surface has high surface coverage. However, as the surface temperature rises above the energy barrier, the O atoms desorb leaving the carbon surface vacant. Thus, at higher surface temperatures (1200-2100 K), the carbon surface has low surface coverage. We assume that the angular distribution profiles are self similar in the respective regimes. Thus, when normalized, the angular

distribution profiles between 800-1100 K (high surface coverage) and 1200-2100 K (low surface coverage) would lie on top of each other. The normalized expressions for 800 K and 1875 K are tabulated in Table 5.1 and the expressions can now be used at the intermediate temperatures and scaled with the flux values measured only for a scattering angle of 45°. The reconstructed angular distributions at all temperatures are shown in Figs. 5.2 and 5.3 for the two regimes.

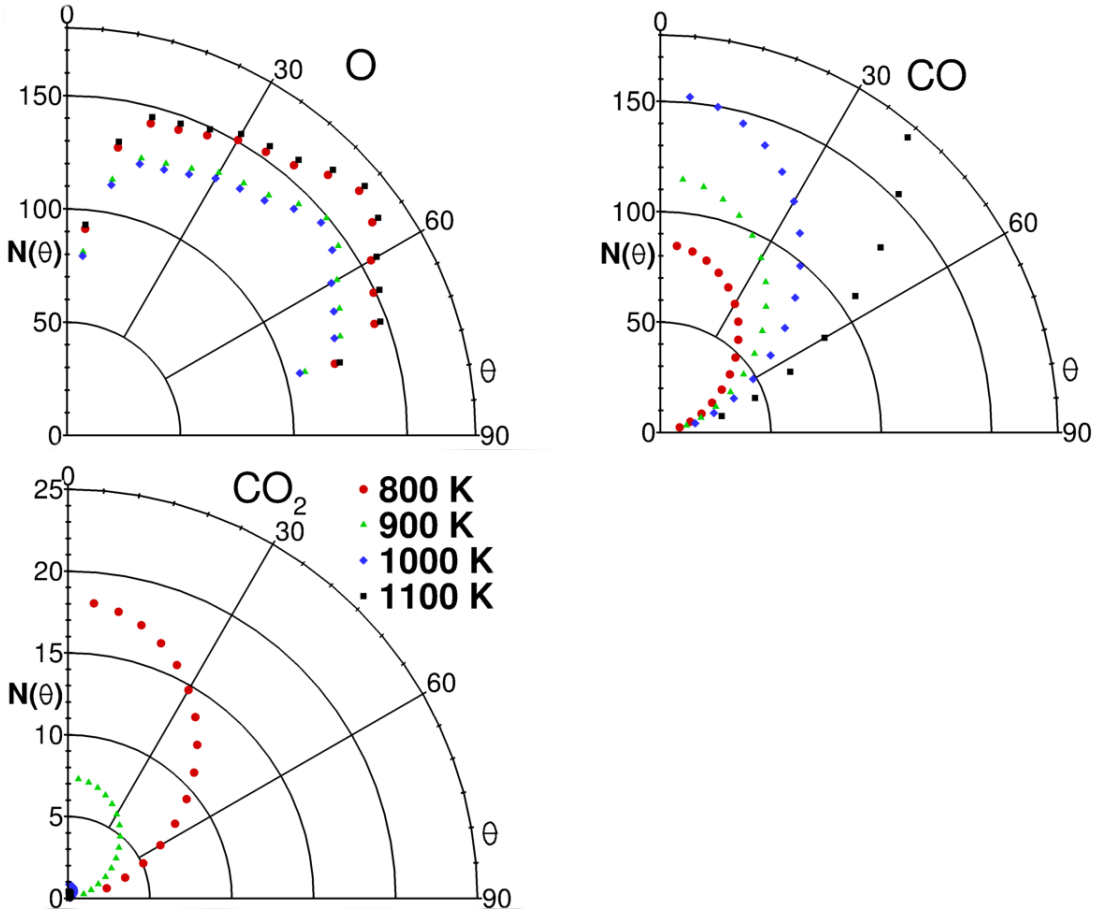

Figure 5.2: Reconstructed angular distributions at high surface coverage in the temperature range of 800-1100 K.

Table 5.1: Expressions for the normalized angular distributions of scattered products. Expressions are fit to full angular distributions from experiment at 800 K and 1875 K, and are used for 800 K $< T <$ 1100 K and 1200 K $< T <$ 2100 K, respectively.

Species	800 K $< T <$ 1100 K	1200 K $< T <$ 2100 K
O	$6.43\text{x}10^{-2}$ - $2.57\text{x}10^{-2}\cos(3.9\theta)$ + $6.41\text{x}10^{-3}\sin(3.9\theta)$ - $1.01\text{x}10^{-2}\cos(7.7\theta)$ + $1.02\text{x}10^{-2}\sin(7.7\theta)$ - $5.11\text{x}10^{-3}\cos(11.6\theta)$ + $6.26\text{x}10^{-3}\sin(11.6\theta)$ - $5.68\text{x}10^{-4}\cos(15.4\theta)$ + $3.78\text{x}10^{-3}\sin(15.4\theta)$	$0.11062\ \cos^{0.9}\theta$
CO	$0.14007\ \cos^{1.662}\theta$	$0.13994\ \cos^{1.65}\theta$
CO_2	$0.1335\ \cos^{1.484}\theta$	-

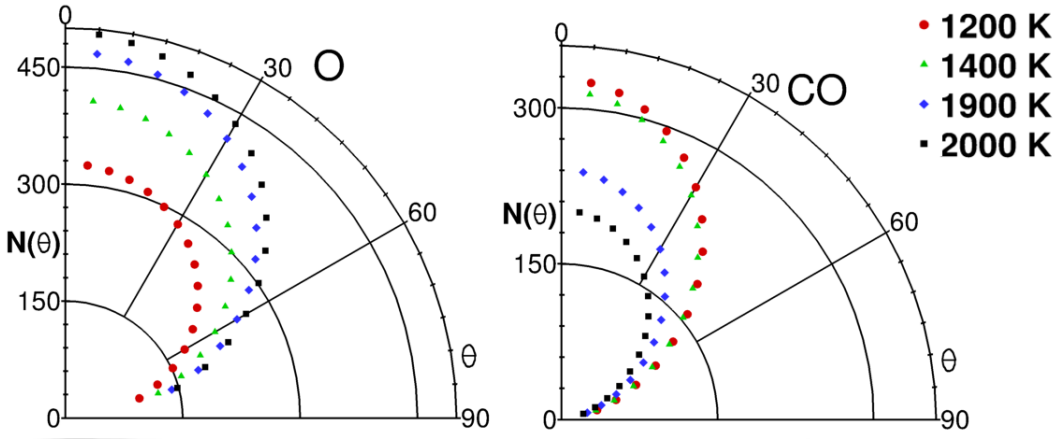

Figure 5.3: Reconstructed angular distributions at low surface coverage in the temperature range of 1200-2000 K. Only four temperatures are shown here.

The angular distributions can be integrated over all angles to obtain the integrated flux. Assuming the reactions are taking place under steady state conditions, the summation of the fluxes provides the total flux leaving the surface and is equal to the incoming total flux (N_{total}) as described in the previous work [25]. The probability for each species (i) can then be obtained as N_i/N_{total} [25], where i is O, CO or CO_2. The surface reaction probabilities are shown in Fig. 5.4. The data indicate that desorption of O atoms begins around 1100 K. Above this temperature, the O atoms desorb faster than the formation of CO molecules. This leads to a decrease in O atom coverage and therefore a decrease in the probability of CO formation above 1100 K.

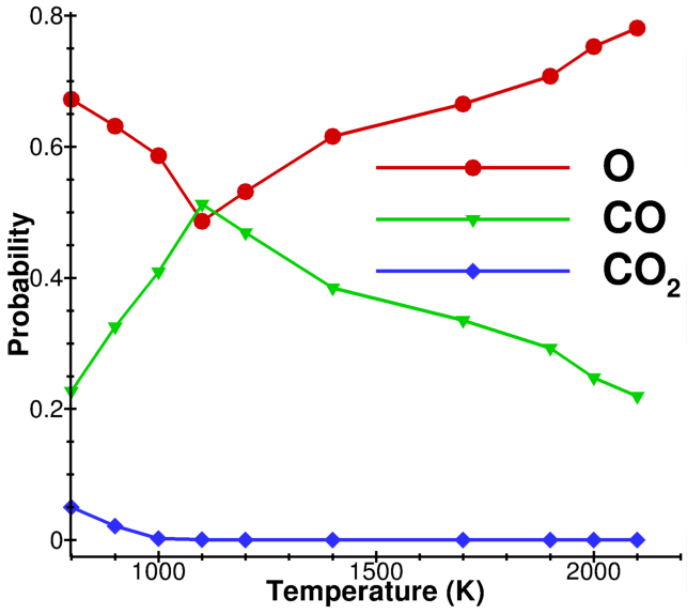

Figure 5.4: Reaction probabilities elucidated from the data of molecular beam experiments.

The observation that the primary oxidation mechanism (the production of CO) reaches a maximum as surface temperature is increased does not follow the Arrhenius rate law used in many finite-rate gas-surface models. However, this observation is consistent with the past experimental studies that investigated the oxidation of carbon surfaces. Previous work from Rosner and Allendorf [21, 105, 106] on both isotropic graphite and pyrolytic graphite using a flow of O atoms and O_2 molecules show that the oxidation reaches a maximum around 1600 K for a pressure of about 10^{-2} Torr. Nagle and Strickland-Constable [107] and Walls and Strickland-Constable [108] performed experiments on reactor-grade graphite and pyrographite and observed the maximum oxidation rate at 1800 K at an operating pressure of approximately 0.1 atm. The work of Eucken [109], Meyer [110] and Duval [111], as well as the molecular beam experiments from Olander *et al.* [112], Shih *et al.* [113] and Liu [114], also indicate a maximum in the temperature-dependent oxidation of carbon surfaces. The theory used at that time to explain the experiments was the two site model proposed by Blyholder *et al.* [115]. The two site model suggested two different reactive sites (A and B) on the

carbon surface. A-sites were more reactive than B-sites and at low temperatures, A-sites dominated the surface. As temperature was increased, A-sites converted to B-sites leading to a maximum in the oxidation rate. Thus, three reactions were used to explain the production of CO: (A) + O $\overset{k_1}{\rightarrow}$ CO, (B) + O $\overset{k_2}{\rightarrow}$ CO and (A) $\overset{k_3}{\rightarrow}$ (B). The researchers at that time focused on fitting the experimental data to deduce the three rate constants with little consensus on the values for the rate constants. The new model proposed in this article (Section 5.3) is based on oxygen surface coverage and is able to accurately predict the maximum oxidation rates found in all of these prior experiments as well as the recent molecular beam experiments discussed above. For example, the new model predicts a maximum oxidation rate at T = 1500 K for a pressure of 10^{-2} Torr and 1800 K for a pressure of 0.1 atm which agree with the work of Rosner and Allendor [21] and Nagle and Strickland-Constable [107]. It must be noted here that experiments were performed on different carbon materials using both O and O_2. The net mass loss and inferred reaction probabilities were different between experiments; however, all materials tested (involving both O and O_2) exhibited the non Arrhenius behavior where the oxidation rate reaches a maximum value.

5.3 New Finite Rate Model

As discussed above, the molecular beam experiments indicate a competition between the formation of CO molecules and the desorption of O atoms. The rate of desorption is modeled based on the activation energy of the desorption reaction, whereas the rate of CO formation is modeled as a function of the incoming flux and a reaction probability. For a specific activation energy for O desorption, the temperature of maximum CO flux (highest reactivity) will shift based on the incident O-atom flux. For example, at higher fluxes of incident atoms, the temperature at which the O-atom desorption rate overtakes the rate of CO formation will shift towards higher temperature. This shift will be quantified in the next section.

The desorption energy can be computed by equating the O-atom desorption rate and the rate of CO formation at 1100 K, since this is the surface temperature where the desorption rate becomes comparable to the CO formation rate. The rate of O-atom desorption can be written by standard transition state theory (TST) [116] as,

$$k_{desorption} = \frac{2\pi m_O k_b^2 T^2}{h^3} e^{\frac{-E_d}{T}} \ , \tag{5.1}$$

where T is the surface temperature in K, m_O is the mass of an oxygen atom in kg, k_b is the Boltzmann constant, h is the Planck's constant, and E_d is the activation energy of desorption. The rate of CO formation can be modeled as $F_O \times P_{CO}$, where F_O is the flux of oxygen atoms to the surface and P_{CO} is a temperature dependent probability of reaction. For the molecular beam experiments, $F_O = 10^{18}$ atoms/m^2/s [24], and the probability of CO formation at $T = 1100$ K is 0.5 (refer to Fig. 5.4). Equating $F_O \times P_{CO}$ to Eq. 5.1 at T=1100 K, the desorption energy for O atoms is the only unknown and is determined to be $E_d = 44277$ K = 368 kJ/mol. This desorption energy, determined only from the molecular beam data, is close to the value suggested in the ZA model [4] and the energy of a single C-O bond [117]. The fact that such molecular beam experiments capture the transition in surface coverage is important, and as a result, the data is highly relevant for ablation model development.

A finite rate model that can be used in CFD simulations can now be written with the following surface reaction mechanisms:

1. Adsorption (sticking) of O atoms on the carbon surface.
2. Desorption of O atoms from the surface.
3. Formation of CO molecules through a surface participating mechanism.
4. Formation of CO_2 molecules through a surface participating mechanism.
5. Formation of CO molecules through direct O atom impact and reaction.

The rates for adsorption, formation of CO, and formation of CO_2, are modeled with the general form: $F_O \times P_i \times \Theta$, where F_O is the local flux of oxygen atoms to the surface, P_i is the probability of reaction i, and Θ is the surface coverage that gives the fraction of adsorbed oxygen atoms on the surface. As an example, consider the rate of CO formation, given in molar specific units by the following:

$$\frac{d[CO]}{dt} = F_O P_i \Theta \ , \tag{5.2}$$

$$F_O = [O] \frac{1}{4} \sqrt{\frac{8 k_b T}{\pi m_O}} \ , \tag{5.3}$$

$$\Theta = \frac{[O(s)]}{B} \ . \tag{5.4}$$

Here, $[O]$ is the molar concentration of oxygen atoms in the gas phase ($\frac{mol}{m^3}$), $[O(s)]$ is the concentration of O adsorbed on the surface ($\frac{mol}{m^2}$) and B is the total site density ($\frac{mol}{m^2}$), which is total number of reactions sites available on the surface. Equation 5.3 is the kinetic theory result for the flux to a surface from a gas at temperature T and molar concentration $[O]$. Since the rate of this reaction can also be expressed as

$$\frac{d[CO]}{dt} = k[O(s)][O] \ , \tag{5.5}$$

we can write the rate constant for this reaction as $k = \frac{1}{4B}\sqrt{\frac{8k_bT}{\pi m_O}}\mathrm{P}_i$, where the reaction probabilities are obtained from the molecular beam data (Fig. 5.4). The final set of reaction mechanisms and rate expressions are shown in Table 5.2. All the rate constants are expressed in the form suggested by Marschall and MacLean [1]. Although the beam experiments were performed at relatively low O atom incident fluxes, the new model is general to any O atom flux. It should be noted that the values in the exponential of the rate constants for reactions 3, 4 and 5 are not activation energies but curve fits to the probabilities obtained from the beam experiments (Fig. 5.4). The new model's applicability under high surface flux conditions, more typical of hypersonic boundary layer conditions, is demonstrated later in Section 5.5. Since the rate model is expressed in the form similar to Marschall and MacLean [1], it can easily be implemented within modern CFD codes.

Table 5.2: New finite rate model. O(s) refers to an O atom adsorbed on the surface and (s) refers to an empty site on the surface, where from conservation, (s) + O(s) = B. C(b) is a carbon atom in the bulk phase. References [1] and [2] contain the naming convention for different species in different phases.

Mechanisms	Rate	Rate constant (k)	Units
O + (s) $\rightarrow$ O(s)	$\mathrm{k}_1[\mathrm{O}][(\mathrm{s})]$	$\frac{1}{4B}\sqrt{\frac{8k_bT}{\pi m_O}}$	$\frac{m^3}{mol\ s}$
O(s) $\rightarrow$ O + (s)	$\mathrm{k}_2[\mathrm{O(s)}]$	$\frac{2\pi m_O k_b^2 T^2}{Bh^3} e^{-\frac{44277}{T}}$	$\frac{1}{s}$
O + O(s) + C(b) $\rightarrow$ CO + O(s)	$\mathrm{k}_3[\mathrm{O}][\mathrm{O(s)}]$	$\frac{1}{4B}\sqrt{\frac{8k_bT}{\pi m_O}} 57.37 e^{-\frac{4667}{T}}$	$\frac{m^3}{mol\ s}$
O + O(s) + C(b) $\rightarrow$ $\mathrm{CO_2}$ + (s)	$\mathrm{k}_4[\mathrm{O}][\mathrm{O(s)}]$	$\frac{1}{4B}\sqrt{\frac{8k_bT}{\pi m_O}} 8.529 \times 10^{-6} e^{\frac{6958.0}{T}}$	$\frac{m^3}{mol\ s}$
O + C(b) + (s) $\rightarrow$ CO + (s)	$\mathrm{k}_6[\mathrm{O}][(\mathrm{s})]$	$\frac{1}{4B}\sqrt{\frac{8k_bT}{\pi m_O}} 0.1203 e^{\frac{2287}{T}}$	$\frac{m^3}{mol\ s}$

5.4 Simulation details

In this section, we describe the specific variants of the ZA model that we compare with our new model. We also describe the methodology used for performing zero-dimensional (0-D) gas-surface simulations.

5.4.1 ZA model and variants

The rate constants of the original ZA model [4] and the modification proposed by MacLean *et al.* [3] can, in some cases, predict significantly different species production rates. The various rate sets are tabulated in Table 5.3. First, the original ZA model proposes multiple activation energies (E) for the CO, CO_2, and O_2 production reactions. We use the activation energies that are consistent with those used in the modified ZA model of MacLean *et al.* (see Table 5.3). Second, the original ZA model suggests two mechanisms for the desorption of O atoms, namely "immobile" desorption and "mobile" desorption. The modified model of MacLean *et al.* [**?**], is consistent with the mobile desorption mechanism. Therefore, as shown in Table 5.3, we consider three variants of the ZA model. These include both the immobile and mobile variants of the original ZA model, denoted as ZA-immobile and ZA-mobile, respectively, as well as the ZA-MacLean-mobile reaction model. All models in Table 5.3 as well as our new model (Table 5.2), require a surface site density (B) to be prescribed. We use a value of $B = 1 \times 10^{-5}$ mol/m^2 as suggested by Zhluktov and Abe [4] and also used by MacLean *et al.* [3]. Finally, we note that the ZA-MacLean-mobile model has been used extensively by Alba *et al.* [7] in CFD simulations of ablation and this model is also used for the CFD simulations presented later in Section 5.5.2.

Table 5.3: ZA model with the rates from MacLean *et al.* [3] and the original work of ZA [4].

Mechanisms	k (ZA-MacLean-mobile)	k (ZA)	Units
1. O + (s) $\rightarrow$ O(s)	$\frac{1}{4B}\sqrt{\frac{8k_bT}{\pi m_O}}$	$\frac{1}{4B}\sqrt{\frac{8k_bT}{\pi m_O}}$	$\frac{m^3}{mol\ s}$
2. O(s) $\rightarrow$ O + (s)	$1.72 \times 10^4 e^{-\frac{45000}{T}}$	$\frac{2\pi m_O k_b^2 T^2}{Bh^3} e^{-\frac{45000}{T}}$ immobile $\frac{k_bT}{h} e^{-\frac{45000}{T}}$ mobile	$\frac{1}{s}$
3. C(b) + O(s) $\rightarrow$ CO + (s)	$2.08 \times 10^9 e^{-\frac{40000}{T}}$	$\frac{k_bT}{h} e^{-\frac{E}{T}}$, E = 40,000 (present) E = 34,000 or 27,000 also proposed [4]	$\frac{1}{s}$
4. O + C(b) + O(s) $\rightarrow$ CO_2 + (s)	$\frac{1}{4B}\sqrt{\frac{8k_bT}{\pi\ m_O}} 0.8 e^{\frac{-2000}{T}}$	$\frac{1}{4B}\sqrt{\frac{8k_bT}{\pi\ m_O}} 0.8 e^{\frac{-E}{T}}$, E = 2000 (present) E = 1000 also proposed [4]	$\frac{m^3}{mol\ s}$
5. 2O(s) + C(b) $\rightarrow$ CO_2 + 2(s)	$3.58\text{x}10^{14} T e^{\frac{-40000}{T}}$	$\frac{k_bT}{Bh} e^{\frac{-E}{T}}$, E = 40,000 (present) E = 34,000 or 13,700 also proposed [4]	$\frac{m^2}{mol\ s}$
6. 2O(s) $\rightarrow$ O_2 + 2(s)	$3.58\text{x}10^{10} T e^{\frac{-31000}{T}}$	$8 \times 10^{-4} \frac{k_bT}{Bh} e^{\frac{-31000}{T}}$	$\frac{m^2}{mol\ s}$
7. O_2 + (s) $\rightarrow$ O + O(s)	$\frac{1}{4B}\sqrt{\frac{8k_bT}{\pi m_{O_2}}} e^{\frac{-14500}{T}}$	$\frac{1}{4B}\sqrt{\frac{8k_bT}{\pi m_{O_2}}} e^{\frac{-14500}{T}}$	$\frac{m^3}{mol\ s}$
8. CO_2 + (s) $\rightarrow$ CO + O(s)	$\frac{1}{4B}\sqrt{\frac{8k_bT}{\pi m_{CO_2}}} 0.9$	$\frac{1}{4B}\sqrt{\frac{8k_bT}{\pi m_{CO_2}}} 0.9$	$\frac{m^3}{mol\ s}$

5.4.2 0-D simulation setup

We perform zero-dimensional simulations to compare the new model with the three variants of the ZA model (ZA-mobile, ZA-immobile, ZA-MacLean-mobile). To do this, we integrate a set of rate equations to steady-state and determine the production rate for each species. The set of rate equations for the new model is given below (Eqs. 5.6 - 5.10) and similar expressions can be written for the ZA models considered. The four equations, along with the conservation equation O(s) + (s) = B, are integrated simultaneously using the Runge-Kutta (RK4) algorithm until the surface coverage ($O(s)/B$) reaches a steady value. The production rates are then computed for each of the species.

$$\frac{d[(s)]}{dt} = -k_1[O_o][(s)] + k_2[O(s)] + k_4[O_o][(s)] \tag{5.6}$$

$$\frac{d[CO]}{dt} = k_3[O_o][O(s)] + k_6[O_o][(s)] \tag{5.7}$$

$$\frac{d[CO_2]}{dt} = k_4[O_o][O(s)] \tag{5.8}$$

$$\frac{d[O]}{dt} = k_5[O_o][O(s)] + k_2[O(s)] \tag{5.9}$$

$$[O(s)] + [(s)] = B \tag{5.10}$$

Initial pressure and temperature conditions are prescribed, where the temperature is that of the gas-surface interface. Specifying a pressure sets the molar concentration of oxygen atoms through the ideal gas law, $p_O = [O]RT$, where R is the universal gas constant. In order to mimic the conditions in the molecular beam experiment this molar concentration is a fixed constant denoted as $[O_o]$. This artificially maintains a constant flux of oxygen atoms to the surface, or in other words, maintains a fixed gas-phase state. Such simulations allow a straightforward comparison between each model and the experimental data. Simulations involving a changing boundary layer state are presented later in Section 5.5.2.

5.5 Results

In this section we compare the ablation behavior predicted by each model for both 0-D simulations as well as for CFD simulations of hypersonic flow over a sharp leading edge.

5.5.1 0-D simulations

Forward Reactions only

In the beam experiments, oxygen atoms strike the surface, possibly react, and the products leave the surface, where they are detected by the mass spectrometer. For this reason, we start by performing zero-dimensional gas-surface simulations where only forward reactions from the ZA model are considered. Specifically, we include forward reactions 1-6 in Table 5.3 and do not consider reactions 7 and 8 since they involve gas-phase CO, CO_2, and O_2 species impacting and reacting with the surface, which did not occur in the experiments. Recall from the discussion of Fig. 5.1, that the small amount of O_2 in the beam was observed to scatter without reacting with the surface. It is interesting to note that reaction 8 turns out to be the most critical reaction for the ZA model within a CFD calculation, as this reaction largely dictates the CO/CO_2 concentration near the surface. This is discussed in the next section when we consider the backward reactions.

First we consider an oxygen atom flux approximately equal to that used in the molecular beam experiment. In the experiment, the beam flux was $\sim 10^{18}$ atoms/m^2/s. Using Eq. 5.3, this gives a fixed value for the molar concentration of atomic oxygen of $[O_o] = 1.2\times10^{-9}$ mol/m^3. This value corresponds to a low partial pressure of $p_O =$

4.75×10^{-5} Pa. Figure 5.5 plots the relative flux of reaction products leaving the surface predicted by the new model compared to flux predicted by the ZA-immobile model, the ZA-mobile model, and the ZA-MacLean-mobile model. Several interesting results can be observed from these simulations.

All models predict a sudden change in reactive fluxes when the surface temperature reaches approximately 1100 K. This is a result of the surface temperature dependence in the reaction rates of all models considered. Since oxygen desorption in ZA-immobile and new model and CO formation in ZA-mobile and ZA-MacLean-mobile are calculated in the same manner, and the desorption energy calculated from the molecular beam data that is used in the new model is very close, this agreement is expected. Although the ZA and new model have a similar surface coverage dependence, there are striking differences in the production rates of each species. At low surface temperature (high surface coverage conditions), CO_2 is the dominant product for all variants of the ZA model. In contrast, the new model predicts mostly CO and a small amount of CO_2 production, which is consistent with the molecular beam experiments. Therefore, a major difference between the new model and existing ZA models is that the new model predicts virtually all CO production, in agreement with the molecular beam experiments, while the ZA models predict virtually all CO_2 production.

In the high temperature regime (low surface coverage conditions), the new model predicts an increase in O desorption and reduction in CO production. The ZA models have very different behavior in this regime depending on the choice of the ZA model variant that is used. For the ZA-immobile model, O-atom desorption is the dominant process, while the ZA-mobile model predicts CO as the dominant product. In the ZA model, CO formation is expressed as an activated desorption process, similar to the desorption of O atoms (Table 5.3). Thus, depending on the rate constants, CO or O will be the dominant surface reaction product. This is illustrated in Table 5.4, where for the ZA-mobile and ZA-MacLean-mobile models, the production of CO dominates, however for the ZA-immobile model the rate of O atom desorption will dominate.

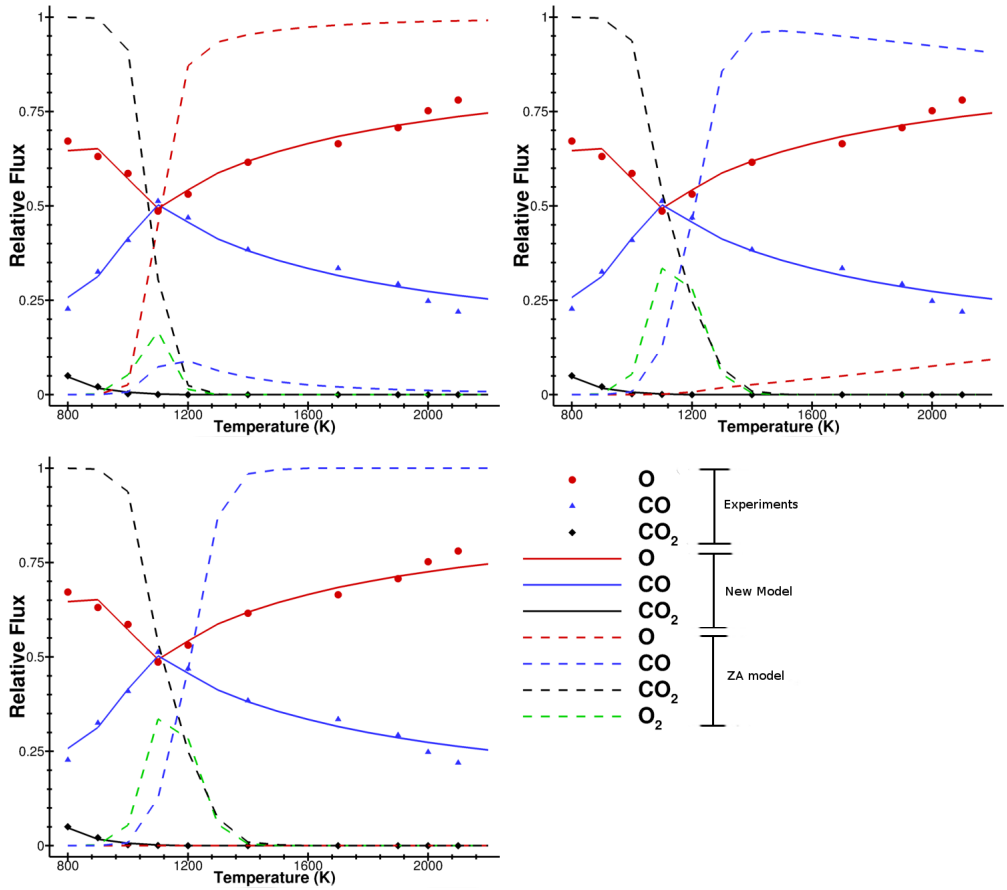

Figure 5.5: Comparison of relative flux between the new model and ZA models at a gas pressure of 4.75×10^{-5} Pa with a) ZA-immobile, b) ZA-mobile and c) ZA-MacLean-mobile. Simulated results are also compared to the molecular beam data obtained under similar atomic oxygen flux conditions.

It is interesting to note that the desorption rate constant in the ZA-immobile model has an inverse dependency on site density B, and that increasing the site density lowers the desorption rate, therefore eventually allowing the rate of CO production to dominate. This complex dependency of oxidation products on site density for the ZA-immobile model is discussed in the next section.

Table 5.4: Rate comparison of O desorption and CO formation.

	O(s) → O + (s)	O(s) + C(b) → CO + (s)	
ZA-immobile	$k_O = \frac{2\pi m_O k_b^2 T^2}{Bh^3} e^{-\frac{45000}{T}}$	$k_{CO} = \frac{k_b T}{h} e^{-\frac{40000}{T}}$	if B = 10^{-5} mol/m^2, $k_O > k_{CO}$
ZA-mobile	$k_O = \frac{k_b T}{h} e^{-\frac{45000}{T}}$	$k_{CO} = \frac{k_b T}{h} e^{-\frac{40000}{T}}$	$k_{CO} > k_O$
ZA-MacLean-mobile	$k_O = 1.72 \times 10^4 - \frac{45000}{T}$	$k_{CO} = \frac{k_b T}{h} e^{-\frac{40000}{T}}$	$k_{CO} > k_O$

The mass flux from the surface is compared in Fig. 5.6 between the new model and the three variants of the ZA model. The mass flux gives an indication of the amount of oxidation occurring on the carbon surface. The results are consistent with the expected observations of relative flux. The new model predicts higher mass flux for oxidation products (CO or CO_2) compared to the ZA models at low surface temperatures (high surface coverage conditions). However, the mass flux predicted by the ZA models is higher at high surface temperature (low surface coverage conditions), if the mobile desorption rate is used.

The results discussed above corresponded to a low incident flux of oxygen atoms or, equivalently, a low partial pressure for the gas next to the surface in order to match the molecular beam experimental flux conditions. In hypersonic flows, the flux of atoms to the surface would be much higher. To this purpose, we compare model predictions for a flux of 10^{25} atoms/m^2/s. This corresponds to a partial pressure of $p_O = 475$ Pa and a corresponding $[O_o]$ value of 0.06 mol/m^3. Figure 5.7 compares the relative flux of oxidation products for this higher pressure condition. Similar behavior is observed compared to the low flux conditions (Fig. 5.5), however, with high flux conditions the temperature at which the surface coverage changes is now shifted to a higher value. As seen in Fig. 5.7, this transition now occurs at a surface temperature close to 1800 K, which is in good agreement with a number of experimental results in the literature, for example, as mentioned previously in Section 5.2, the work of Rosner and Allendor [21], Nagle and Strickland-Constable [107] among others. Thus, although the new model was constructed using only molecular beam data at low incident flux, the model successfully captures surface-coverage and is applicable over a wide range of pressures and temperatures. This is one of the most important aspects of the current article. As seen in Fig. 5.7, under higher pressure conditions (typical of a hypersonic boundary layer), the new model predicts all CO production up until surface temperatures near 1800 K , while existing ZA models predict all CO_2 production and no CO production. Furthermore, at higher temperatures, the new model predictions for reactive species

fluxes are also completely different then existing ZA models, which differ significantly among themselves. These differences would directly influence the overall ablation rate and boundary layer composition predicted in CFD simulations.

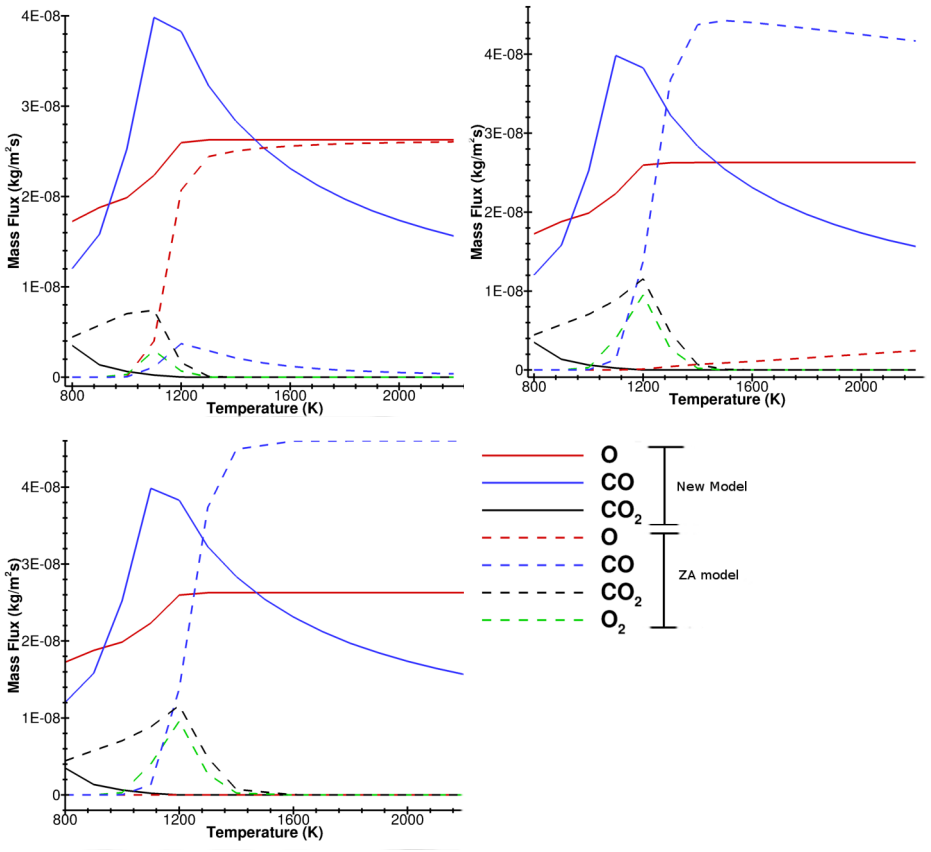

Figure 5.6: Comparison of mass flux between the new model and the ZA model at a gas pressure of 4.75×10^{-5} Pa with (a) ZA-immobile, (b) ZA-mobile and (c) ZA-MacLean-mobile.

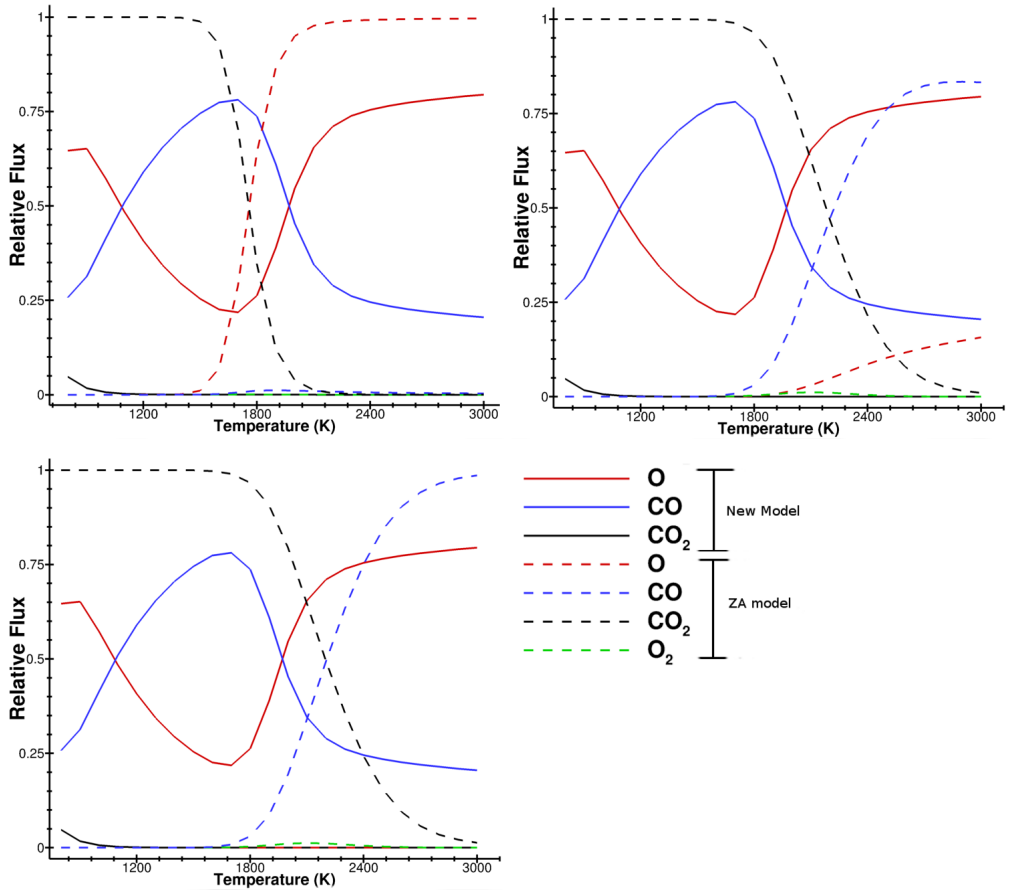

Figure 5.7: Comparison of relative flux between the new model and the ZA model at a gas pressure of 475 Pa with (a) ZA-immobile (b) ZA-mobile and (c) ZA-MacLean-mobile.

Backward rates in ZA model

In general, the ZA model considers all reactions in the reverse direction and, in addition, sublimation reactions can be included in the model. As discussed in Refs. [2, 4, 118], only a subset of backward reaction rates can be independently specified. The remaining backward rates should be determined through equilibrium considerations, such that a gas-surface system in chemical equilibrium should remain in the equilibrium state. To ensure this condition, backward reaction rates should be evaluated using the forward reaction rate and equilibrium constants.

As an example, consider the production of CO (reaction 3 in Table 5.3). The equilibrium constant for this reaction (K_{CO}) can be written in terms of the equilibrium constants of other reactions,

$$K_{CO} = \frac{k_f^3}{k_b^3} = \frac{[CO]\ [(s)]}{[C(b)]\ [O(s)]} = \frac{K_{Sub}}{K_{Diss} K_{Ads}}\ . \tag{5.11}$$

Here, K_{Sub} is the equilibrium constant for the sublimation reaction: C(b) + (s) $\leftrightarrow$ C + (s), K_{Diss} is the equilibrium constant for the gas-phase dissociation reaction: CO + M $\leftrightarrow$ C + O + M, and $K_{Ads} = k_f^1/k_f^2$ is the equilibrium constant for the adsorption reaction (note that, in Table 5.3, reaction 2 is the reverse of reaction 1). Therefore, if the forward and backward rates are specified for the adsorption reaction, the sublimation reactions, and the gas-phase dissociation reaction, the equilibrium constant K_{CO} is determined by Eq. 5.11. If the forward rate of CO production (k_f^3) is specified (reaction 3 in Table 5.3), then the backward rate (k_b^3) should not be independently specified, rather it should be calculated from Eq. 5.11. The backward rates for the other reactions are calculated in a similar way.

Zero dimensional simulations are performed using the ZA model, similar to the previous set of simulations, but now including backward rates. The gas phase equilibrium constants were computed using partition functions with a pressure of 475 Pa, and the sublimation reaction parameters are those of Havstad and Ferencz [12]. While the concentration of atomic oxygen is still fixed (at $[O_o] = 0.06$ mol/m^3), as CO, CO_2, and O_2 products are created during the simulations (analogous to Eqs. 5.6 - 5.9), there are now additional mechanisms for these species to undergo reverse reactions. It is also important to note that unlike the previous section (Section 5.5.1), all reactions listed in Table 5.3 are now considered for this analysis. Later, in this section, we will also perform simulations where the last reaction (reaction 8) in Table 5.3 is not included. The integration of the system of rate equations (including backward mechanisms) is performed using the RK4 method, in the same manner as previously described (Section 5.4).

Figure 5.8 plots the mass flux of CO, CO_2 and O_2 respectively, now including backward reactions for ZA-immobile and ZA-mobile models. It can be observed that the backward rates have a significant effect on the product composition predicted by the ZA model. While previously the dominant product was a competition between CO_2 and O for the immobile model, and between CO_2 and CO for the mobile models, the dominant product with backward reactions becomes O_2. This is a direct result of the reaction,

O_2 + (s) $\leftrightarrow$ O + O(s) (reaction 7 in Table 5.3), which has a very small equilibrium constant. Thus, an Eley-Rideal (ER) recombination of O atoms into O_2 is preferred in the ZA model when backward rates are included.

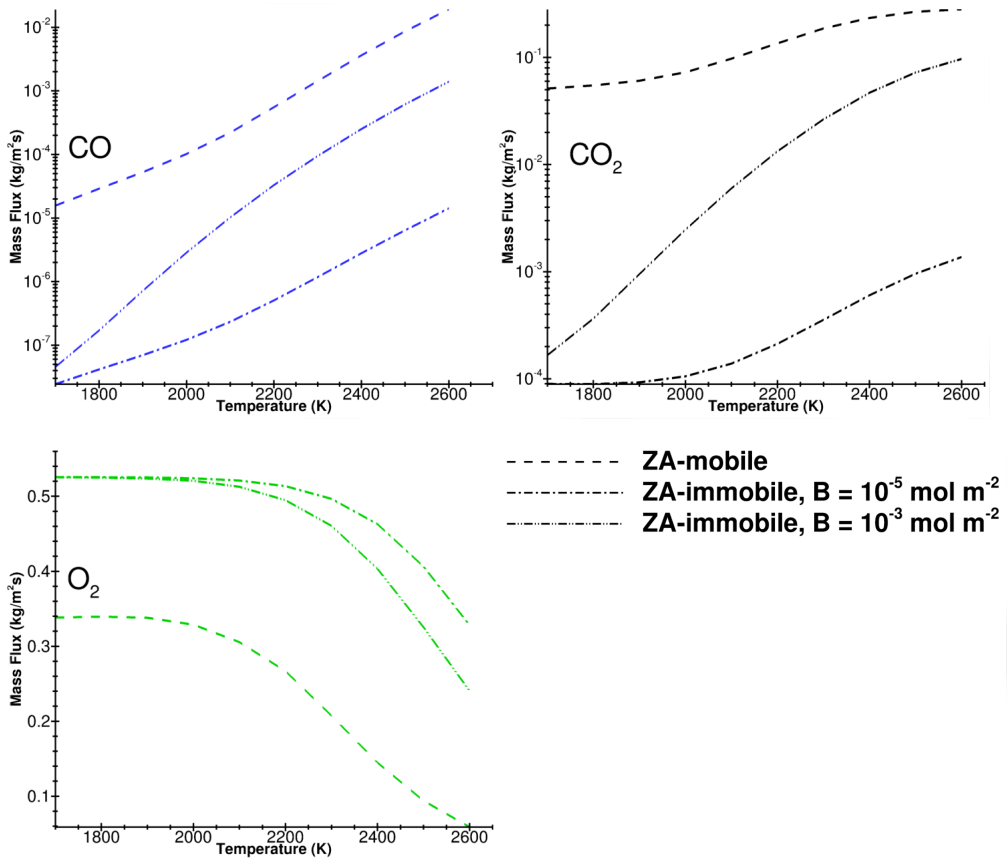

Figure 5.8: Mass flux for (a) CO, (b) CO_2 and (c)O_2 for ZA model with backward rates.

It can also be seen that the ZA-immobile model produces more O_2 than the ZA-mobile model. This can be understood by looking at the backward rate for this ER recombination reaction. The equilibrium constant for the reaction, O_2 + (s) $\leftrightarrow$ O + O(s) is shown in Eq. 5.12. Here, K_{Diss} is the equilibrium constant for the gas-phase dissociation reaction: O_2 + M $\leftrightarrow$ O + O + M, k_f^1, k_f^2 are the adsorption and desorption rate constants respectively (see discussion above). Therefore, the backward rate for this reaction is $k_b^7 = \frac{k_f^7 k_f^2}{K_{Diss} k_f^1}$. Since, the desorption rate constant (k_f^2) is higher for ZA-immobile as compared to ZA-mobile, a higher O_2 mass flux is observed when the

ZA-immobile model is used. The molecular beam experiments show no evidence of such recombination reactions at higher temperatures and only a hint of this reaction at lower temperatures.

$$K_{O_2} = \frac{k_f^7}{k_b^7} = \frac{[O]\ [O(s)]}{[O_2]\ [(s)]} = K_{Diss} K_{Ads} \ = K_{Diss} \frac{k_f^1}{k_f^2}. \tag{5.12}$$

The effect of site density B can also be seen from the results in Fig. 5.8. The original work of Zhluktov and Abe suggested a value of 10^{-5} mol/m^2, which corresponds to the number of carbon atoms in the plane of a hexagonal graphene sheet. However, this value can vary over several orders of magnitude based on the carbon material microstructure considered. When the site density (B) is increased, a significant increase in CO mass flux is seen when the ZA-immobile model is used. This occurs because the rate constant for the desorption of oxygen atoms (reaction 2 in Table 5.3) becomes smaller than the rate constant for the formation of CO through reaction 3.

Finally, the importance of the last reaction in Table 5.3 (reaction 8), CO_2 + (s) $\leftrightarrow$ CO + O(s) is examined. The equilibrium constant for this reaction is very small and most of the CO produced is converted to CO_2 because of this reaction. To demonstrate this, we run the same set of calculations but we now exclude reaction 8. Figure 5.9 compares results from the simulations of excluding (Reaction Off) and including the reaction (Reaction On). It can be seen from Fig. 5.9 that CO mass flux is much higher when the reaction is excluded because there is no mechanism to convert CO into CO_2.

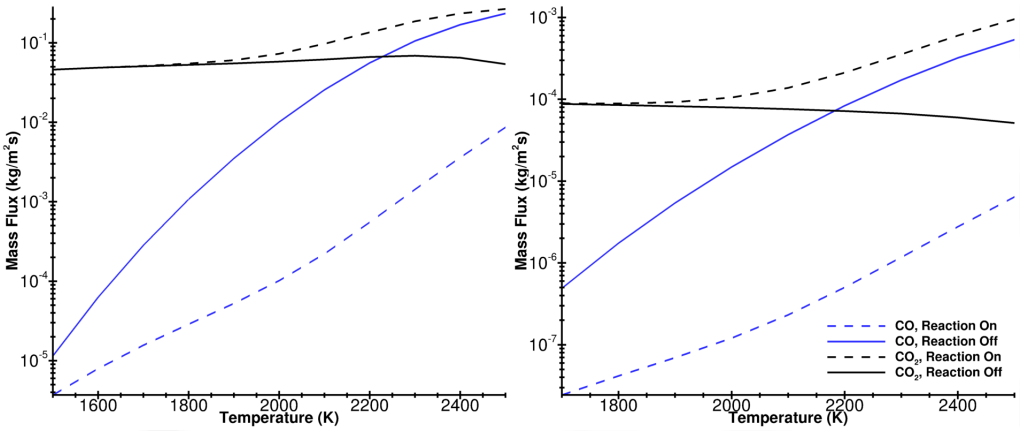

Figure 5.9: Mass flux for (a) ZA-mobile and (b) ZA-immobile with and without reaction 8 from Table 5.3, CO_2 + (s) $\leftrightarrow$ CO + O(s).

It is important to note that the influence of reaction 8 in the ZA-MacLean-model was also analyzed by Alba *et al.* [7]. As discussed in the introduction, Alba used the ZA-MacLean-mobile model in the US3D CFD code to simulate high-enthalpy ablation experiments performed at the University of Queensland. A carbon material sample was resistively heated to high temperature and exposed to short duration hypersonic flow. Spectroscopic measurements were taken in the boundary layer, where the main signature measured was radiation from CN molecules [17]. The CFD simulations with the ZA-MacLean-mobile model predicted virtually all CO_2 leaving the surface and within the boundary layer. This resulted in little production of CN in the boundary layer and predicted much less CN radiation than observed experimentally. In order to improve agreement with experiment, several modifications were made to the ZA-MacLean-mobile model. Initially, surface nitridation reactions were added to the model [119], however, this did not produce enough CN to match the experimental CN radiance. Two other modifications were made in order to increase the CO composition in the boundary layer. Specifically, the pre-exponential factor for reaction 3 (in Table 5.3) was increased by one order of magnitude, and the forward and backward rate coefficients were switched for reaction 8, thereby favoring the dissociation of CO_2 on the surface to produce CO in the gas phase and an adsorbed oxygen atom. After incorporating these modifications, the simulation predictions for CN radiance in the boundary layer agreed well with the experimental data. The new model, formulated using only data from the molecular beam experiments also predicts CO to be the dominant reaction product, and is therefore fully consistent with the final modified ZA model of Alba *et al.* [7].

In summary, as originally published, the ZA model includes a number of variants, including various activation energies and immobile vs. mobile desorption mechanisms. It is not clear which variant should be used and we have shown that none of the variants produce results that are consistent with the molecular beam data. The forward reactions of the existing ZA models predict dramatically different products and trends with temperature than the molecular beam experiments. A reverse reaction included in existing ZA models favors surface recombination forming O_2, whereas the molecular beam experiments show clearly that this reaction is rare. Also a second reverse reaction in the existing ZA models favors recombination of CO into CO_2 through a surface reaction which should not occur at high temperatures, and is not consistent with the amount of CN radiation measured in high enthalpy ablation experiments. Finally, as analyzed in

this section, there are many complicated aspects of the forward and backward reactions in existing ZA model variants, for example the dependence on surface site density, B.

In contrast, the new model contains only the reaction mechanisms observed in the molecular beam experiments and the rate expression for each reaction is determined individually by the molecular beam data. The new model is able to capture the expected surface coverage dependence of the reaction rates and is fully consistent with available high enthalpy ablation testing data. While careful assessment and adjustment of existing ZA rate parameters based on high enthalpy ablation tests is certainly useful, the methodology proposed in this article represents an entirely new way of formulating an ablation model for use in CFD. The next section incorporates the new model within the US3D CFD code and presents simulation results for hypersonic flow over a sharp leading edge at a variety of free-stream flow conditions relevant to US Air Force vehicles.

5.5.2 CFD simulations

CFD simulations of hypersonic flow over an 8° sphere-cone geometry with a 10 cm radius leading edge are performed using the US3D [120] with both the ZA-MacLean-mobile model and the new model. The freestream velocity is 7 km/s with conditions corresponding to altitudes of 50, 40, 30, and 25 km. These simulation conditions are the same as those used by Candler *et al.* [16] in a recent study that compared a number of ablation models.

The leading edge geometry for the 40 km case with temperature contours using the new model is shown in Fig. 5.10. The simulations were performed using 5 species reacting air chemistry with rates from Park *et al.* [121, 122]. The surface temperature distribution around the surface was prescribed and was held fixed for the simulations. Specifically, the surface temperature distribution was determined by scaling the surface temperature obtained from a CFD simulation using a non-ablating, non-catalytic, radiative-equilibrium boundary condition to approximate the temperature distribution for an ablative surface. This temperature distribution is shown in each of Figs. 5.11 - 5.14, as the black dotted line, for reference. Also, plotted for reference are contours of the CO mass fraction for the 40 km case (Fig. 5.10), and also the surface pressure distributions for each case (Fig. 5.10) using the new model.

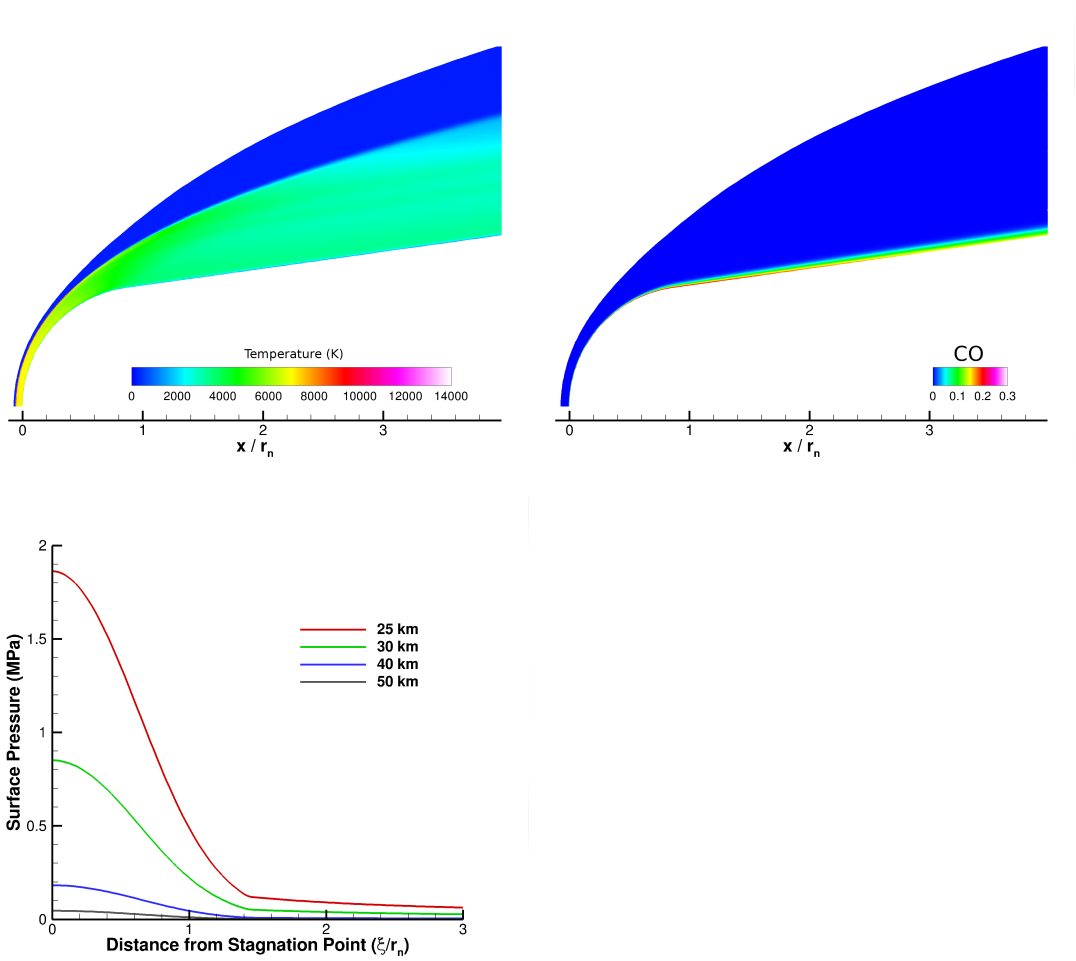

Figure 5.10: (a) Temperature contours, and (b) CO mass fraction contours for the 40 km altitude; (c) surface pressure for all the cases.

The ZA-MacLean-mobile and new models were implemented into the US3D code based on the work of Marschall and MacLean [1, 2] The sublimation reactions for carbon taken from the ZA model [4] are included in the CFD simulations for both models. The surface state is computed by first balancing the production and destruction of adsorbed atoms. Then, the surface mass balance equation (Eqn. 5.13) is solved.

$$-(\rho D_k)_w \nabla_w y_k + (\rho v)_w y_{kw} = M_k \dot{\omega}_k \tag{5.13}$$

D is the diffusivity, ρ is the density at the wall, y_k is the mass fraction of species k,

v_w is the surface velocity, M_k is the molecular weight of species k and $\dot{\omega_k}$ is the rate of production of species k. The surface velocity is obtained by summing over all the species, $(\rho v)_w = \sum_k M_k \dot{\omega_k}$. Equation 5.13 is solved iteratively until the surface velocity converges.

Figures 5.11 - 5.14 contain the results of the simulations. The net mass flux of each species away from the surface is plotted around the sphere-cone geometry, starting at the stagnation point. A negative species mass flux means that the species is being removed from the flow field due to surface reactions. The most notable such species is atomic oxygen, however, depending on the model and flight conditions, other species are seen to have a negative net mass flux at the surface. Results using the ZA-MacLean-mobile model are plotted on the left, and results using the new model are plotted on the right. The total mass flux away from the surface (representative of the ablation rate) is plotted as the solid black line in each figure.

The first major result apparent from the comparisons is that the total mass flux, predicted by both the ZA-MacLean-mobile and the new model, is similar. Specifically, for the 50 km case the new model predicts approximately 42% higher total mass flux than the ZA-MacLean-mobile model, and for the 40 km case, approximately 33% higher mass flux. As the altitude decreases (both 30 km and 25 km cases) the total mass flux predictions by both models become very close. This level of agreement in the overall ablation rate is a result of the fact that the reaction probabilities for atomic oxygen (whether forming CO or CO_2) are high, for example they typically range between 0.1 and 1, both in existing ZA models and as observed in molecular beam experiments. This is an important validation of the new model, since the ZA-MacLean-mobile model has been adjusted and validated based on recession rates observed in high-enthalpy ablation tests [3], and therefore demonstrating such agreement is important. One interesting prediction of the new model is that a finite ablation rate persists onto the conical surface (far from the stagnation point), whereas the ZA-MacLean-mobile model predicts that the ablation rate essentially drops to zero after approximately 1.5 nose radii (r_n) from the stagnation point.

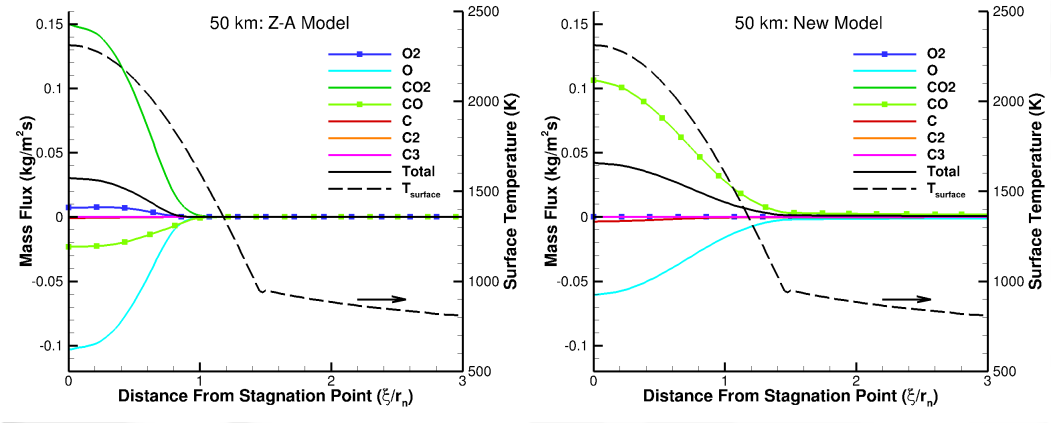

Figure 5.11: Surface mass flux for ZA (left) and new model (right) along the surface at 50 km.

In contrast to the overall mass flux predictions, the predictions for individual species fluxes are completely different between the ZA-MacLean-mobile and the new model. This may be expected based on the 0-D simulations presented in the previous section, however, large differences are shown to persist for full CFD simulations at relevant hypersonic flight conditions. We emphasize that, in contrast to the 0-D simulations, the CFD simulations include a boundary layer next to the surface including gas-phase chemistry and species diffusion within the boundary layer. At the high altitude conditions (50 km and 40 km cases), although the overall mass flux is similar, the new model predicts that this is entirely due to the production of CO. In stark contrast, the ZA-MacLean-mobile model predicts that the mass loss is due entirely to the production of CO_2. In fact, as noted earlier for the 0-D simulations, the ZA-MacLean-mobile model actually predicts that CO is removed on the surface to produce CO_2 (through reaction 8 of Table 5.3 in the reverse direction), and also predicts a noticeable amount of O surface recombination into O_2. Again, these processes are inconsistent with the molecular beam experiments [24] and previous experimental studies [21, 107, 113], and do not occur for the new model.

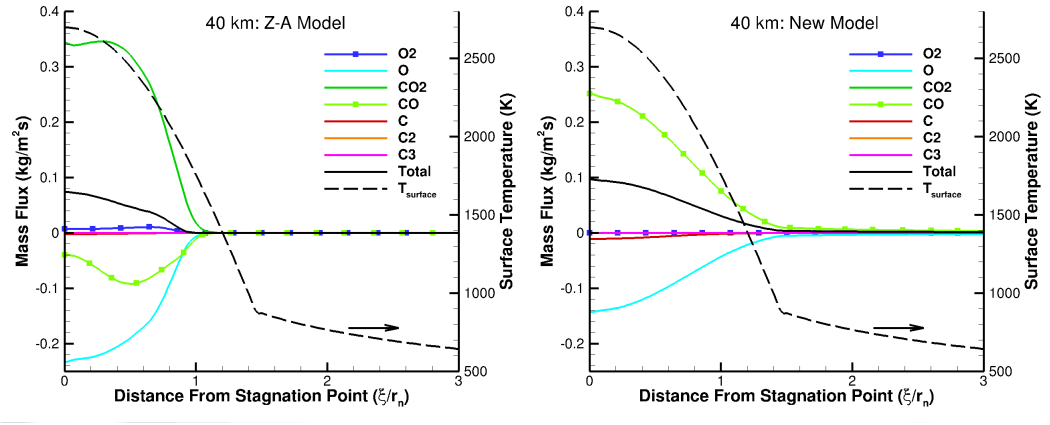

Figure 5.12: Surface mass flux for ZA (left) and new model (right) along the surface at 40 km.

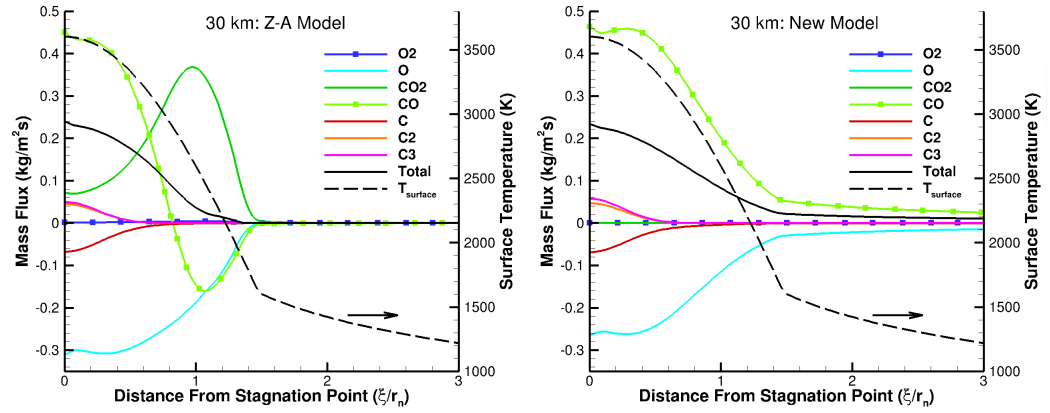

Figure 5.13: Surface mass flux for ZA (left) and new model (right) along the surface at 30 km.

At the low altitude conditions (30 km and 25 km cases), the new model still predicts that CO production is responsible for the majority of mass loss with no contribution from CO_2 production as observed in the molecular beam experiments. In contrast, the ZA-MacLean-mobile model predicts significant CO production near the stagnation point (at high temperature and pressure), however, a drastic change occurs as the temperature drops around the leading edge. Specifically, CO becomes consumed at the surface,

to a similar degree as atomic oxygen, and CO_2 production becomes dominant. As the temperature further decreases, further from the stagnation point, then the total mass loss drops to essentially zero beyond 1.5 nose radii. As expected, the sublimation reactions become increasingly important at lower altitudes where the surface temperature is larger.

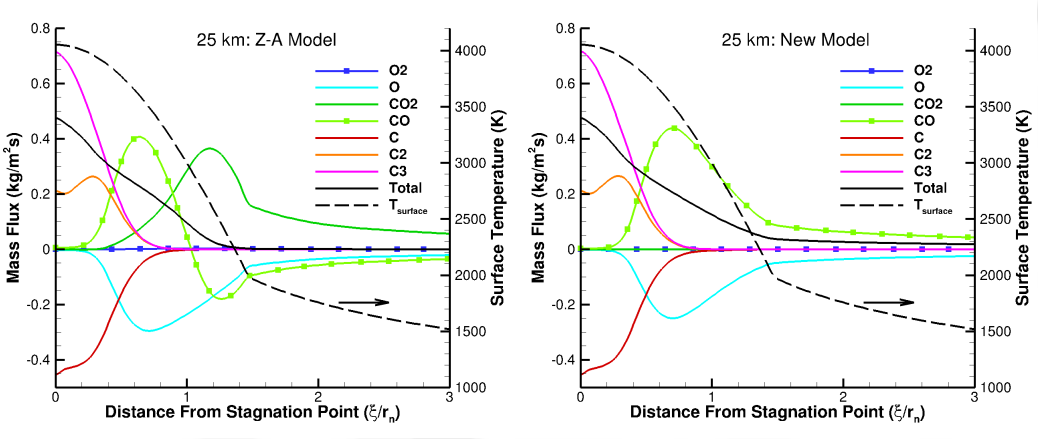

Figure 5.14: Surface mass flux for ZA (left) and new model (right) along the surface at 25 km.

5.6 Conclusions

A new finite rate model has been developed using the data from molecular beam experiments [24]. The experimental data contained integrated fluxes for O, CO, and CO_2 which were used to deduce surface reaction probabilities as a function of gas-surface temperature. The reaction probabilities indicated that the CO probability reached a maximum at 1100 K after which the desorption of oxygen atoms from the surface dominated the surface kinetics. Desorption of oxygen atoms was modeled as an activated process with an energy barrier which was found to be 44277 K and was close to the value suggested by Zhluktov and Abe [4], the energy of a single bond between carbon and oxygen. The new model was built based on the surface coverage approach of Zhluktov and Abe but purely from the molecular beam experiments that provide true surface oxidation probabilities.

The new model was compared with the ZA model (both immobile and mobile desorption assumption) and its variant proposed by MacLean *et al.* (ZA-MacLean-mobile) using a 0-D approach and CFD simulations. The 0-D simulations showed that at lower surface temperatures (high surface coverage conditions), the ZA model predicted CO_2 as the dominant oxidation product in contradiction to the new molecular beam results and past experiments. At higher surface temperature (low surface coverage conditions) the ZA-mobile predicted that CO would be the dominant product when only forward reactions were included. However, if all backward rates were included, the reaction, CO_2 + (s) $\leftrightarrow$ CO + O(s) converted all the CO into CO_2. Most importantly, the ZA model did not predict that oxidation would reach a maximum at a certain surface temperature. The new model that has been developed predicted similar overall ablation rates as the ZA model (and variants), however, the individual mechanisms and rate parameters were completely different. The dominant species produced in the new model was CO and it reached a maximum based on the surface pressure and temperature.

The comparisons presented in this article clearly show how different finite-rate gas-surface reaction models can predict similar macroscopic behavior (overall mass loss rates, for example), despite the molecular level details (mechanisms and rate parameters) being completely different. These results underscore the difficulty in parametrizing gas-surface reaction models based on macroscopic observables (recession rate and heat flux) alone, since many different model formulations could agree with the observations. The choice of new model reaction mechanisms was determined solely by the scattered products observed in molecular beam experiments, and the rate parameters were determined through an analysis of the temperature dependence of the scattered products. The general new model was formulated using only this data, it was incorporated within state-of-the-art hypersonic CFD simulations, and produced accurate results over a range of conditions relevant to US Air Force vehicles. The discovery that measurements taken in molecular beam facilities are able to determine individual reaction mechanisms, including dependence on surface coverage, opens up an entirely new way of constructing ablation models.

Chapter 6

Conclusions

Conclusions from the individual studies were provided in the respective chapters. In this chapter, broad conclusions from this work and future steps are discussed.

A new approach to building a gas-surface model was undertaken where gas-surface interactions were probed individually to understand relevant fundamental processes. This understanding was then used to build a predictive model that is accurate over a wide range of pressures and temperatures.

Initial computational studies were performed of HOPG exposed to a 5 eV atomic oxygen beam, matching the experiments of Nicholson, Minton, and Seibner [8, 40] using molecular dynamics. The MD simulations were performed using LAMPPS and ReaxFF potential. The result predicted by the MD simulations is a wide but shallow cylindrical etch pit, in qualitative agreement with experimental observation. The dominant chemical mechanisms leading to the production of O_2, CO_2 and CO were isolated on the actual oxidized HOPG surface (a simulated multilayer etch pit) and further investigated using trajectory analysis to obtain reaction probabilities. Analysis was also done using low temperature (1 K) MD to predict the energy barriers of the important reactions.

Next, the role of microstructure in carbon ablators was examined. DSMC was used to simulate flow around the microstructure of a non porous carbon ablator that protrudes into the flowfield to understand its effect on macroscopic reaction rates. The surface oxidation reaction to form CO was modeled with three different microscopic probabilities, $r = 0.29, 0.029, 0.0029$ which covered the high, intermediate and low probabilities respectively. It was found that at high surface reaction probability, the surface reactions were in the diffusion dominant regime and changing the surface area of the

microstructure did not have an effect on the concentration profiles. However, a significant effect was observed in the low reaction probability case or the reaction dominant regime.

Molecular beam experiments performed at high surface temperature [24] revealed that a majority of surface reaction products accommodate to the surface and are scattered thermally. The experiments provided detailed data on the relative magnitudes of O, O_2, CO, and CO_2 scattering from a representative material sample, made of vitreous carbon. It was also found that reactions do not depend on beam energy and the beam only provides a source of O atoms to the surface. Further, the beam data was used to deduce surface reaction probabilities at 800 K. The surface reaction probabilities were incorporated into MGDS solver and molecular simulations were performed of high temperature dissociated oxygen reacting with a carbon-carbon composite material, where the microstructure was resolved. For a gas-surface temperature of 800 K, it was found that despite CO being the dominant surface reaction product, a gas-phase exchange reaction forms significant CO_2 within the microstructure region. It is important to emphasize again that these results were specific to 800 K and are specific to the gas-phase chemical reaction rates of Ref. [94]. Consistent results were obtained using a real ablated sample where a complex surface mesh was constructed using X-Ray Computed Tomography to render a 3D image and triangulate the ablator surface.

The molecular beam data was then used to develop a new finite rate model. The surface reaction probabilities indicated that the CO probability reached a maximum at 1100 K after which the desorption of oxygen atoms from the surface dominated the surface kinetics. Desorption of oxygen atoms was modeled as a rate activated process with an energy barrier which was found to be 44277 K and was close to the value suggested by Zhluktov and Abe [4], the energy of a single bond between carbon and oxygen. The new model was compared with the ZA model using a 0-D approach and CFD simulations. The model was implemented in the CFD code, US3D and it was seen that the new model predicted similar overall mass loss rates compared to existing models, however, the individual species production rates were completely different. The most notable difference was that the new model (based on molecular beam data) predicts CO as the oxidation reaction product with virtually no CO_2 production, whereas existing models predict the exact opposite trend. CO being the dominant oxidation product was consistent with recent high enthalpy wind tunnel experiments. The development of this

new model is indeed promising and it can be used to predict recession rates, boundary layer species etc. in hypersonic vehicles with carbon ablators.

6.1 Future Steps

Although, significant improvements have been made, a lot remains to be understood and further experimentation and analysis is required to build a model that captures all the important kinetic processes. In this section, I will suggest future steps to study ablation processes from my perspective.

The molecular beam results were obtained using vitreous carbon (VC) and other carbon materials have to be analyzed to validate if reactions are thermal in all carbon materials. The beam data only provided reactions of O atoms with the carbon surface. Under realistic conditions, there would be nitrogen based species, O_2, CO, and CO_2 colliding and reacting with the surface. Although, it is well known that the reactivity of species like O_2 is low, they could form precursors on the surface or affect the partial pressure of the gas near the surface that could inhibit or accelerate the oxidation reactions. Thus, new experiments need to be performed, both with different carbon materials and different gas species.

From a microstructural perspective, it can be concluded that surface area does not affect the composition of species observed in the boundary layer. However, the effect of gas phase reactions within the microstructure was not studied in detail. Since it is now possible to simulate flow over real surfaces using X-ray tomography, the role of gas phase reactions within the microstructure for various carbon materials, at different stages of ablation can be studied in detail. A key question as to why different carbon materials recess or ablate at different rates still does not have a satisfactory explanation. Combining the information from molecular beam experiments and simulations of flow over *real* microstructures could provide the answer to that question.

It is my opinion that this approach of studying the processes at the atomistic scale and the micro scale is useful and as more experimental and simulation data become available, definite conclusions can be made about several unanswered questions which could ultimately lead into developing a “complete” gas-surface model.

References

[1] J. Marschall and M. MacLean. Finite-rate surface chemistry model, I: Formulation and reaction system examples. In *42nd AIAA Thermophysics Conference*, page 3783, Honolulu, Hawaii, June 2011.

[2] J. Marschall, M. MacLean, P.E. Norman, and T.E. Schwartzentruber. Hypersonic Nonequilibrium Flows: Fundamentals and Recent Advances, Chapter 6. In *Surface Chemistry in Nonequilibrium Flows, Progress in Astronautics and Aeronautics, AIAA*, 2015.

[3] M. MacLean, J. Marschall, and D.M. Driver. Finite-Rate Surface Chemistry Model, II: Coupling to Viscous Navier-Stokes Code. In *42nd AIAA Thermophysics Conference, Fluid Dynamics and Co-located Conferences*, page 3784, Honolulu, Hawaii, June 2011.

[4] S.V. Zhluktov and T. Abe. Viscous Shock-Layer Simulation of Airflow past Ablating Blunt Body with Carbon Surface. *Journal of Thermophysics and Heat Transfer*, 21(11):1588–1594, 1983.

[5] P. Schrooyen. Numerical Simulation of Aerothermal Flows through Ablative Thermal Protection Systems. In *Phd Thesis*, November 2015.

[6] C. Park. Stagnation-Point Ablation of Carbonaceous Flat Disks Part I: Theory. *AIAA Journal*, 21(11):1588–1594, 1983.

[7] C.R. Alba, R.B. Greendyke, and J. Marschall. Development of a Nonequilibrium FiniteRate Ablation Model for Radiating Earth Reentry Flows. *Journal of Spacecraft and Rockets*, 53(1):98–120, 2016.

[8] K.T. Nicholson, T.K. Minton, and S.J. Sibener. Spatially Anisotropic Etching of Graphite by Hyperthermal Atomic Oxygen. *The Journal of Physical Chemistry B*, 109(17):8476–8480, 2005.

[9] S. Poovathingal, T.E. Schwartzentruber, S.G Srinivasan, and A.C.T. van Duin. Large Scale Computational Chemistry Modeling of the Oxidation of Highly Oriented Pyrolytic Graphite. *Journal of Physical Chemistry A*, 117(13):2692–2703.

[10] R. Gosse and G.V. Candler. Evaluation of Carbon-Carbon Ablation Models Using a Fully Coupled CFD Solver. In *40th Thermophysics Conference*, page 3908, Reston, VA, June 2008.

[11] McVey D., Auerbach I., and McBride D. Some Observations on The Influence of Graphite Microstructure on Ablation Performance. In *8th Aerospace Sciences Meeting*, page 0155, 1970.

[12] M.A. Havstad and R.M. Ferencz. Comparison of Surface Chemical Kinetic Models for Ablative Reentry of Graphite. *Journal of Thermophysics and Heat Transfer*, 16(4):508–512, 2002.

[13] M.R. Wool. Final summary report passive nosetip technology (pant) program. In *Aerotherm Report 75-159, Report No. SAMSO-TR-75-250.*

[14] J.A. Keenan and G.V. Candler. Simulation of graphite sublimation and oxidation under re-entry conditions. In *6th Joint Thermophysics and Heat Transfer Conference*, page 2083, Colorado Springs, Colorado, June 2004.

[15] A.F. Beerman, M.J. Lewis, R.P. Starkey, and B.Z. Cybyk. Significance of Nonequilibrium Surface Interactions in Stardust Return Capsule Ablation Modeling. *Journal of Thermophysics and Heat Transfer*, 23(3):425–432, 2009.

[16] Candler G.V. Nonequilibrium Processes in Hypervelocity Flows: An Analysis of Carbon Ablation Models. In *50th AIAA Aerospace Sciences Meeting including the New Horizons Forum and Aerospace Exposition, Aerospace Sciences Meetings*, page 0724, Nashville, Tennessee, January 2012.

[17] S.W. Lewis, R.G. Morgan, T.J. McIntyre, C. Alba, and Greendyke R.B. Comparison of Carbon Ablative Shock-Layer Radiation with High Surface Temperatures. In *AIAA Aviation 45th AIAA Thermophysics Conference*, page 2348, Dallas, Texas, June 2015.

[18] S.W. Lewis, R.G. Morgan, T.J. McIntyre, C. Alba, and Greendyke R.B. Expansion Tunnel Experiments of Earth Reentry Flow with Surface Ablation. *Journal of Spacecraft and Rockets*, pages 1–13, 2016.

[19] C.R. Alba. A Nonequilibrium Finite-Rate Carbon Ablation Model For Radiating Earth Re-entry Flows. In *Phd Thesis, AFIT-ENY-DS-15-S-053*, September 2015.

[20] C.R. Alba, R.B. Greendyke, S.W. Lewis, R.G. Morgan, and T.J. McIntyre. Numerical Modeling of Earth Reentry Flow with Surface Ablation. *Journal of Spacecraft and Rockets*, 53(1):84–97, 2016.

[21] D. E. Rosner and H. D. Allendorf. Comparative Studies of the Attack of Pyrolytic and Isotropic Graphite by Atomic and Molecular Oxygen at High Temperatures. *AIAA Journal*, 6(4):650–654, 1968.

[22] S. Poovathingal and T.E Schwartzentruber. Computational Chemistry Modelling of the Oxidation of Highly Oriented Pyrolytic Graphite. In *43rd AIAA Thermophysics Conference, Fluid Dynamics and Co-located Conferences*, page 3099, New Orleans, Louisiana, June 2012.

[23] J.T. Paci, H.P. Upadhyaya, J. Zhang, G.C. Schatz, and T.K. Minton. Theoretical and Experimental Studies of the Reactions between Hyperthermal O(^{3}P) and Graphite: Graphene-Based Direct Dynamics and Beam-Surface Scattering Approaches. *The Journal of Physical Chemistry A*, 113(16):4677–4685, 2009.

[24] V.J. Murray, B.C. Marshall, P.J. Woodburn, and Minton T.K. Inelastic and Reactive Scattering Dynamics of Hyperthermal O and O_2 on Hot Vitreous Carbon Surfaces. *Journal of Physical Chemistry C*, 119(26):14780–14796, 2015.

[25] S. Poovathingal, T.E. Schwartzentruber, V.J. Murray, and T.K. Minton. Molecular simulations of surface ablation using reaction probabilities from molecular beam experiments and realistic microstructure. *AIAA Journal*, 54(1):1–12, 2016.

[26] C. Berger, Z. Song, X. Li, X. Wu, N. Brown, C. Naud, D. Mayou, T. Li, J. Hass, A.N. Marchenkov, E.H. Conrad, P.N. First, and W.A. deHeer. Electronic Confinement and Coherence in Patterned Epitaxial Graphene. *Science*, 312:1191–1196, 2006.

[27] K.S. Kim, Y. Zhao, H. Jang, S.Y. Lee, J.M. Kim, K.S. Kim, J.H. Ahn, P. Kim, J.Y. Choi, and B.H. Hong. Large-scale pattern growth of graphene films for stretchable transparent electrodes. *Nature*, 457:706–710, 2009.

[28] Y.W. Son, M.L. Cohen, and S.G. Louie. Energy Gaps in Graphene Nanoribbons. *Physical Review Letters*, 97(21):216803, 2006.

[29] X. Wang, Y. Ouyang, X. Li, H. Wang, J. Guo, and H. Dai. Room-Temperature All-Semiconducting Sub-10-nm Graphene Nanoribbon Field-Effect Transistors. *Physical Review Letters*, 100(20):206803, 2008.

[30] L.R. Radovic and B. Bockrath. On the Chemical Nature of Graphene Edges: Origin of Stability and Potential for Magnetism in Carbon Materials. *Journal of the American Chemical Society*, 127(16):5917–5927, 2005.

[31] D.E. Jiang, B.G. Sumpter, and S. Dai. First principles study of magnetism in nanographenes. *Journal of Chemical Physics*, 127:124703, 2007.

[32] D.E. Jiang, B.G. Sumpter, and S. Dai. Unique chemical reactivity of a graphene nanoribbon's zigzag edge. *Journal of Chemical Physics*, 126:134701, 2007.

[33] R. Sharma, N. Nair, and M.S. Strano. StructureReactivity Relationships for Graphene Nanoribbons. *The Journal of Physical Chemistry C*, 113(33):14771–14777, 2009.

[34] M.Y. Han, B. Ozyilmaz, Y. Zhang, and P. Kim. Energy Band-Gap Engineering of Graphene Nanoribbons. *Physical Review Letters*, 98(20):206805, 2007.

[35] F. Rodriguez-reinoso and P.A. Thrower. Microscopic studies of oxidized highly oriented pyrolytic graphites. *Carbon*, 12(3):269–279, 1974.

[36] C. Wong, R.T. Yang, and B.L. Halpern. The mode of attack of oxygen atoms on the basal plane of graphite. *Journal of Chemical Physics*, 78:3325, 1983.

[37] X. Chu and L.D. Schmidt. Gasification of graphite studied by scanning tunneling microscopy. *Carbon*, 29(8):1251–1255, 1991.

[38] L. Zhang, D.A. Pejakovi, B. Geng, and J. Marschall. Surface modification of highly oriented pyrolytic graphite by reaction with atomic nitrogen at high temperatures. *Applied Surface Science*, 257(13):5647–5656, 2011.

[39] F. Stevens, L.A. Kolodny, and T.P. Beebe. Kinetics of Graphite Oxidation: Monolayer and Multilayer Etch Pits in HOPG Studied by STM. *The Journal of Physical Chemistry B*, 102(52):10799–10804, 1998.

[40] K.T. Nicholson, T.K. Minton, and S.J. Sibener. Temperature-dependent morphological evolution of {HOPG} graphite upon exposure to hyperthermal O(3P) atoms. *Progress in Organic Coatings*, 47(3):443–447, 2003.

[41] K.T. Nicholson, T.K. Minton, and S.J. Sibener. Nucleation and growth of nanoscale to microscale cylindrical pits in highly-ordered pyrolytic graphite upon hyperthermal atomic oxygen exposure. In *9th International Symposium on Materials in a Space Environment*, Noordwijk, The Netherlands, 2003.

[42] H. Kinoshita, M. Umeno, M. Tagawa, and N. Ohmae. Hyperthermal atomic oxygen beam-induced etching of {HOPG} (0001) studied by X-ray photoelectron spectroscopy and scanning tunneling microscopy. *Surface Science*, 440(1):49–59, 1999.

[43] H.O. Pierson. *Handbook of Carbon, Graphite, Diamond and Fullerenes.* Noyes, New Jersey, USA, 1993.

[44] E.J. Bottani and J.M.D. Tascón. *Adsorption by Carbons.* Elsevier, Amsterdam, Netherlands, 2008.

[45] C. Park. *Nonequilibrium Hypersonic Aerothermodynamics.* Wiley Publications, New Jersey, USA, 1990.

[46] I.A. Leyva, S. Laurence, A.W.K. Beierholm, H.G. Hornung, R. Wagnild, and G.V. Candler. Transition delay in hypervelocity boundary layers by means of CO_2/acoustic instability interactions. In *47th AIAA Aerospace Sciences Meeting*

Including The New Horizons Forum and Aerospace Exposition, Orlando, Florida, January 2009.

[47] S.G. Srinivasan and A.C.T. van Duin. Molecular-Dynamics-Based Study of the Collisions of Hyperthermal Atomic Oxygen with Graphene Using the ReaxFF Reactive Force Field. *The Journal of Physical Chemistry A*, 115(46):13269–13280, 2011.

[48] V. Morn, L. Martin-Gondre, C. Crespos, P. Larregaray, P. Gamallo, and R. Says. Classical dynamics study of atomic oxygen over graphite with new interpolated and analytical potential energy surfaces. *Computational and Theoretical Chemistry*, 990:132–143, 2012.

[49] A.C.T. van Duin, S. Dasgupta, F. Lorant, and W.A. Goddard. ReaxFF: A Reactive Force Field for Hydrocarbons. *The Journal of Physical Chemistry A*, 105(41):9396–9409, 2001.

[50] W.J. Mortier, S.K. Ghosh, and S. Shankar. Electronegativity-equalization method for the calculation of atomic charges in molecules. *Journal of the American Chemical Society*, 108(15):4315–4320, 1986.

[51] K. Chenoweth, A.C.T. van Duin, and W.A. Goddard. ReaxFF Reactive Force Field for Molecular Dynamics Simulations of Hydrocarbon Oxidation. *The Journal of Physical Chemistry A*, 112(5):1040–1053, 2008.

[52] K. Nomura, R.K. Kalia, A. Nakano, P. Vashishta, A.C.T. van Duin, and W.A. Goddard. Dynamic Transition in the Structure of an Energetic Crystal during Chemical Reactions at Shock Front Prior to Detonation. *Physical Review Letters*, 99(14):148303, 2007.

[53] K. Chenoweth, A.C. T. van Duin, S. Dasgupta, and William.A. Goddard. Initiation Mechanisms and Kinetics of Pyrolysis and Combustion of JP-10 Hydrocarbon Jet Fuel. *The Journal of Physical Chemistry A*, 113(9):1740–1746, 2009.

[54] K. Chenoweth, A.C.T. van Duin, S. Dasgupta, and W.A. Goddard. Initiation Mechanisms and Kinetics of Pyrolysis and Combustion of JP-10 Hydrocarbon Jet Fuel. *The Journal of Physical Chemistry A*, 113(9):1740–1746, 2009.

[55] H.J. Qian, A.C. T. van Duin, K. Morokuma, and S. Irle. Reactive Molecular Dynamics Simulation of Fullerene Combustion Synthesis: ReaxFF vs DFTB Potentials. *Journal of Chemical Theory and Computation*, 7(7):2040–2048, 2011.

[56] A. Bagri, C. Mattevi, M. Acik, Y.J. Chbal, M. Chhowalla, and V.B. Shenoy. Structural evolution during the reduction of chemically derived graphene oxide. *Nature Chemistry*, 2:581–587, 2010.

[57] A.D. Kulkarni, D.G. Truhlar, S.G. Srinivasan, A.C.T. van Duin, P. Norman, and T.E. Schwartzentruber. Oxygen Interactions with Silica Surfaces: Coupled Cluster and Density Functional Investigation and the Development of a New ReaxFF Potential. *The Journal of Physical Chemistry C*, 117(1):258–269, 2013.

[58] S. Plimpton. Fast Parallel Algorithms for Short-Range Molecular Dynamics. *Journal of Computational Physics*, 117(1):1–19, 1995.

[59] P. Valentini, T.E. Schwartzentruber, and I. Cozmuta. Molecular dynamics simulation of O_2 sticking on Pt(111) using the *ab-initio* based ReaxFF reactive force field. *Journal of Chemical Physics*, 133:84703, 2010.

[60] T. Sun, S. Fabris, and S. Baroni. Surface Precursors and Reaction Mechanisms for the Thermal Reduction of Graphene Basal Surfaces Oxidized by Atomic Oxygen. *The Journal of Physical Chemistry C*, 115(11):4730–4737, 2011.

[61] A. Barinov, O.B. Malcioglu, S. Fabris, T. Sun, L. Gregoratti, M. Dalmiglio, and M. Kiskinova. Initial Stages of Oxidation on Graphitic Surfaces: Photoemission Study and Density Functional Theory Calculations. *The Journal of Physical Chemistry C*, 113(21):9009–9013, 2009.

[62] W.G. Vinceti and G.H. Kruger. *Introduction to Physical Gas Dynamics*. Krieger, Florida, USA, 2002.

[63] J. Zhang, D.J. Garton, and T.K. Minton. Reactive and inelastic scattering dynamics of hyperthermal oxygen atoms on a saturated hydrocarbon surface. *Journal of Chemical Physics*, 117:6239, 2002.

[64] G. Bird. *Molecular Gas Dynamics and the Direct Simulation of Gas Flows*. Oxford Science Publications: New York, USA, 1994.

[65] W. Tsang and R.F. Hampson. Chemical Kinetic Data Base for Combustion Chemistry. Part I. Methane and Related Compounds. *Journal of Chemical Reference Data*, 15:1087, 1986.

[66] R.H. Fowler and E.A. Guggenheim. *Statistical Thermodynamics*. Cambridge University Press: London, UK, 1939.

[67] Lachuad J. and Vignoles G.L. A Brownian motion technique to simulate the gasification and its application to C/C composite ablation. *Computational Material Science*, 44(4):1024–1041, 2009.

[68] J. Lachaud, I. Cozmuta, and Mansour N.N. Multiscale Approach to Ablation Modeling of Phenolic Impregnated Carbon Ablators. *Journal of Spacecrafts and Rockets*, 47(6):910–921, 2010.

[69] Lachaud J. and Mansour N.N. Microscopic scale simulation of the ablation of fibrous materials. In *48th AIAA Aerospace Sciences Meeting Including the New Horizons Forum and Aerospace Exposition, Aerospace Sciences Meetings*, page 984, Orlando, Florida, January 2010.

[70] A. Martin. Volume averaged modeling of the oxidation of porous carbon fiber material. In *44th AIAA Thermophysics Conference, Fluid Dynamics and Co-located Conferences*, page 2636, San Diego, California, June 2013.

[71] B. Helber, O. Chazot, T. Magin, and A. Hubin. Ablation of carbon preform in the VKI Plasmatron. In *43rd AIAA Thermophysics Conference, Fluid Dynamics and Co-located Conferences*, page 2876, New Orleans, Lousiana, June 2012.

[72] F. Panerai, A. Martin, N.N. Mansour, S.A. Sepka, and J. Lachaud. Flow-tube Oxidation Experiments on the Carbon Preform of PICA. In *44th AIAA Thermophysics Conference, Fluid Dynamics and Co-located Conferences*, page 2769, San Diego, California, June 2013.

[73] Mansour N.N., Panerai F., Martin A., Parkinson D.Y., MacDowell A., Fast T., Vignoles G., and Lachaud J. A New Approach To Light-Weight Ablators Analysis: From Micro-Tomography Measurements to Statistical Analysis and Modeling. In *44th AIAA Thermophysics Conference, Fluid Dynamics and Co-located Conferences*, page 2768, San Diego, California, June 2013.

[74] Zeiring M. and DiCristina V. Thermomechanical erosion of ablative plastic composites. In *7th Thermophysics Conference*, page 0299, 1972.

[75] S.M. Lee. *Handbook of Composite Reinforcements*. VCH Publishers UK, 1992.

[76] I. Nompelis and T.E. Schwartzentruber. A Parallel Implementation Strategy for Multi-Level Cartesian Grid Based DSMC Codes. In *51st AIAA Aerospace Sciences Meeting including the New Horizons Forum and Aerospace Exposition, Aerospace Sciences Meetings*, page 1204, Grapevine, Texas, June 2013.

[77] D. Gao, C. Zhang, and T.E. Schwartzentruber. Particle Simulations of Planetary Probe Flows Employing Automated Mesh Refinement. *Journal of Spacecraft and Rockets*, 48(3):397–405, 2011.

[78] C. Zhang and T.E. Schwartzentruber. Robust Cut-Cell Algorithms for DSMC Implementations Employing Multi Level Cartesian Grids. *Computers and Fluids*, 69:122–135, 2012.

[79] J. Zhong, T. Ozawa, and D.A. Levin. Modeling of Stardust Reentry Ablation Flows in the Near-Continuum Flight Regime. *AIAA Journal*, 46(10):2568–2581, 2008.

[80] D.M. Driver, M.W. Olson, M.D. Barnhardt, and M. MacLean. Understanding High Recession Rates of Carbon Ablators Seen in Shear Tests in an Arc Jet. In *48th AIAA Aerospace Sciences Meeting Including the New Horizons Forum and Aerospace Exposition, Aerospace Sciences Meetings*, page 1177, Orlando, Florida, January 2010.

[81] J. Thoemel, O. Chazot, and P. Barbante. Aspects of advanced modeling for hypersonic flows. In *Proceedings of the Summer Program*, Center for Turbulence Research, Stanford University, 2008.

[82] Y.T. Lee, J.D. McDonald, P.R. LeBreton, and D.R. Herschbach. Molecular Beam Reactive Scattering Apparatus with Electron Bombardment Detector. *Review of Scientific Instruments*, 40(11):1402, 1969.

[83] D.J. Garton, A.L. Brunsvold, T.K. Minton, D. Troya, B. Maiti, and G.C. Schatz. Experimental and Theoretical Investigations of the Inelastic and Reactive Scattering Dynamics of $O(^3P) + D_2$. *Journal of Physical Chemistry A*, 110(4):1327–1341, 2006.

[84] J. Zhang, D.J. Garton, and T.K. Minton. Reactive and inelastic scattering dynamics of hyperthermal oxygen atoms on a saturated hydrocarbon surface. *Journal of Chemical Physics*, 117(13):6239–6251, 2002.

[85] G.E. Caledonia, R.H. Krech, and B.D. Green. A high flux source of energetic oxygen atoms for material degradation studies. *AIAA Journal*, 25(1):59–63, 1987.

[86] D.J. Garton, T.K. Minton, B. Maiti, D. Troya, and G.C. Schatz. A crossed molecular beams study of the $O(^3P)+H_2$ reaction: Comparison of excitation function with accurate quantum reactive scattering calculations. *Journal of Chemical Physics*, 118(4):1585–1588, 2003.

[87] D. Troya and G.C. Schatz. Theoretical studies of hyperthermal $O(^3P)$ collisions with hydrocarbon self-assembled monolayers. *Journal of Chemical Physics*, 120(16):7696–7707, 2004.

[88] C. T. Rettner, D. J. Auerbach, J. C. Tully, and A. W. Kleyn. Chemical Dynamics at the Gas-Surface Interface. *Journal of Physical Chemistry*, 100(31):13021–13033, 1996.

[89] V. Moron, L. Martin-Gondre, P. Gamallo, and R. Sayo. Quasiclassical Trajectory Dynamics Study of Atomic Oxygen Collisions on an O-Preadsorbed Graphite (0001) Surface with a New Analytical Potential Energy Surface. *Journal of Physical Chemistry C*, 116(24):13092–13103, 2012.

[90] S. Poovathingal and T.E. Schwartzentruber. Effect of microstructure on carbon-based surface ablators using dsmc. In *AIAA Scitech 52nd Aerospace Sciences Meeting*, page 1210, National Harbor, Maryland, January 2014.

[91] J.E. Sheehan, K.W. Buesking, and B.J. Sullivan. Carbon-carbon composites. *Annual Review of Material Science*, 24(1):19–44, 1994.

[92] R.L. Burns. *Carbon-Carbon Materials and Composites*. William Andrew Publishing, New York, USA, 1993.

[93] C. Zhang and T.E. Schwartzentruber. Inelastic collision selection procedures for direct simulation monte carlo calculations of gas mixtures. *Physics of Fluids*, 25(10):106105, 2013.

[94] C. Park, J.T. Howe, R.L. Jaffe, and G.V. Candler. Review of Chemical-Kinetic Problems of Future NASA Missions II Mars Entries. *Journal of Thermophysics and Heat Tranfer*, 8(1):9–23, 1994.

[95] K.C. Tseng, J.S. Wu, and I.D Boyd. Simulations of Re-Entry Vehicles by Using DSMC with Chemical-Reaction Module. In *14th AIAA/AHI Space Planes and Hypersonic Systems and Technologies Conference*, page 8084.

[96] B.L. Haas, D.B. Hash, G.A. Bird, F.E. Lumpkin, and H.A. Hassan. Rates of thermal relaxation in direct simulation Monte Carlo methods. *Physics of Fluids*, 6(6):21912201, 1994.

[97] N.E. Gimelshein, S.F. Gimelshein, and D.A. Levin. Vibrational relaxation rates in the direct simulation Monte Carlo method. *Physics of Fluids*, 14:4452–4455, 2002.

[98] S. Doraiswamy, J.D. Kelley, and G.V. Candler. Vibrational Modeling of CO2 in High-Enthalpy Nozzle Flows. *Journal of Thermophysics and Heat Transfer*, 24(1):9–17, 2010.

[99] Boyd I.D. Modeling backward chemical rate processes in the direct simulation monte carlo method. *Physics of Fluids*, 19(12):126103, 2007.

[100] L.Y. Yeung, M. Okumura, J. Zhang, T.K. Minton, J.T. Paci, A. Karton, J.M.L. Martin, J.P. Camden, and J. Schatz. $O(^3P)$ + CO_2 Collisions at Hyperthermal Energies: Dynamics of Non-Reactive Scattering, Oxygen Isotope Exchange, and Oxygen-Atom Abstraction. *Journal of Physical Chemistry A*, 116(11):64–84, 2011.

[101] E. Stern, I. Nompelis, T.E. Schwartzentruber, and G.V. Candler. Microscale Simulations of Porous TPS Materials: Application to Permeability. In *AIAA*

Aviation: 11th AIAA/ASME Joint Thermophysics and Heat Transfer Conference, page 2247, Atlanta, Georgia, June 2014.

[102] D. Troya and G.C. Schatz. Theoretical Studies of Hyperthermal O(^{3}P) Collisions with Hydrocarbon Self-Assembled Monolayers. *Journal of Chemical Physics*, 120:7696, 2004.

[103] Giapis K.P. Minton, T.K. and T. Moore. Inelastic Scattering Dynamics of Hyperthermal Fluorine Atoms on a Fluorinated Silicon Surface. *Journal of Physical Chemistry A*, 101(36):6549–6555, 1997.

[104] Smoll E.J. Purcell S.M. Costen M.L. McKendrick K.G. Marshall, B.C. and T.K. Minton. Scattering Dynamics of Oxygen Atoms on Imidazolium Tetrafluoroborate Ionic Liquid Surfaces: Dependence on Alkyl Chain Length. *Journal of Physical Chemistry C*, 10.1021/acs.jpcc.6022886, 2016.

[105] H. D. Allendorf and D. E. Rosner. Primary Products in the Attack of Graphite by Atomic Oxygen and Diatomic Oxygen Above 1100. *Carbon*, 7(4):515–518, 1969.

[106] D. E. Rosner and H. D. Allendorf. High Temperature Oxidation of Carbon By Atomic Oxygen. *Carbon*, 3(2):153–156, 1965.

[107] J. Nagle and R.F. Strickland-Constable. Oxidation of Carbon between 1000-2000 C. In *Proceedings of the fifth carbon conference*, volume 1, Oxford: Pergamon Press, New York, 1962.

[108] J.R. Walls and R.F. Strickland-Constable. Oxidation of carbon between 1000-2400 C. *Carbon*, 1(3):333–338, 1964.

[109] A. Eucken. *2. 5ng.-Chem.*, 48:986, 1930.

[110] L. Meyer. *2. physk. Chem.*, 17B:385, 1932.

[111] X. Duval. *Journal of Chemical Physics*, 41:339, 1950.

[112] D.R. Olander, W. Siekhaus, R. Jones, and J.A. Schwarz. Reactions of Modulated Molecular Beams with Pyrolytic Graphite. I. Oxidation of the Basal Plane. *Journal of Chemical Physics*, 57(1):408–420, 1972.

[113] W.C.C. Shih. Molecular Beam Studies of Graphite Oxidation. In *M.I.T. PhD Thesis*, 1973.

[114] G.N.K. Liu. High Temperature Oxidation of Graphite by a Dissociated Oxygen Beam. In *M.I.T. PhD Thesis*, 1973.

[115] G. Blyholder, J.S. Binford Jr, and H. Eyring. A Kinetic Theory for the Oxidation of Carbonized Filaments. *The Journal of Physical Chemistry*, 62(3):263–267, 1958.

[116] I.G. Pitt, R.G. Gilbert, and K.R. Ryan. Application of Transition-State Theory to Gas-Surface Reactions: Barrierless Adsorption on Clean Surfaces. *Journal of Physical Chemistry*, 98(49):13001–13010, 1994.

[117] Huheey. *pp. A-21 to A-34, The Strengths of Chemical Bonds.* 2nd ed., Butterworths, London, 1958.

[118] C. Sorensen, P. Valentini, and T.E. Schwartzentruber. Uncertainty Analysis of Reaction Rates in a Finite-Rate Surface-Catalysis Model. *Journal of Thermophysics and Heat Transfer*, 26(3):407–416, 2012.

[119] C.R. Alba, R.B. Greendyke, and J. Marschall. Influence of carbon nitridation in a nonequilibrium finite-rate ablation model. In *53rd AIAA Aerospace Sciences Meeting*, page 1453, Kissimmee, Florida, January 2015.

[120] I. Nompelis, T.W. Drayna, and G.V. Candler. A Parallel Unstructured Implicit Solver for Reacting Flow Simulation. In *17 th AIAA Computational Flow Dynamics Conference*, page 4867, June 2005.

[121] C. Park. Review of Chemical-Kinetic Problems of Future NASA Missions I - Earth Entries. *Journal of Thermophysics and Heat Transfer*, 7(3):385–398, 1993.

[122] C. Park, J.T. Howe, R.L. Jaffe, and G.V. Candler. Review of Chemical-Kinetic Problems of Future NASA Missions II- Mars Entries. *Journal of Thermophysics and Heat Transfer*, 8(1):9–23, 1994.